

**Data Acquisition, Detector Technology,  
and Materials Analysis with a  
Scanning Ion Microprobe**

**David Peter Louis Simons**

Copyright ©1998 David P.L. Simons

Omslagontwerp en fotografie: Paul Simons

Druk: Universiteitsdrukkerij Technische Universiteit Eindhoven

CIP-DATA LIBRARY TECHNISCHE UNIVERSITEIT EINDHOVEN

SIMONS, David Peter Louis

Data Acquisition, Detector Technology, and Materials Analysis  
with a Scanning Ion Microprobe / by David Peter Louis Simons. -

Eindhoven : Eindhoven University of Technology, 1998. -

Proefschrift Technische Universiteit Eindhoven - with ref. - with summary in Dutch.

ISBN 90-386-0767-9

NUGI 812

Trefw.: ionenbundel analyse / halfgeleider detectoren / ioniserende straling

Subject headings: ion-beam analysis / ion microprobe analysis / materials analysis / data  
acquisition / semiconductor detectors / position sensitive detectors / charge-coupled devices /  
particle detectors / ionizing radiation / radiation damage effects / conjugated polymers /  
functional polymers / uranium microparticle characterization

# **Data Acquisition, Detector Technology, and Materials Analysis with a Scanning Ion Microprobe**

PROEFSCHRIFT

ter verkrijging van de graad van doctor  
aan de Technische Universiteit Eindhoven,  
op gezag van de Rector Magnificus, prof.dr. M. Rem,  
voor een commissie aangewezen door het College  
voor Promoties in het openbaar te verdedigen op  
maandag 14 december 1998 om 16.00 uur

door

**David Peter Louis Simons**

geboren te Roermond

Dit proefschrift is goedgekeurd door de promotoren

prof.dr. M.J.A. de Voigt  
en  
prof.dr.ir. K. Kopinga.

Copromotor:

dr.ir. P.H.A. Mutsaers.

*Aan mijn ouders en aan mijn broer*



# Contents

<b>General introduction</b>	<b>1</b>
Data acquisition .....	3
Detector technology.....	3
Alternative detection systems.....	4
Radiation damage effects .....	4
Materials analysis .....	5
Organic semiconductor device-related effects .....	5
Diffusion processes during patterned photo-polymerization.....	5
Verification of a uranium micromass standard .....	5
References .....	6
<b>Chapter 1 The Eindhoven multi-parameter data-acquisition system for ion beam experiments</b>	<b>7</b>
1.1 Introduction .....	8
1.2 Experiments and their requirements to data acquisition .....	8
1.2.1 Scattering set-up.....	9
1.2.2 Microprobe set-up.....	9
1.2.3 Channeling set-up.....	10
1.3 Data-acquisition system requirements and design .....	10
1.4 Front-end hardware and software .....	12
1.4.1 Hardware.....	12
1.4.2 Software .....	16
1.5 Back-end hardware and software.....	18
1.5.1 Hardware.....	18
1.5.2 Software .....	18
1.6 System performance .....	22
1.6.1 Front-end acquisition .....	22
1.6.2 Back-end monitoring.....	23
1.7 Applications.....	25
1.7.1 A scanning ion microprobe IBIC experiment .....	25
1.7.2 A channeling angular-scan measurement.....	26
1.7.3 Time- and dose-dependent list-mode measurements.....	28
1.7.4 An ERDA-PSD experiment .....	29
1.8 Conclusions and recommendations .....	31
References .....	32

<b>Chapter 2 Exploration of X-ray and charged-particle spectroscopy with CCDs and PSDs</b>	<b>33</b>
2.1 Introduction .....	34
2.2 Alternative detector types .....	34
2.2.1 X-ray spectroscopy.....	34
2.2.2 Charged-particle spectroscopy .....	35
2.3 X-ray spectroscopy with a CCD .....	37
2.3.1 CCD operation principle .....	37
2.3.2 Aspects of CCD X-ray spectroscopy.....	39
2.3.3 Conclusions .....	48
2.4 Charged-particle spectroscopy with a PSD.....	49
2.4.1 PSD operating principle .....	49
2.4.2 Theory of PSD operation.....	50
2.4.3 Pre-amplifier requirements, theory, and design .....	54
2.4.4 Noise theory and optimum shaping time.....	57
2.4.5 Characterization measurements.....	61
2.4.7 Conclusions .....	64
References .....	65
<b>Chapter 3 Radiation damage in silicon detectors caused and analyzed by a microprobe</b>	<b>67</b>
3.1 Introduction .....	68
3.2 PIPS detectors.....	69
3.3 Detector radiation damage.....	70
3.3.1 Causes of damage.....	70
3.3.2 Effects of damage.....	70
3.4 Techniques.....	72
3.4.1 Scanning Transmission Ion Microscopy (STIM) .....	72
3.4.2 Ion Beam Induced Charge (IBIC) .....	73
3.4.3 Data-filtering techniques .....	74
3.5 Experimental.....	77
3.5.1 Experimental set-up .....	77
3.5.2 Pulse-height vs. dose.....	78
3.5.3 Pulse-height vs. position .....	78
3.6 Results and discussion .....	79
3.6.1 Pulse-height vs. dose.....	79
3.6.2 Pulse-height vs. position .....	84
3.6.3 Protons vs. helium ions .....	87
3.6.4 STIM vs. IBIC.....	88
3.7 Conclusions and recommendations .....	90
References .....	91



---

<b>Chapter 4 <math>\mu</math>PIXE study of organic semiconductor devices</b>	<b>93</b>
4.1 Introduction .....	94
4.2 Organic field-effect transistors .....	95
4.3 Precursor-route pentacene MISFET measurements.....	98
4.4 Organic electroluminescent diodes .....	101
4.5 $\text{InCl}_3$ formation in ITO/PPV structures.....	103
4.6 Conclusions .....	105
References .....	106
<b>Chapter 5 <math>\mu</math>PIXE study of diffusion processes during patterned photo-polymerization</b>	<b>107</b>
5.1 Introduction .....	108
5.2 Photo-induced diffusion processes .....	109
5.3 $\mu$ PIXE analysis of photo-induced diffusion.....	111
5.3.1 Sample preparation.....	111
5.3.2 $\mu$ PIXE experiments .....	112
5.3.3 Interpretation of the results .....	116
5.4 $\mu$ PIXE analysis of dual-labeled lithographic gratings .....	117
5.4.1 Description of the dual-labeled system .....	117
5.4.2 Sample preparation.....	117
5.4.3 $\mu$ PIXE analysis of the dual-labeled grating film .....	118
5.4.4 Interpretation of the results .....	124
5.5 Conclusions and recommendations .....	125
References .....	126
<b>Chapter 6 Verification of a uranium micromass standard using an ion microprobe</b>	<b>127</b>
6.1 Introduction .....	128
6.2 Experimental.....	129
6.2.1 Sample preparation.....	129
6.2.2 Ion microprobe measurements .....	130
6.3 Results and discussion .....	133
6.4 Conclusions and recommendations .....	135
References .....	136
<b>Summary</b>	<b>137</b>
<b>Samenvatting</b>	<b>139</b>
<b>Publications</b>	<b>141</b>
<b>Dankwoord</b>	<b>142</b>
<b>Curriculum Vitae</b>	<b>144</b>



# General introduction

The scanning ion microprobe is a sophisticated instrument that is used for the imaging, characterization, elemental analysis and even modification of a wide range of samples [1]. It is based on a charged-particle accelerator, an ion-beam focusing system, an ion-beam scanning system, and a detection system for measuring beam-sample interactions.

The charged-particle accelerator provides the high-energy ion beam, which consists of protons or helium ions with energies of a few MeV. The ion beam is focused to a spot on the sample under investigation, with a diameter in the micrometer regime or sometimes even the sub-micrometer regime. Additionally, the scanning system provides the means to scan the focussed beam spot across the sample in a predefined scan pattern. This makes the analysis of samples possible in two dimensions with a high lateral position resolution.

Various imaging and analytical techniques are applied in an ion microprobe [2]. Each technique is based on the measurement of specific interactions between the high-energy incoming ions and the sample matter. For this purpose a detection system is used, which comprises detectors for charged particles and X-rays, and a data-acquisition system.

The imaging techniques include scanning transmission ion microscopy (STIM) [5] and ion beam induced charge (IBIC) [6] analysis. In STIM, the energy loss of ions after sample transmission is measured from which areal density distributions can be derived. In IBIC, the charge induced in the sample itself is measured, from which charge-collection efficiency distributions can be derived.

The analytical techniques include Rutherford back- and forward scattering spectrometry (RBS/RFS) [3], elastic recoil detection analysis (ERDA) [4], and nuclear reaction analysis (NRA) [7]. RBS and RFS are based on the scattering of the incoming ions on sample atoms, whereas ERDA is based on the recoiling of atoms from the sample by incoming ions. NRA is based on the detection of products from nuclear reactions between incoming ions and atoms in the sample. All these techniques are mainly used to study depth and lateral distributions of bulk and minor elements in the sample.

At the moment, the most important analytical tool of the ion microprobe is the particle induced X-ray emission (PIXE) [8] technique. This technique is based on the detection of X-rays, emitted in a discrete line structure that is specific for each element. Because of the relatively high cross-sections, the PIXE technique is widely used to detect and quantify trace elements. The application of the PIXE technique in an ion microprobe is called  $\mu$ PIXE.

The primary feature of the scanning ion microprobe is its ability to apply various imaging and analytical techniques in two dimensions, with a relatively high lateral position resolution.

The stopping power of MeV protons and helium ions in the majority of samples is relatively small, which results in a depth range of the incoming ions from a few  $\mu\text{m}$  to over a hundred  $\mu\text{m}$ . Consequently, imaging and depth profiling of relatively thick samples, throughout their entire depth is possible in an ion microprobe. Note, however, that the amount of self-

absorption of emitted X-rays increases with sample thickness, which can complicate PIXE analyses.

Both the lateral position resolution and the energy spread of the focused ion beam worsen with increasing depth. The initial lateral position resolution, which is determined by the beam spot size, is degraded by multiple scattering of the ions traversing the sample. The initial beam energy spread is degraded by the straggling of the ions traversing the sample. In practice, however, these effects are relatively small. Both beam broadening and range straggling add up to only a few  $\mu\text{m}$  for MeV protons and to about 1  $\mu\text{m}$  for MeV helium ions, at the end of their track. These resolutions allow for the use of a scanning ion microprobe in a wide range of analytical applications.

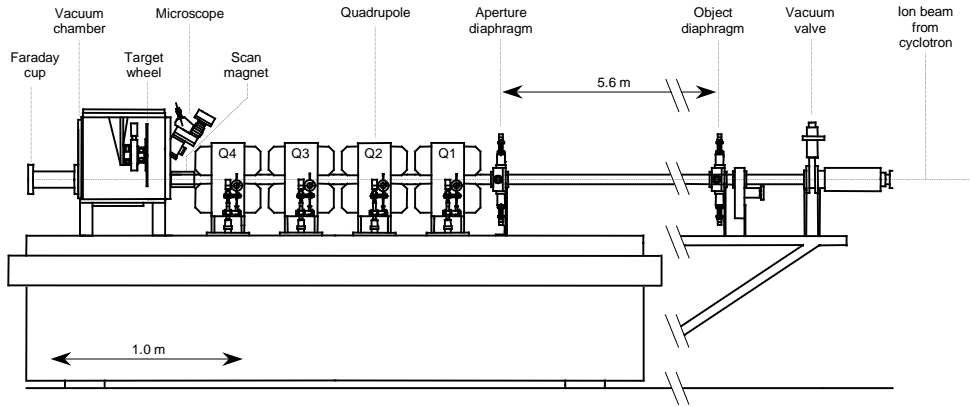


*Fig. 1: Side view of the Eindhoven scanning ion microprobe set-up [9].*

All topics presented in this dissertation concern the Eindhoven scanning ion microprobe set-up [9]. A schematic drawing of this set-up is shown in Fig. 1.

The ion beam supplied by the particle-accelerator enters the set-up from the right. The particle-accelerator at Eindhoven University of Technology is a variable-energy Philips AVF cyclotron [11]. This cyclotron can accelerate protons, deuterium ions, and helium ions to an energy in the range of 2-30 MeV. For microprobe experiments, 3 MeV protons and 4 MeV  $\text{He}^+$  ions generally are used. The microprobe-setup is connected to the cyclotron via a beam guidance system, which includes a dispersive system to reduce the beam energy spread [12].

The object and aperture diaphragms of the microprobe set-up (5.6 m apart) define the object size and the divergence of the beam. Using four magnetic quadrupoles, the ion beam is focused to a spot on the target (sample) in the vacuum chamber. For elemental analyses, a proton beam with a spot diameter of 3  $\mu\text{m}$  FWHM and a current up to 100 pA can be obtained. In STIM, where a current of about 1 fA suffices, a spot size of 1  $\mu\text{m}$  FWHM can be obtained.

Eight samples can be mounted in the target wheel, which is attached to a translation and rotation stage. A scan magnet, behind the focusing system, is used to move (scan) the beam spot across the sample. A Faraday cup is present to facilitate beam charge measurements.

X-rays emitted from the target (PIXE) are detected using a Si(Li) detector, mounted at a backward angle of 135 degrees. Scattered, recoiled, or transmitted ions are detected using solid-state charged-particle detectors mounted at a backward angle of 147 degrees (for RBS) and at a variable forward angle (for RFS, STIM and IBIC). Details about the Eindhoven scanning ion microprobe set-up can be found in [9], and in Chapter 1 of this dissertation.

Three areas of research and development, related to the scanning ion microprobe, are presented in this dissertation: data acquisition, detector technology, and materials analysis. A short introduction to each of these is given below.

## Data acquisition

Prior to the work in this dissertation, a system for set-up control, data acquisition, and data analysis was developed by Mutsaers [9], dedicated to microprobe experiments. For the other ion-beam analysis set-ups at the Cyclotron laboratory, the set-up control was mostly performed manually and data acquisition was limited to one single parameter at a time.

It was desirable to have an improved and general system for set-up control, data acquisition, data monitoring, and data analysis, for routine use in all ion-beam analysis experiments at the laboratory. To achieve this goal, the set-up control dedicated to the microprobe set-up had to be expanded to support all ion-beam analysis set-ups at the Cyclotron laboratory. Furthermore, the data acquisition had to be improved to support multiple-parameter data-acquisition, enabling a wide range of ion-beam experiments, including coincidence experiments. In addition to list-mode measurements, histogram-mode measurements had to be supported, including measurements as a function of time and beam charge. More features and an improved performance of the on-line data visualization and monitoring were also required. Last but not least, it was desirable to improve the reliability, performance, and scalability of the relational data base that is used to store all relevant information about the experiments.

It was decided to design and implement such a new system, based on the existing hardware configuration and software. The development of this new system for set-up control, multi-parameter data-acquisition, monitoring, and data analysis, which is usually referred to as ‘the data-acquisition system’, is described in Chapter 1.

## Detector technology

The high lateral resolution of the ion microprobe can also cause limitations to its analytical performance. The reduction of the beam-spot size at a given beam current is likely to increase the sample deterioration, because of the increase of areal dose. Although the use of very low beam currents may reduce this damage, a certain number of detected beam-sample

interactions (events) is still required and thus measurement time increases. Alternatively, use can be made of both beam-sample interactions with higher cross sections and detection systems with an increased detection efficiency.

### Alternative detection systems

In this work, two alternative detection systems for use in the Eindhoven scanning ion microprobe are studied. First, the applicability of a charge-coupled device (CCD) system to X-ray spectroscopy in  $\mu$ PIXE analyses is explored. This study was inspired by the progress in low-energy X-ray spectroscopy with CCDs in the field of astronomy, where an enhanced detection efficiency for soft X-rays (compared to a Si(Li) detector) together with excellent energy resolutions is reported. In the first part of Chapter 2, a literature survey on CCD X-ray spectroscopy will be presented. Based on this, the feasibility of  $\mu$ PIXE with CCDs is discussed.

Second, the applicability of a commercial (SiTek type 1L30) position sensitive detector (PSD), widely used for laser-light tracking, to charged-particle spectroscopy is explored. This PSD, based on the resistive charge-dividing principle, is both energy disperse and position sensitive in one dimension. For energy-disperse charged-particle spectroscopy in ion-scattering techniques, its energy resolution and linearity have to be comparable to that of a conventional charged-particle detector. If so, via its additional position sensitivity, angle-disperse charged-particle spectroscopy may be applied to correct for the increased kinematic energy spread. This energy spread is inherent to enlarged detector solid angles in ion-scattering techniques. In the second part of Chapter 2, both a theoretical and an experimental characterization of this PSD will be presented. Based on this, the applicability of this PSD to ion-scattering experiments is discussed.

### Radiation damage effects

The highly focussed ion beam can not only cause damage to the sample under analysis, but also to the detectors that are used in the experiment. Especially during STIM analyses, where the detector is placed behind a thin sample to measure the energy-loss of the ions, the focussed ion beam almost directly irradiates the detector. Occasionally, in STIM measurements, a change in the pulse-height-to-energy calibration of the STIM detector is observed, which affects the accuracy in the energy-loss measurement. It was decided to study radiation-damage effects in a charged-particle detector, and specifically the pulse-height-to-energy calibration as a function of ion dose and irradiation position. Using this, it is possible to correct for change in the pulse-height-to-energy calibration during STIM analyses. This study is presented in Chapter 3.

## Materials analysis

The useful and sometimes unique properties of the  $\mu$ PIXE technique in the ion microprobe set-up, including the new data-acquisition system, will be demonstrated. Several analytical studies have been carried out, in collaboration with researchers from various disciplines.

### Organic semiconductor device-related effects

Chapter 4 shows a study of organic semiconductor device-related effects, applying the  $\mu$ PIXE technique. The lateral position resolution (micrometer range) allows to measure minor and trace elements in actual devices.

First, for precursor-route pentacene-based field-effect transistors (pentacene MISFET), the conversion efficiency of the precursor is studied, as a function of conversion temperature. This is done by *in-situ* measurement in the devices of the residual of chlorine, which is contained in the precursor leaving-group only. The purpose is to relate this residual amount of chlorine to the device performance, as measured on the same devices.

Second, for precursor-route poly-(phenylene-vinylene) based light-emitting diode (PPV-LED) structures, degradation is studied of the indium-tin-oxide (ITO) electrode by hydrochloric acid. Hydrochloric acid is released during the precursor conversion and sometimes supplied as an acid catalyst during conversion. This study was performed in conjunction with studies on the diffusion of indium from the electrode into the organic layer [10], in the course of the FOM Rolling Grants project 'Fundamental and material properties of (semi)conducting polymers (application to electronic devices)' at Eindhoven University of Technology.

### Diffusion processes during patterned photo-polymerization

The lithographic and holographic illumination of an isotropic mono-acrylate and a liquid crystalline di-acrylate blend is known to produce polymer films with a lateral modulation in their refractive index. It is believed that the  $\mu$ PIXE technique provides the means to quantitatively study lateral diffusion processes in such mixtures of liquid monomers during patterned photo-polymerization. The requirement is that pattern dimensions match the beam spot-size.

By labeling one of the (acrylate) monomers with an element that can be detected with the PIXE technique, for example silicon, it should be possible to reveal the final monomer distribution in the films. If chemical composition modulations across the film are found, the alleged two-way monomer diffusion may be confirmed. Furthermore, the use of a dual-labeled monomer system, which allows for detection of both monomers could yield full quantification of the monomer distribution. This study will be presented in Chapter 5.

### Verification of a uranium micromass standard

The ion microprobe is an instrument that, almost uniquely, can perform the elemental analysis and mass determination of individual, micrometer-sized particles. In Chapter 6, this ability is

used to determine the relative mass distribution of a set of 4  $\mu\text{m}$ -sized spherical uranium-oxide ( $\text{U}_3\text{O}_8$ ) particles. The purpose of this is to check whether such a set is monodisperse in its uranium mass, since then it may serve as a micromass calibration standard for analytical tools in the detection of uranium for various uses.

## References

- [1] Proceedings of the 5th International Conference on Nuclear Microprobe Technology and Applications, Nucl. Instr. and Meth. B 130 (1997), and M.B.H. Breese, D.N. Jamieson and P.J.C. King, Materials Analysis using a Nuclear Microprobe, (Wiley, New York, 1996).
- [2] K.G. Malmqvist, Nucl. Instr. and Meth. B 104 (1995) 138-151.
- [3] W.K. Chu, J.W. Mayer, M.A. Nicolet, Backscattering Spectrometry, (Academic Press, New York, 1978).
- [4] J. L'Ecuyer *et al.*, J Appl. Phys. 47 (1976) 381-382.
- [5] G. Bench, A. Saint, G.J.F Legge, M. Cholewa, Nucl. Instr. and Meth. B 77 (1993) 175.
- [6] M.B.H. Breese, P.J.C. King, G.W. Grime, F. Watt, J. Appl. Phys. 72 (1992) 2097.
- [7] G. Demortier, Nucl. Instr. and Meth. B 104 (1995) 244-254.
- [8] S.A.E. Johansson, J.L. Campbell, K.G. Malmqvist, Particle Induced X-ray Emission Spectrometry, (Wiley, New York, 1995).
- [9] P.H.A. Mutsaers, Design and Realisation of the Eindhoven Scanning Proton Microprobe, (Ph.D. Dissertation, Eindhoven University of Technology, 1995).
- [10] M.P. de Jong, D.P.L. Simons, M.A. Reijme, L.J. van IJzendoorn, A.W. Denier van der Gon, M.J.A. de Voigt, H.H. Brongersma, and R.W. Gymer, to be submitted to Synth. Metals.
- [11] H.L. Hagedoorn, P. Kramer, IEEE Trans. Nucl. Sci. NS-13 (1966) 449.
- [12] G.E. Sandvik, H.L. Hagedoorn, F. Schutte, Nucl. Instr. and Meth. 106 (1973) 245.



# Chapter 1

## The Eindhoven multi-parameter data-acquisition system for ion beam experiments

*The multi-parameter data-acquisition system for performing ion beam experiments at the Cyclotron laboratory Eindhoven is described. This system is used for microprobe, ion scattering, and channeling experiments. The front-end part (PhyDAS) consists of two separate bus systems: a VME bus with an MPS030 processor board, equipped with a Motorola 68030 CPU, and a homemade bus with experiment interfaces. PhyDAS handles real-time data-acquisition, control of the experiment, and data transport to the back-end system. This back-end system consists of a Digital Alphastation that takes care of data storage, monitoring, and analysis, both on-line and off-line. The hardware and software of both the front-end and back-end system are discussed as well as the overall system performance. Applications are given to illustrate the advantages of this multi-parameter data-acquisition system for ion beam experiments.*

Related publication: "A multi-parameter system for acquisition, monitoring, and analysis of scanning ion microprobe data", P.H.A Mutsaers, D.P.L. Simons, Nucl. Instr. and Meth. B130 (1997) 127-132.

## 1.1 Introduction

In this chapter, the multi-parameter data-acquisition system for performing ion beam experiments at the Cyclotron laboratory Eindhoven is described. This system is commonly used with the microprobe set-up, the channeling set-up, and the ion-scattering set-up.

At the beginning of this work, a system for set-up control, data acquisition and data analysis, dedicated to microprobe experiments, had been developed by Mutsaers [1,2]. From this, a channeling set-up control system had been derived, together with some data-acquisition software. For the ion-scattering set-up, data acquisition was limited to one single parameter at a time and set-up control was performed manually. It was, however, desired to have a general system for set-up control, data acquisition, and data analysis.

In this work, such a general system has been developed. The hardware configuration of the existing microprobe control and acquisition system has been maintained: a front-end computer system for set-up control and real-time data-acquisition, and a back-end system for data visualization and data analysis. Both the front-end and back-end software have been redesigned and newly implemented. The system now supports the necessary control of all three set-ups. Multi-parameter data-acquisition, *i.e.* acquisition of data corresponding to multiple experimental signals, has been implemented, enabling use in a wide range of experiments, including coincidence experiments. Furthermore, both list-mode and histogram-mode experiments are fully supported, also enabling measurements as a function of time and beam charge. On-line data visualization has been improved to support these new features. Last but not least, a relational database has been added that is used to store all relevant information about experiments.

In section 1.2, the requirements with respect to a data-acquisition system are discussed from an experimental point-of-view. Section 1.3 gives an overview of primary requirements for a generalized data-acquisition system. Furthermore, an introduction to its design is given. In section 1.4, the design, implementation, and description of the front-end hardware and software will be given in more detail. In section 1.5, this will be done for the back-end hardware and software. The performance of this system is discussed in section 1.6. Applications of the new system are shown in section 1.7 to illustrate its value.

## 1.2 Experiments and their requirements to data acquisition

At the Cyclotron laboratory of Eindhoven University of Technology, a Philips AVF cyclotron is used that can accelerate protons, deuterons, and helium ions, to energies in the range of 2-30 MeV. The ion beam can be transported, amongst others, to one out of the four available ion-beam analysis set-ups: the scattering set-up, the microprobe set-up, the channeling set-up, or the PIXE set-up. For each of the first three set-ups, an overview of the applied ion-beam analysis techniques will be given, together with a discussion of experimental details and requirements, relevant for the data-acquisition system. The PIXE set-up will not be discussed further, because it has its own commercial data-handling system.

### 1.2.1 Scattering set-up

In the scattering set-up, Rutherford backscattering spectrometry (RBS) [3] and elastic recoil detection analysis (ERDA) [4] techniques are available for mass analysis and depth profiling. These are used to study, for example, diffusion and degradation effects in polymer light-emitting device (PLED) systems [5].

The scattering set-up allows for the use of a variable number of detectors, located at different scattering angles and distances. Depending on its type, a detector may give only an energy signal, or also a position and timing signal. Using analog electronics, rise-time or flight-time signals may be created from the detector output signals. For coincident scattering and recoiling experiments using position sensitive detectors and flight-time measurement, this may result in ten signals to be recorded for one event. From now on, these signals will be called *experimental parameters*.

Generally, it is desired that the data are stored event-by-event (list-mode), sometimes also as a function of time. In other experiments, it is sufficient to collect data during a fixed time interval into histograms, one for each experimental parameter. Count-rates up to 10 kilo-counts-per-second (kcps) per experimental parameter may be expected. For normalization purposes, it is necessary to record the beam charge, as measured by a Faraday cup.

### 1.2.2 Microprobe set-up

In the scanning ion microprobe set-up, particle induced X-ray emission (PIXE) [6] is used to measure trace-elemental concentration distributions in, for example, biomedical tissue [7]. Simultaneously, nuclear (non-Rutherford) back- and forward scattering (NBS/NFS) are used to determine the areal mass-density distribution. In addition to optical sample visualization with a microscope, scanning transmission ion microscopy (STIM) [8] is available. The ion beam induced charge (IBIC) technique [9] has been used to study radiation damage effects in semiconductor particle detectors [10].

The microprobe contains a focusing system [1] to create a beam spot with a diameter of a few micrometers. A scan magnet can deflect a 3 MeV proton beam about 3 mm in the horizontal or vertical direction, thus allowing beam scanning. Generally, the scanning is carried out in steps from position to position according to a pre-determined scan pattern. The sample itself can also be moved with an  $x$ - $y$  stepper motor stage. An X-ray detector is installed for PIXE analysis, and two silicon charged-particle detectors are mounted at a fixed backward and a variable forward angle for NBS, NFS, and STIM. The count-rate for each detector has a maximum of 10 kcps.

One may collect energy data in histogram-mode or in list-mode, with the beam position as an extra experimental parameter. Time-dependent measurements are also desired, to be able to correct for possible radiation damage. Normalization requires beam charge measurement. Finally, computer control of beam focussing, beam scanning, and target wheel movement is required.

### 1.2.3 Channeling set-up

In this set-up, the channeling technique [11] is available for structure analysis of crystalline samples, such as strain determination in epitaxially grown semiconductor multi-layers [12]. The channeling set-up consists of an ultra-high vacuum chamber with a sample manipulator (goniometer). The latter is capable of rotating the sample over three angles (around three axes) with an inaccuracy of less than 0.01 degree [12]. In general, an RBS detector is located at a backward angle to record the back-scattered ion yield. For transmission channeling, a second detector at a forward angle may be used. For charge measurement, an additional detector in the beam line records back-scattered particles from a vane, that rotates through the beam. Count-rates with a maximum of 10 kcps for each detector are expected. Typically, histograms are to be collected for all experimental parameters, over a fixed time interval. This is repeated for various sample orientations, thus requiring automated goniometer control. The histograms of the backward and forward detector have to be normalized with data from the rotating-vane detector histogram.

## 1.3 Data-acquisition system requirements and design

In section 1.2, the requirements with respect to a data-acquisition system from an experimental point-of-view are given. In this section, these are generalized into a list of primary requirements for the multi-parameter data-acquisition system. The new system needs to support:

#### *Control of the experiment*

- Microprobe beam focussing via quadrupole magnet current steering
- Microprobe beam scanning via scan pattern calculation and scan magnet steering.
- Microprobe target-wheel movement via stepper motors.
- Channeling goniometer manipulation via stepper motors.

#### *Multi-parameter acquisition*

- At least ten *experimental parameters*, each with a count-rate up to 10 kcps. A sampling resolution of 12 bit is sufficient.
- List-mode and/or histogram-mode acquisition, also simultaneously (mixed mode).
- Coincident and non-coincident *experimental parameters*; also mixed.
- Collection of data for all *experimental parameters* during the same, fixed time interval. For example, two *experimental parameters* are coincident and have to be recorded in list-mode. Simultaneously, during exactly the same time interval, the histogram of another, non-coincident *experimental parameter* has to be recorded.
- Data that is fixed over a single measurement time interval, such as measurement time, beam charge, and target orientation, has to be stored as *header parameters*, to be used for subsequent analysis, like normalization.

*Data manipulation*

- For each event in the list-mode data, it should be possible to perform calculations on the experimental parameter values, applying user-editable equations. This is, for example, needed to calculate particle velocities  $v=L/T$  from measured flight times  $T$ . Results of the calculations are to be stored as *derived parameters*, in addition to the data of experimental parameters.
- For the histogram-mode, it should be possible to perform calculations on the histogram data, like determination of peak yield, centroid, and standard deviation. This is necessary for *e.g.* histogram normalization.
- Division of list-mode and histogram-mode data into intervals of equal measuring time or dose, to enable time- and dose-dependent analysis.
- Sorting of list-mode data into histograms, often conditionally by applying Boolean logic to experimental and derived parameters.
- Data compression and reduction, if data flows become too large for further processing.

*Data visualization*

- Single parameter histograms of experimental and derived parameters, for both histogram-mode and list-mode data.
- Two-parameter scatter-plots including microprobe count/concentration-distribution plots. Plots of list-mode data for two experimental or derived parameters versus each other. Plots of one histogram-mode experimental or derived parameter versus a header parameter.
- Conditional graphics generation, by applying Boolean logic to experimental and derived parameters.
- Generation of graphics has to be performed on-line (during the measurement) to monitor the experiment, and off-line (afterwards) for further analysis.

*Data analysis*

- Calibrations and fits (like channel-to-energy conversion and peak fitting).
- Calculation of areal mass density, depth profiles, and (trace) elemental concentration distributions.

*Data storage*

- Storage of acquired list-mode and histogram-mode data into files on storage disk.
- Management system for creating and restoring storage tape back-ups.

*Experiment logging*

- Automatically keep a log of the experimental set-up and progress.
- Allow the user to add notes in an electronic logbook.

A data acquisition and analysis system has been designed that consists of two parts. The front-end part takes care of experiment control and real-time data-acquisition. The back-end part is used for (on-line) data monitoring, data processing, and archiving. Data transport from the front-end to the back-end system is controlled by the front-end system but performed by an intermediate data server. This data server also takes care of data storage on the back-end system. In this way, experiment progress and real-time data-acquisition are separated from data monitoring and processing. This division was also made since an excellent system for set-up control and real-time data-acquisition already existed at our department. Only a second computer system, more suitable for data visualization and analysis, had to be added. The hardware and software of the front-end system and the back-end system are described in sections 1.4 and 1.5, respectively.

## 1.4 Front-end hardware and software

### 1.4.1 Hardware

The front-end system is based on the Physics Data Acquisition System (PhyDAS) [13], which has been developed at the Department of Applied Physics. It is therefore readily available, maintainable, and can be adapted to our specific needs. In Fig. 1.1, a schematic hardware layout of our PhyDAS front-end system is given. It consists roughly of two parts: a VME-bus [14] part and a homemade Physics Bus System (PhyBUS) part.

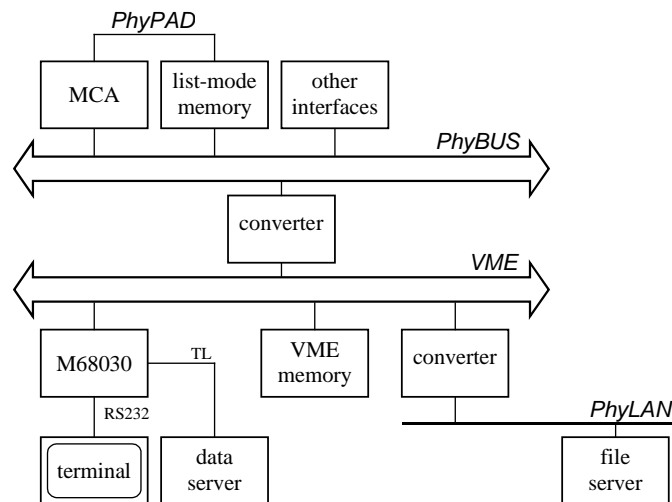


Fig. 1.1: Overview of the Physics Data Acquisition System (PhyDAS).

The VME-bus part consists of an MPS030 processor board with a Motorola M68030 40 MHz CPU, which can be controlled via a serial line, and a 64 Mbyte memory board. The operating

system and user program codes are stored on a file server, that is accessed using the Physics Local Area Network (PhyLAN) via a VME/PhyLAN converter, based on historic reasons.

The PhyBUS is a locally developed, dedicated bus (32-bit wide, 300 ns read-cycle and 400 ns write-cycle minimum protocol time), which contains ‘intelligent’ experiment interfaces. It can be connected to any computer bus system (*e.g.* VME, PCI). In our case it is connected to VME via the VME/PhyBUS converter. This converter also allows for Direct Memory Access (DMA) transport between experiment interfaces and VME interfaces, *e.g.* the MPS030 processor board, at a rate of about 2.5 Mbyte/s.

In addition to the PhyBUS, the Physics Parallel Asynchronous Dataway (PhyPAD) has been implemented (32-bit wide, 100 ns minimum protocol time, and handshake mechanism identical to the PhyBUS). This allows for fast data transport between experiment interfaces in a master-slave, point-to-point configuration, while at the same time the PhyBUS remains available for other purposes.

Several interfaces have been designed and implemented in the PhyBUS. Interfaces like counters, timers, stepper motor interfaces, and I/O controllers (IEEE, RS232) are available. These are used *e.g.* for sample manipulation, current measurement, and steering and stabilization of the current sources for the microprobe focussing magnets [2].

The interface that is used in all set-ups for the actual acquisition of data in list-mode or histogram-mode, is the Multi-Channel Analyzer (MCA) interface (see Fig. 1.2).

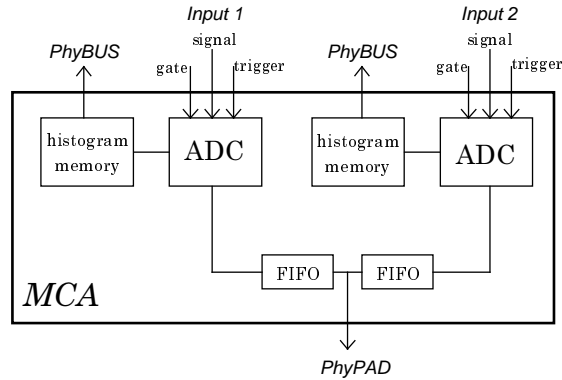


Fig. 1.2: Schematic layout of the Multi Channel Analyzer (MCA) interface.

A MCA interface contains two 12-bit analog-to-digital converters (ADCs) that are used to digitize incoming signal pulse heights (the experimental parameters, like detector pulses or time-to-amplitude converter signals), triggered by an external pulse. The conversion time of these ADCs is about 1.6  $\mu$ s. For each ADC, the digitized pulse heights are used to build a pulse-height histogram in the histogram memories on the MCA board. Afterwards, these memories can be read out via the PhyBUS. Optionally, the digitized pulse heights from either one ADC or both ADCs working in coincidence can be send via a PhyPAD connection to a 2 Mbyte list-mode memory (see Fig. 1.1). The MCA/list-mode memory combination can work

autonomously, without loading the PhyBUS, and data does not have to be read out until a preset time interval has elapsed or until the list-mode memory is full, as discussed below.

At the moment, three MCA boards are present in our system, which enables the measurement of up to six (coincident) input signals (experimental parameters). Validity of ADC conversions can be determined using an externally supplied coincidence gate signal. Invalid conversions are not sent to the histogram memory. In the list-mode memory they are marked as invalid.

Another set of interfaces is associated with the control of the microprobe scan magnet and its controller. A schematic layout of this control system is shown in Fig. 1.3.

The scan magnet controller contains the power supplies connected to the x and y deflection units of the scan magnet. The current steering is carried out using four 12-bit DACs. For both deflection directions, one DAC is used for coarse current steering and one for additional fine steering. A 16-bit value that is sent to the scan magnet controller must contain the DAC number and its 12-bit DAC value.

The simplest implementation would have been to connect the scan magnet controller directly to a PhyBUS I/O controller and make the MPS030 CPU change the DAC values each time the beam has to be stepped to a next position. Such a solution, however, would load the CPU heavily with low-level tasks, and would not satisfy the required real-time, continuous operation of the beam scanning during list-mode measurements. Therefore, the scan magnet controller is connected to a 2 Mbyte static memory module. This 32-bit pattern memory contains the user-defined, pre-calculated scan pattern. Each 32-bit value consists of a 16-bit number, that is sent to the scan magnet controller, and an additional 16-bit Position Identification Number (PIN), that uniquely identifies each position within the scan pattern. In this way, a scan pattern can have a maximum of 65536 positions and an arbitrary shape.

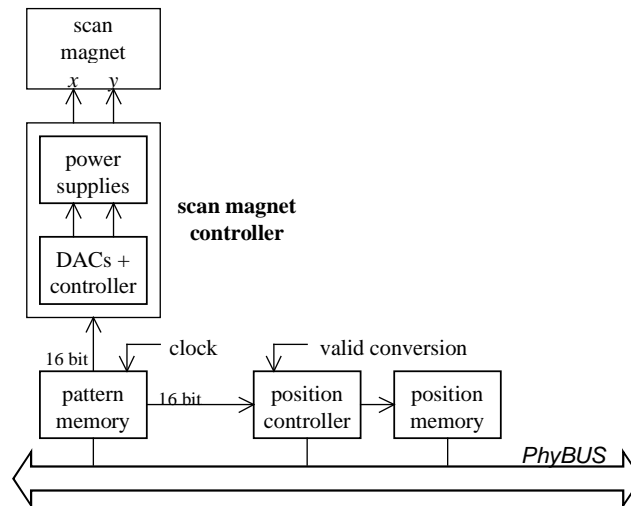


Fig. 1.3: Schematic layout of the scan magnet control system



To have the beam scanning work autonomously, the pattern memory is clocked by an external clock pulse generator. A clock pulse increments the memory pointer and initiates (asynchronous) transfer of the new scanning position data from the pattern memory to both the scan magnet controller and the position controller (see below). The step frequency can be selected by simply changing the clock-pulse frequency. Since measurements [1] have shown that the step response time of the scan magnet system is less than 0.1 ms, step frequencies up to 10 kHz are possible.

In scanning microprobe experiments, the position of the beam has to be recorded together with each incoming energy event from a detector. Therefore, each set consisting of MCA interface and a 2 Mbyte list-mode memory for the energy experimental parameter data also contains a 2 Mbyte list-mode memory to store the position experimental parameter data. One of these position memories is depicted in Fig. 1.3. Each time an MCA makes a valid energy conversion, a valid conversion pulse is sent to the position controller (see Fig. 1.3). This controller then copies the current 16-bit PIN from the pattern memory into the position list-mode memory that is associated with the initiating MCA and its energy list-mode memory. Each of the 2 Mbyte list-mode memories can contain up to about  $10^6$  events. As mentioned above, data is collected autonomously until one or more list-mode memories are full, but generally until a pre-set time interval (generally 60 s) has elapsed. Then, all MCAs are paused and the processor initiates DMA transfer, which copies the contents of the list-mode and/or histogram memories into the 64 Mbyte VME memory, for all memories in use. Within a fraction of a second, the MCAs can be restarted. The MCAs and the charge measurement are paused during readout to ensure the same fixed measurement time interval for all MCAs, and thus the same beam dose for all data.

At the moment, it is not necessary to perform additional data processing, like data compression or reduction. After restarting the MCAs, the front-end system immediately initiates data transfer of the raw data, together with information about measurement time, beam current, and dose, from the VME memories to the back-end system for further processing. Fig. 1.4 schematically shows the data transmission path from the front-end to the back-end system.

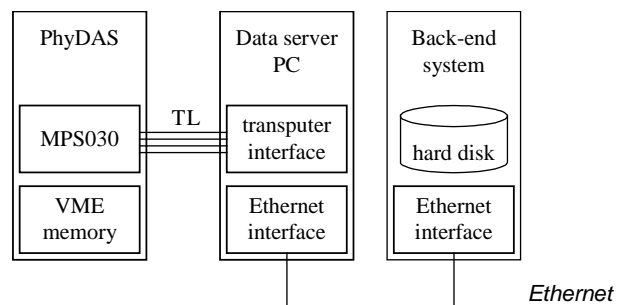


Fig. 1.4: Data transmission from the front-end (PhyDAS) to the back-end system via the data server (see text for details).

In addition to the serial line for console use, the MPS030 board in the PhyDAS is equipped with a Transputer Link (TL) interface. This provides four links, each with a transfer capacity of 20 Mbit/s. The back-end system (section 1.5), however, does not support a TL connection and the PhyDAS does not support Ethernet access. Therefore, an intermediate data server, equipped with both a TL interface and an Ethernet interface, has been installed. The acquired data and additional information is sent from the VME memory to this data server, which is a 486DX2-66 based PC, working under MS-DOS 7. Next, via Ethernet and Digital Pathworks software, the data is copied into files that are physically located on one of the back-end system hard disks. This makes the data available for, *e.g.* on-line processing by the back-end system. Effective transfer speeds are up to 250 kbyte/s (see section 1.6).

One of the advantages of this set-up is that the real-time data-acquisition by the front-end system and the storage of data onto disk are separated from data processing and data visualization by the back-end system. Furthermore, storage of data in time interval blocks ( $\Delta t_{\text{sample}}$ ), each having sufficient statistics, allows for easy time and dose dependent analyses, of both list-mode and histogram-mode data.

#### 1.4.2 Software

The software that runs on the PhyDAS is the Eindhoven Program Editor and Processor (EPEP) [15], which like the PhyDAS, has been developed at the Department of Applied Physics. EPEP is a combination of a real-time operating system (PEP030) and a programming language with a line editor and a program interpreter. The language closely relates to Pascal. User program codes can be loaded on top of each other, into shell levels. Higher shell levels can use the procedures, functions, and variables from previous, lower shell levels. In this way new ‘commands’ can be added to the operating system.

A data-acquisition software package has been designed and implemented: the Cyclotron Eindhoven Data Acquisition Software (CEDAS). This software has been divided into several levels. Each level can use routines from lower levels. Basic and some frequently used routines are included in the lower levels. This simplifies the code of higher levels and also enables the call of basic routines directly from the command line.

The levels, from low to high, are: the communication level, the interface level, the routines level, and the acquisition and control level.

##### *Level 1: Communication level*

This level contains routines that simplify communication between the front-end and the back-end system, over both the serial line and the TL. Furthermore, communication with the outside world (user) is simplified by including warning and error messages, together with a terminal graphics library.

*Level 2: Interface level*

This level contains routines that isolate hardware addresses and interface control from higher levels. Using an interface table, a unique index is assigned to each experiment interface. This avoids hard-coded numbers and addresses in higher levels. Furthermore, basic routines like starting, stopping, and resetting of experiment interfaces are included.

*Level 3: Routines level*

The level contains routines to simplify control of the experimental set-up. This includes routines for *e.g.* magnet current adjustment, target wheel motion, and scan pattern generation. Furthermore, this level deals with the multi-parameter features of the system. Since the system was designed for a variable number and type of experimental parameters, it has to keep track of the various data, and hence routines have been added for the user to change the multi-parameter set-up definition, that the system uses to keep track of the various data flows. The multi-parameter set-up definition contains the number of experimental parameters, which are sorted into groups (modules) of coincident experimental parameters. Furthermore, an MCA input and/or a list-mode memory is assigned to each experimental parameter. In this way, virtually any type of multi-parameter experiment can be set-up.

*Level 4: Acquisition and control level*

This level contains several sets of routines for automated data acquisition and control of actual experiments with the various set-ups.

Acquisition routines for both list-mode and histogram-mode multi-parameter data-acquisition have been written. These perform starting and stopping of the appropriate MCA interfaces and subsequent readout of the list-mode and/or histogram-mode memories. This is done, based on the multi-parameter set-up definition and various other settings, like measurement-interval length and number of intervals. Data for each measurement interval is stored in files on the back-end system disks. These files contain the histogram and list-mode data for all experimental parameters, in addition to data for the header parameters, such as measurement time and beam charge.

Control routines have been included for (automated) microprobe beam-focussing and beam-diameter measurement. Furthermore, control routines have been written for automated measurements at a series of scan positions, target-wheel positions, or goniometer orientations. Data is then acquired in either list-mode or histogram-mode. In channeling experiments, these routines are used to measure angular scans, and in microprobe experiments to irradiate the sample at series of individual points.

If new types of acquisition or control are required, the corresponding routines can easily be added on top of the existing routines in this level.

## 1.5 Back-end hardware and software

### 1.5.1 Hardware

The back-end system consists of a Digital Alphastation 400 equipped with a 233 MHz Alpha RISC processor, 96 Mbyte of internal memory, and a 21" color monitor. It runs the Digital OpenVMS AXP V6.2 operating system and the X Window System version 11, with the OSF Motif Toolkit and Window Manager. The workstation has several Gbyte SCSI hard disks and DAT storage drives connected to it. It is clustered with several other Digital Alphastations.

### 1.5.2 Software

The back-end system software that has been developed is called COLUMBUS. This graphical control shell is written using the VAX-C language and the X and Motif Toolkit. COLUMBUS can be divided into four modules: the database module, the experiment-control module, the monitoring module, and the off-line analysis module.

#### 1. Database module

A database has been implemented into COLUMBUS, to be able to automatically record all relevant information about the experiment, in addition to the acquired data. A major objective of the database is to replace the conventional logbook. It can store *e.g.* experimental set-up conditions (beam properties, detector configuration, sample information), multi-parameter set-up definitions, monitoring demands (graphics to be drawn during experiment monitoring), file locations of acquired data, analysis demands and results, and user information.

A commercial Relational Database Management System (RDBMS) has been installed (Oracle V7) within the VMS-cluster. The COLUMBUS database module contains routines to interface to this database server and to store and retrieve information from the database. Via a Graphical User Interface (GUI), which has been implemented in the database module, the experimenter can edit the database contents. The other COLUMBUS modules use database contents as input for their routines, and their output results are added to the database. In this way, the database module serves as an intermediate between the COLUMBUS modules, by controlling exchange of information.

A relational database has been designed and implemented. The database model is depicted in Fig. 1.5. Each box corresponds to a database table. A table is a collection of records, each with a unique key and a set of fields. The central table is the *Experiment* table, which contains records of all performed experiments. As an example, the COLUMBUS GUI window to edit the content of the records in the *Experiment* table is shown in Fig. 1.6. Each record in a table is uniquely defined by a key, composed of identification number (*id*). and a unique *name*. Fields in a record can contain user data or a reference to records (keys) in other tables. User-data fields in the *Experiment* table allow for *e.g.* the storage of experiment type, user comment, beam properties, and slit settings.

Similar GUI windows are available to edit records in the other tables in the COLUMBUS database. The essential tables include: *Sample* (the sample under analysis), *User* (the person that performed the experiment), *Graphic* (a histogram or scatter-plot, drawn during monitoring), *Parameter* (an experimental, header, or derived parameter), *Fileseries* (list-mode or histogram-mode data files), *Module* (a group of coincident experimental parameters), *Configuration* (a collection of *Modules*).

Relations that have been defined between tables are depicted as arrows in Fig. 1.5. Relations are either of the type *one-to-many* ( $1:n$ ) or *many-to-many* ( $m:n$ ). In the first case, many records in one table may refer to one and the same record in another table. The relation between the *Experiment* table and the *User* table, for example, is ( $1:n$ ); each experiment is performed by only one user, but the same user can perform multiple experiments. This can be seen in Fig. 1.6, where the *Experiment* record refers to one *User* only. Other reference fields point to, for example, the sample under analysis, or the microprobe scan-pattern.

In the case of a ( $m:n$ ) relation, one record in a table may refer to many records in another table, and *vice versa*. For example, a graphic (table *Graphic*) can be based on the data of multiple parameters (table *Parameter*), and one parameter can be used in multiple graphics. This has been implemented using intermediate cross-reference tables (like *Par\_in\_Graph*, *Graph\_in\_Mon*, *Module\_in\_Config*, *Par\_in\_Module* and *Comp\_in\_Module*).

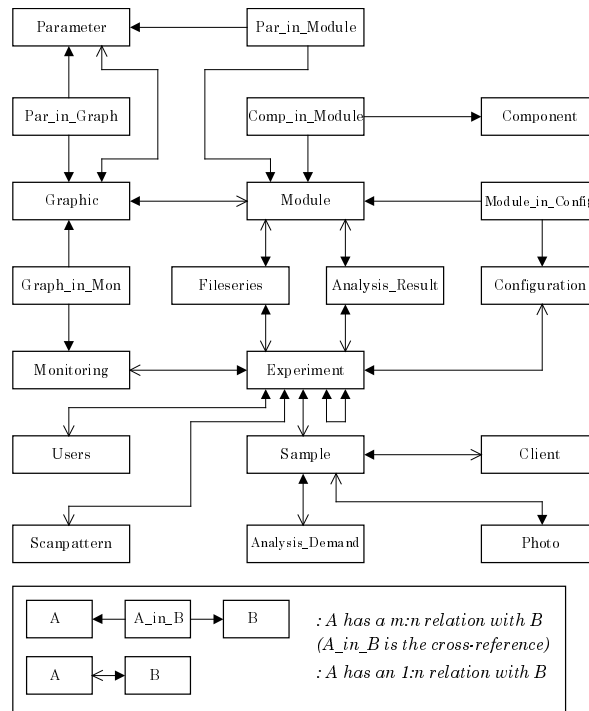


Fig. 1.5: The COLUMBUS database model (see text).

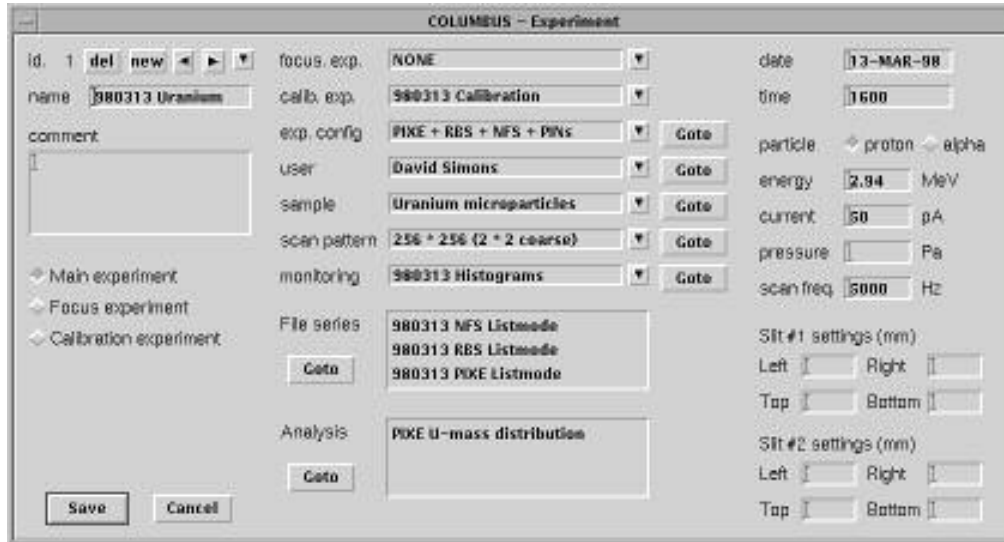


Fig. 1.6: The COLUMBUS GUI to edit the Experiment database table (see text).

The COLUMBUS database model has been normalized to the 3<sup>rd</sup> normal form. There are, however, three exceptions to this normalization. The first exception is that a record in the *Experiment* table can refer to another record in the same table. As can be seen in Fig. 1.6, three types of experiments are available: a main experiment, a focus experiment, and a calibration experiment. Because of this exception, beam-focussing and calibration experiments can be referred to by subsequent main experiments.

The second exception to the 3<sup>rd</sup> normal form is the direct coupling of a unique *Fileseries* record to both an *Experiment* record and one of the *Module* records, whereas the latter is also coupled to the *Experiment* record via the *Configuration* table. The same exception holds for the *Analysis\_Result* records. It has been implemented to speed up database search-queries of all *Fileseries* and *Analysis\_Result* records belonging to an *Experiment* record. These queries are frequently performed; *i.e.* each time an *Experiment* record is edited (see Fig. 1.6).

A third exception to the 3<sup>rd</sup> normal form are the combined (1:*n*) and (*m*:*n*) relations between *Graphic* and *Parameter*. For each graphic, one or two parameters have to be selected for which the data is plotted. A third parameter may be selected of which the data is used to normalize the graphic. For each of these parameters, a (1:*n*) relation is used. The (*m*:*n*) relation via the cross-reference table *Par\_in\_Graph*, on the other hand, is used to store conditions (channel windows) that are set on one or more parameters for each graphic.

## 2. Experiment-control module

The purpose of this module is to control the front-end system. This control has been implemented using the RS232 serial line connection. In a terminal window, PhyDAS commands can be directly executed and the status of the front-end system is displayed. In this

way, all commands and routines from the front-end software (*e.g.* from the acquisition and control level described in section 1.4.2) are available. Integration with the GUI of COLUMBUS has not been implemented yet.

### 3. Monitoring module

This module takes care of visualization of acquired data. This can either be on-line, to monitor experiment progress, or off-line, to replay the experiment afterwards in order to generate other or better graphics. The graphics are generated from the acquired list-mode and histogram-mode data-files on disk, based on the monitoring demand settings in the database.

If necessary, list-mode data can be pre-processed to calculate the derived parameters from the experimental parameters. Instead of including a fixed set of equations (functions) into the COLUMBUS code, a routine has been written that interprets equations from user input. The available set of operators includes +, -, \*, /, MOD, DIV. The user-defined equation is applied to the list-mode data of the appropriate set of experimental parameters. Until this routine has been integrated into the database and monitoring modules of COLUMBUS, which is not straightforward, it can be run off-line only. The resulting data set is stored in a new list-mode file, which can be used for monitoring or further processing.

Several graphic types are available during monitoring: single parameter histograms (from histogram-mode data or calculated from list-mode data), 2-D scatter-plots (two coincident list-mode parameters plotted vs. each other, or histograms vs. header parameters, like time or dose), and count-distribution plots (a special type of scatter plot when using the scanning microprobe). Count intensities are plotted in gray or in color scale. Basic graphic manipulation is available, like scale selection, zooming, region-of-interest (ROI) selection of a channel interval (window) or pixel area (contour), saving of histograms and scatter-plot data, and printing of graphics. On-line axis projections of ROI windows and contours allow for simple on-line analyses, like time- or dose-evolution studies. On-line graphics, with channel thresholds and windows on various parameters, are also supported from within the database.

The number of graphics is limited by computer capacity only. Although a larger number of graphics will slightly increase the delay between measurement and graphic display of the data, this will never interfere with the actual measurement. As mentioned above, the acquisition and storage of data is namely performed autonomously by the front-end system. The back-end system will not start monitoring this data until it has been stored safely on disk by the front-end system and the data server.

### 4. Off-line analysis module

This module converts data into ‘final’ results, through analysis of the measurement, based on the analysis demand in the database. External programs may be used and results are stored in the database.

Current options are: conditional sorting of list-mode data into histograms, histogram analysis like filtering, smoothing, calibration, peak identification and fitting, calculation of derived

parameters, and calculation of elemental concentration distributions and depth profiles. The computer codes that perform these analyses are partly from external sources and partly developed within our group. Most of these codes will be or have been integrated into COLUMBUS.

## 1.6 System performance

### 1.6.1 Front-end acquisition

Currently, our PhyDAS systems are equipped with three MCA boards. In histogram-mode, up to six experimental parameters can be measured at the same time, each with a count-rate up to at least 65 kcps. In list-mode, up to three pairs of coincident experimental parameters can be handled. An additional scan-position experimental parameter for each of the three MCA interfaces is available, when using the scanning microprobe. A list-mode measurement with three energy and three position experimental parameters, each with a count-rate of over 7.5 kcps, has been handled successfully. The requirement of six times 10 kcps may be feasible in the near future, since currently the count-rate is limited by the speed of the data-server (see below).

Our typical time interval of data acquisition  $\Delta t_{sample}$  is 60 s, after which the MCAs are stopped for reading the histogram and list-mode memories together with the acquired charge. Next, the MCAs are restarted for further acquisition. Data-transfer to the back-end system is done after restarting data acquisition and consequently does not affect the measurement time (see below). The effective transmission speed for histogram data is about 5.5 kbyte/s, which is limited by the speed of ASCII-based I/O from the PhyDAS. Histogram data is saved in ASCII-based files to ensure compatibility with existing off-line analysis programs. On the other hand, for binary list-mode data, typical transfer speeds are about 120 kbyte/s. This is limited by data server performance, the amount of Ethernet traffic, or occasionally reduced speed of disk access. File creation and closure, normally, takes about 0.4 s. Hence, storage of a 4096 channel 32-bit histogram takes about 3.3 s. Storage of  $10^5$  events of list-mode data for one 16-bit parameter takes about 2.0 s.

Fig. 1.7 shows the time diagram of data acquisition, combined for histogram-mode and list-mode experiments. All times are estimates based on multiple timing measurements.

For our typical experiments (three histograms, or six list-mode experimental parameters), the measurement off time is less than 400 ms, mainly determined by the readout time of the Keithley programmable electrometer. With a time interval  $\Delta t_{sample}$  of 60 s, this gives a measurement off/on ratio of less than 1%. Therefore, use of beam time is effective. If necessary, the measurement off time can be reduced further by using the Ortec current digitizer instead of the Keithley. At beam currents below 1 nA, however, the accuracy of the charge measurement with the Ortec decreases, due to large errors in current integration resulting from leakage currents.



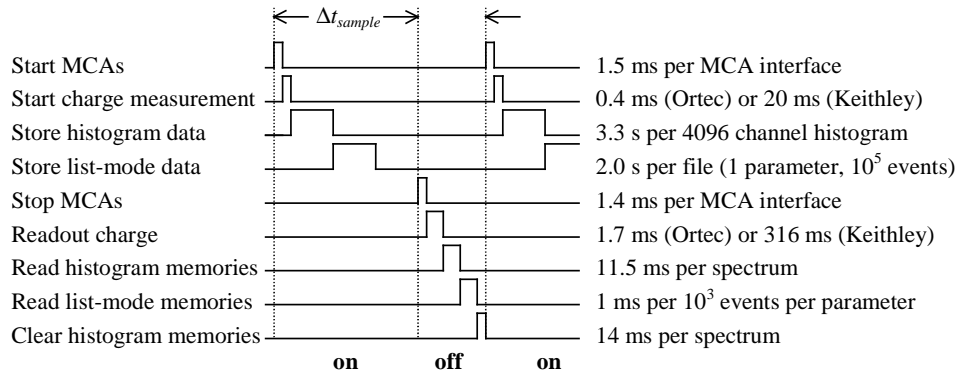


Fig. 1.7: Time diagram of data acquisition by the front-end system

Data storage generally takes less than 12 s, which is considerably shorter than the measurement time interval. However, if data storage has not completed, the measurement time interval is automatically extended.

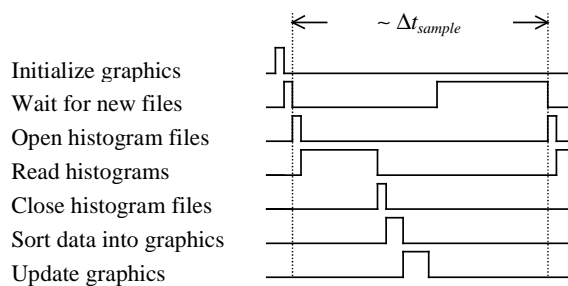
### 1.6.2 Back-end monitoring

Fig 1.8 shows the time diagram of data-monitoring by the back-end system. For clarity, this has been split into histogram-mode and list-mode data monitoring.

The histogram time diagram is shown in Fig. 1.8a. After initialization of the graphics, COLUMBUS repeatedly tries to open the first data files. It has to wait until the front-end system has stored these files on disk. Histogram files are then entirely read into memory, after which they are closed. The histogram data is sorted into the graphics data arrays, after which the on-screen graphics are updated. COLUMBUS then waits again until the next set of histogram files is accessible.

The list-mode time diagram is shown in Fig. 1.8b. List-mode data files cannot be read entirely into memory. To minimize file I/O, blocks of list-mode data are read into memory buffers. From these, the data is sorted into graphics, which are updated after a certain amount of events has been processed. Empty buffers are re-filled with new data from the files on disk. Upon an end-of-file, the data files are closed. The remaining buffered data is sorted into the graphics and COLUMBUS waits for the next set of list-mode files.

Each of the steps in the monitoring takes a few seconds at most. Exact timings cannot be given, since variations in the time of the steps are too large. Generally, COLUMBUS can easily keep up with the experiment. Only in case of simultaneous disk access by the front-end and back-end system, a large number of high-resolution scatter-plots or count-distribution plots, or a high workstation CPU usage, the time to process one set of files may increase to tens of seconds. Notice, however, that this does not affect data acquisition by the front-end system.



*Fig. 1.8a: Time diagram of histogram data monitoring by the back-end system*

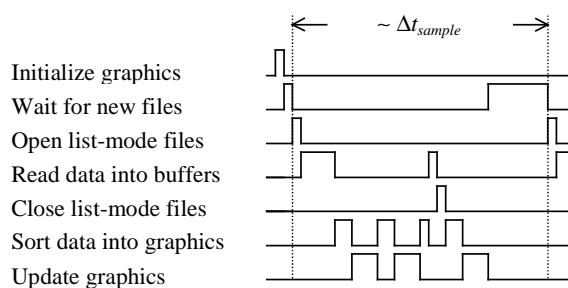


*Fig. 1.8b: Time diagram of list-mode data monitoring by the back-end system*

## 1.7 Applications

In this section, four types of experiments are described in which the multi-parameter data-acquisition system will show its value.

- An IBIC measurement using the microprobe set-up, to illustrate the use of beam scanning and the on-line generation of count-distribution plots from list-mode data,
- A typical angular-scan measurement using the channeling set-up, to illustrate the use of automated set-up control and the on-line analysis of channeling minimum-yield curves from histogram-mode data,
- A radiation damage measurement on organic samples, showing hydrogen and oxygen loss, to illustrate on-line analysis of time- and dose-dependent processes,
- An ERDA Pulse-Shape-Discrimination (PSD) experiment in the scattering set-up, to illustrate the on-line display and preliminary analysis of a multi-parameter list-mode experiment.

### 1.7.1 A scanning ion microprobe IBIC experiment

The on-line generation and display of both pulse-height histograms and count-distribution plots has become indispensable in scanning microprobe measurements. This will be illustrated by one of the IBIC experiments that were performed to study radiation damage effects in silicon particle detectors [10].

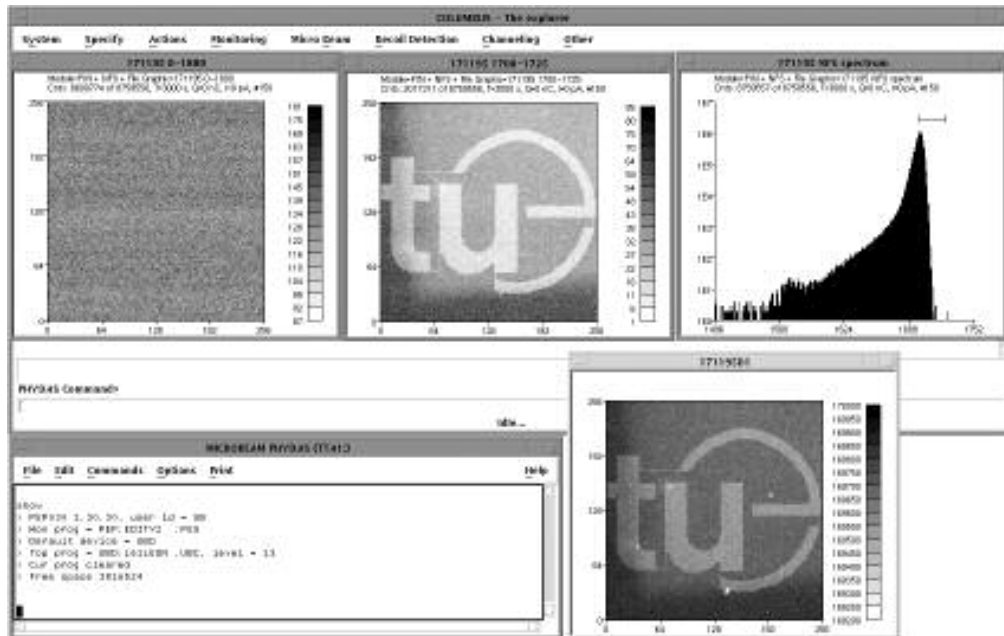


Fig. 1.9: Screen capture of COLUMBUS during the scanning microprobe IBIC experiment of our university logo.

A particle detector, at nominal bias, is mounted in the target wheel of the microprobe set-up and can be irradiated at normal incidence, in this case with a 4 MeV helium microbeam. First, the detector is irradiated, while the beam spot ( $3 \times 3 \mu\text{m}^2$ ) repeatedly scans the pattern (our university logo in this example) to damage the detector selectively. This is done, until each of the scan positions (16385 positions) has been irradiated with a certain amount of ions (in this case about 400 ions/pixel). Next, a square area that overlaps the damaged (logo) area is scanned, and the detector pulse-height response of several ions for each scan position (here  $\sim 130$  ions/pixel) is recorded in list-mode.

Fig. 1.9 shows the COLUMBUS screen during this measurement, together with the PhyDAS command window in the bottom-left corner. In the top-left corner, the count-distribution plot of all events is shown. On average, 130 ions have been recorded per scan position and no structures are visible in the distribution. In the top-right corner, the pulse-height histogram is shown, as generated on-line from the list-mode data, summed over all positions. The histogram shows a large peak with a centroid energy that corresponds to the beam energy. For some ions, however, a lower energy value is measured, as can be seen from the low-energy tail of the peak, a part of which supposedly is caused by radiation damage. Based on the pulse-height histogram, a narrow channel interval enclosing the upper part of the main peak can be selected (channel 1700-1725, as indicated by the bar in the histogram). This is used to define a new conditional count-distribution in the monitoring demand, after which monitoring is restarted. This new distribution should reveal areas that contribute to the main peak and, by contrast, areas that contribute to the low-energy tail. In the resulting top-middle graphic the university logo appears, which practically does not show any yield within the selected energy range. More accurately this can be seen from the result of off-line filtering analysis, which is shown in the bottom-right graph. Here, the average pulse-height response for each scan position is plotted. The logo area clearly displays a lower pulse height response (white) due to the previous selective damaging. Obviously, particle detectors are very susceptible to radiation damage. This is illustrated by the background (light gray) square region with reduced pulse height behind the logo, which is probably due to radiation damage from a previous STIM experiment.

### 1.7.2 A channeling angular-scan measurement

The data-acquisition system is routinely used for channeling experiments. Here, a  $\langle 111 \rangle$  angular scan measurement on a MBE-grown GaAs/AlGaAs/InGaAs/GaAs heterostructure [12] will be discussed. A 4 MeV  $\text{He}^+$  beam is used, which impinges on the sample around 54 degrees with the sample normal.

After the sample has been aligned with the incoming beam [12], pulse height histograms are acquired in histogram-mode for both the RBS channeling detector (at 170 degrees) and the rotating-vane detector in the beam line. Each histogram is acquired during a fixed time interval of 300 s. This is done automatically 42 times: after each measurement, the sample is

rotated by 0.05 degrees around the vertical axis. This gives a total rotation angular scan range of 2.1 degrees.

The top-left graph in Fig. 1.10 shows the pulse-height histogram of the RBS channeling detector, summed over all 42 measurements. This histogram displays a small In peak near channel 600, just above the large Ga and As ridge. Right next to this graph, the sum histogram of the rotating-vane detector is displayed. This features a large contribution from the 4.5  $\mu\text{m}$  gold coating on the rotating vane (the Al signal is absent due to the thick Au layer). The top-right window is the PhyDAS command window, which shows the goniometer control menu, including the status of the tilt, spin, and rotation axis values.

COLUMBUS can generate an on-line visualization of the angular scan. The scatter-plots in the middle row of Fig. 1.10 each display the 42 measured histograms vs. the rotation angle. This angle corresponds to the vertical axis; the color scale corresponds to the yield. From left to right, the shown scatter-plots are: the RBS channeling detector data, the rotating vane detector data, and the RBS channeling detector data normalized to the integral yield of the rotating-vane detector. The latter is calculated using an external program, after which the data is read into COLUMBUS.

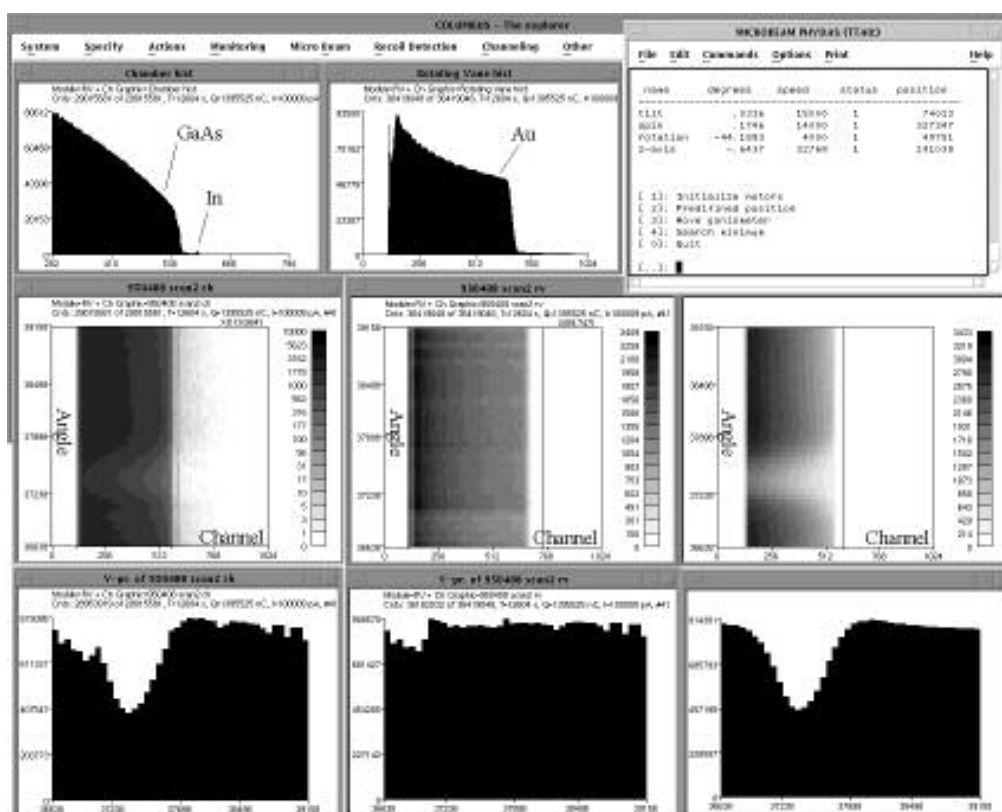


Fig. 1.10: Screen capture of COLUMBUS during a channeling experiment.

A region-of-interest (ROI) can be selected in the scatter-plots (channel window in the histograms on the horizontal axis), which corresponds to a certain element and depth interval. The data in this ROI can then be projected onto the vertical angle-axis, which gives an angular scan with one or more channeling minimum-yield dips. This is shown in the bottom row of histograms in Fig. 1.10. The bottom-left histogram shows the 'raw', on-line preview of the GaAs angular scan, created using the non-normalized measurement data. The bottom-middle histogram displays the beam dose fluctuation as a function of rotation angle. The bottom-right histogram displays the normalized GaAs angular scan with a smooth minimum-yield dip that can be analyzed further [12].

### 1.7.3 Time- and dose-dependent list-mode measurements

Radiation damage studies require time- and dose-dependent measurements. Here, an example is given of a radiation-damage experiment to study the effect of a 3 MeV proton microbeam on a  $0.7 \text{ mg/cm}^2$  poly-carbonate ( $\text{C}_{16}\text{H}_{14}\text{O}_3$ ) foil, which can be regarded as a model system for biological tissue. The beam spot size is  $(19 \times 14) \mu\text{m}^2$ , and the beam current is about 4.6 nA. While irradiating the sample at a fixed spot, the front-end system acquires a series of histogram files from the NBS detector (147 degrees) and the NFS detector (45 degrees), during measurement time intervals of 15 s. After one hour of irradiation, the total charge is about  $16.5 \mu\text{C}$  and the areal dose almost  $4 \cdot 10^{19}$  protons/cm<sup>2</sup>.

Fig. 1.11 shows the on-line COLUMBUS screen. The top-left graph shows the histogram of the NFS detector, summed over all time intervals, with the hydrogen peak on the left side and the combined carbon and oxygen peak on the right. Below this graph, the histogram of the NBS detector, summed over all time intervals, is displayed. This shows a large peak from carbon and a small peak from oxygen.

Instead of adding the 240 histograms up to a sum histogram, they can also be plotted vs. their file number or vs. cumulative dose. The top-middle graph shows the on-line scatter-plot of the H peak in the NFS histogram vs. its file number. In the middle graph, the same is done for the NBS histograms, zoomed into the ROI around the C and O peaks. In order to study radiation-damage effects, one likes to obtain elemental yield vs. cumulative dose. This can also be done on-line; the right-hand side scatter-plots show the NBS and NFS histograms as a function of dose. The unequal vertical spacing between histograms is caused by dose variations. Notice that all histograms are normalized to dose, on-line.

To plot elemental yields vs. dose, a ROI enclosing the element of interest can be defined in the scatter-plots (see vertical lines in Fig. 1.11). Projection of the ROI contents onto the cumulative dose axis gives the required elemental yield vs. dose plots. The bottom-row graphs of Fig. 1.11 display, from left to right, the normalized hydrogen, carbon, and oxygen yield as a function of the dose. Hydrogen and oxygen appear to be volatile, whereas the carbon signal, after a short initial decrease, shows an increase that is attributed to residual carbon deposition by the ion beam. Further analysis, including curve fitting, can be done off-line.

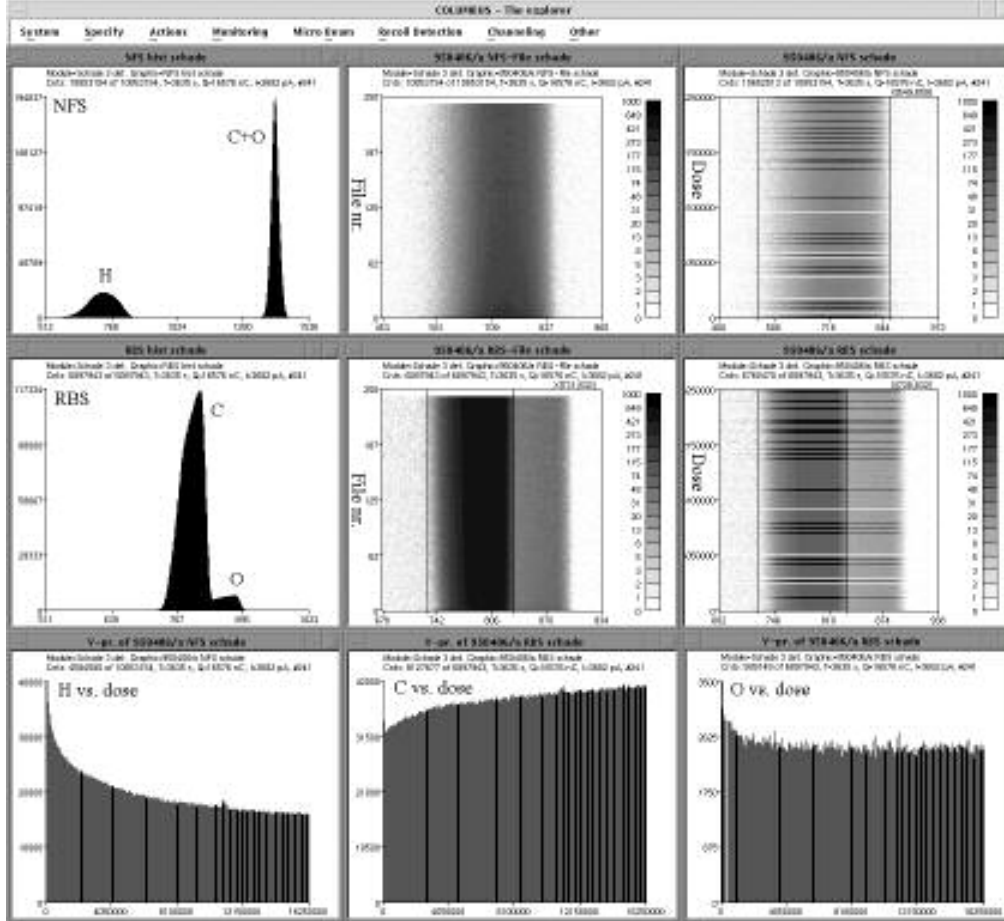


Fig. 1.11: Screen capture of COLUMBUS during the radiation damage measurement

#### 1.7.4 An ERDA-PSD experiment

Multi-parameter acquisition is indispensable for coincident ion-scattering experiments. This is illustrated by a typical ERDA-PSD experiment. The ERDA technique is based on the detection of particles that are recoiled from the sample. However, when using helium ions as projectiles, many of these also scatter, hit the forward recoil detector, and thereby obscure the recoil signal. To discriminate between recoils and the scattered projectiles, the PSD technique is applied. This technique provides a charge-collection-timing signal in addition to the energy pulse-height signal(s) from the recoil detector [16].

Fig. 1.12 shows the COLUMBUS output screen during the ERDA-PSD measurement on a 400 nm thin  $\text{SiO}_2$  film that was thermally grown on a silicon substrate. In list-mode three experimental parameters are recorded in coincidence. The charge-sensitive pre-amplifier signal from the recoil detector is fed to two shaping amplifiers with a shaping time of 1.0  $\mu\text{s}$

( $E_{rec1}$ ) and  $0.25 \mu\text{s}$  ( $E_{rec2}$ ), respectively. Using a fast-timing circuit, a third experimental parameter (*timing*) is obtained. As described in [16], this *timing* is expected to be small (fast) for recoils, and large (slow) for scattered helium ions with the same energy as the recoils, thus enabling discrimination. Each of the three coincident signals is fed to an MCA input. Typically, count-rates are limited to 4 kcps, and often the pulse-height signal from an RBS detector is recorded, for normalization purposes, on a separate MCA.

From the list-mode data, three 2-parameter scatter plots can be created, as shown in the top row of Fig. 1.12. From left to right: *timing* vs.  $E_{rec1}$ , *timing* vs.  $E_{rec2}$ , and  $E_{rec2}$  vs.  $E_{rec1}$ . In all graphs, a high-intensity curved feature can be seen, that originates from the many scattered helium projectiles. The scatter contribution appears to be nicely separated from the recoil contribution of interest. In the first two graphs, the oxygen recoil signals lie on an almost straight line, at small *timing* values. In the third graph, they lie on a line with  $E_{rec1}:E_{rec2} = \text{constant}$ .

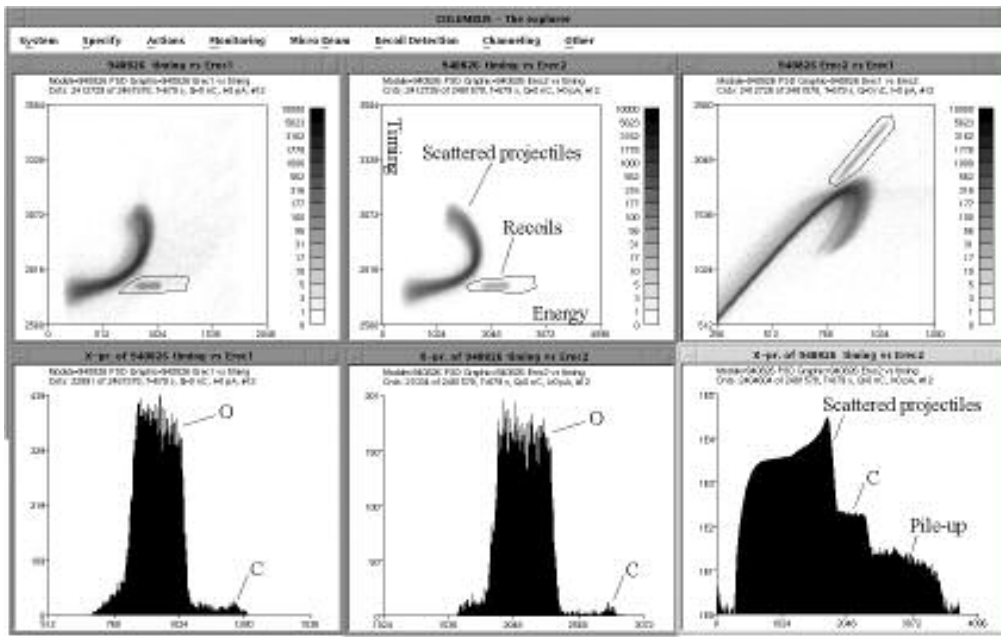


Fig. 1.12: Screen capture of COLUMBUS during an ERDA-PSD measurement.

The need for multi-parameter acquisition can be seen from the following: if only the energy experimental parameters had been recorded, an energy histogram as shown in the bottom-right graph would have been obtained. In that case, oxygen profiling based on recoil signals is hindered by the huge contribution of scattered ions at the low energy side and an associated pulse pile-up background at the high-energy side. In multi-parameter acquisition, on the other hand, the 2-parameter scatter plots allow for on-line selection of only the recoil contribution, via a ROI contour drawn around this contribution. Projection of the contents of this ROI onto



the energy axis gives a ‘clean’ recoil histogram. The result is shown in the two bottom-left histograms, for  $E_1$  and  $E_2$ , respectively. A clear oxygen profile is seen, together with a small peak due to carbon surface contamination. A similar recoil histogram can be obtained by selection of the recoils in the  $E_{rec_2}$  vs.  $E_{rec_1}$  plot. In this case, just two energy experimental parameters without fast-timing electronics are sufficient for efficient recoil selection.

Other experiments in our scattering set-up, that have become feasible through the multi-parameter data-acquisition system, include time-of-flight experiments, energy- and position-sensitive detector experiments, and dE-E telescope experiments.

## 1.8 Conclusions and recommendations

A multi-parameter data-acquisition system has been developed, which is now commonly used in our ion beam experiments. It supports all basic requirements: automated experiment control, acquisition of multi-parameter list-mode and histogram-mode data, on-line data visualization and preliminary analysis, highly integrated off-line analysis, and storage of all relevant experimental details in a database.

The system performance is satisfactory. Up to six (coincident) experimental parameters can be measured at the same time, either in histogram-mode or in list-mode. In histogram-mode, count-rates up to 65 kcps per experimental parameter have been handled successfully. In list-mode, count-rates up to 7.5 kcps per experimental parameter can be dealt with. The latter is mainly limited by the current data-server performance, and can easily be improved if necessary.

The acquisition and storage of data have been separated from the on-line visualization and off-line analysis. The advantage of this separation is that undisturbed real-time performance of acquisition is ensured. In general, the on-line monitoring can easily keep up with the experiment and the acquisition of data.

One of the recommendations for future versions is to enhance set-up control of the front-end system by the back-end system. However, this is not straightforward with the current communication between the front- and back-end system via the serial line. Furthermore, it is difficult for the front-end system to initiate communication with the back-end system. This prevents the front-end system from directly accessing the COLUMBUS database and from triggering the back-end system for the availability of new data. An improved communication and synchronization mechanism between the front-end and back-end system thus is recommended.

Another recommendation is to fully integrate the storage of user-editable functions and equations into the database and their interpretation in the monitoring module of COLUMBUS. This will greatly increase the on-line graphics generation and preliminary data analysis.

Last but not least, it is foreseen that with increasing computer power, but especially with smart ‘dynamic analysis’ algorithms, in the near future, final results of data analysis may be obtained on-line.

## References

- [1] P.H.A. Mutsaers, Design and Realisation of the Eindhoven Scanning Proton Microprobe, (Ph.D. Dissertation, Eindhoven University of Technology, 1995).
- [2] P.H.A. Mutsaers, D.P.L. Simons, Nucl. Instr. and Meth. B130 (1997) 127-132.
- [3] W.-K. Chu, J.W. Mayer, M.-A. Nicolet, Backscattering Spectrometry, (Academic Press, New York, 1978).
- [4] J. L'Ecuyer, C. Brassard, C. Cardinal, J. Chabbal, L. Deschenes, J.P. Labrie, B. Terreault, J.G. Martel and R. St-Jacques, J. Appl. Phys. 47 (1976) 381.
- [5] M.P. de Jong, D.P.L. Simons, M.A. Reijme, L.J. van IJzendoorn, A.W. Denier van der Gon, M.J.A. de Voigt, H.H. Brongersma, and R.W. Gymer, to be submitted to Synth. Metals.
- [6] S.A.E. Johansson and J.L. Campbell, PIXE A Novel Technique for Elemental Analysis, (Wiley, New York, 1988).
- [7] J.A. Quaedackers, R.M.G.J. Queens, P.H.A. Mutsaers, J.J.M. de Goeij, G.J. van der Vusse and M.J.A. de Voigt, Nucl. Instr. and Meth. B139 (1998) 169-174.
- [8] H.W. Lefevre, R.M.S. Schofield, G.S. Bench and G.J.F. Legge, Nucl. Instr. and Meth. B54 (1991) 363-370.
- [9] M.B.H. Breese, G.W. Grime and F. Watt, J. Appl. Phys. 72 (1992) 2097.
- [10] D.P.L. Simons, A.J.H. Maas, P.H.A. Mutsaers and M.J.A. de Voigt, Nucl. Instr. and Meth. B130 (1997) 160-165.
- [11] L.C. Feldman, J.W. Mayer and S.T. Picraux, Materials Analysis by Ion Channeling, (Academic Press, New York, 1982).
- [12] P.W.L. van Dijk, A High-energy Ion Channeling Facility and its Applications, (Ph.D. Dissertation, Eindhoven University of Technology, 1997).
- [13] Physical and Technical Laboratory Automation Group, Department of Applied Physics, Eindhoven University of Technology, P.O. Box 513, 5600 MB Eindhoven, The Netherlands.
- [14] The VMEbus Specification, ANSI/IEEE Std. 1014-1987.
- [15] J.H. Voskamp, F.C. van Nijmweegen and A.J. van der Wal, Nederlands Tijdschrift voor Natuurkunde, A55(1/2) (1989) 50 (in Dutch).
- [16] A.J.H. Maas, S.S. Klein, D.P.L. Simons and M.J.A. de Voigt, Nucl. Instr. and Meth. B118 (1996) 268.

## Chapter 2

# Exploration of X-ray and charged-particle spectroscopy with CCDs and PSDs

*Generally, in scanning ion microprobe set-ups, use is made of Si(Li) detectors or ultra-pure Ge detectors for X-ray spectroscopy, and of surface barrier detectors or PIPS detectors for charged-particle spectroscopy. In this work, two alternative detector types have been studied for use in the Eindhoven scanning ion microprobe set-up. First, the applicability of a charge-coupled device (CCD) system to X-ray spectroscopy has been explored. Second, some properties of the SiTek type 1L30 position sensitive detector (PSD) for charged-particle spectroscopy have been studied.*

*A literature survey shows that excellent X-ray spectroscopy with a CCD system is feasible, particularly with a deep-depletion backside-illuminated CCD and low speed readout. From this study, however, it was also found that if a high-speed CCD readout is required, such as for scanning microprobe experiments, a CCD system cannot be used for spectroscopy due to excessive readout noise.*

*For the PSD, noise-theory calculations are presented, which result in a noise shaping time for optimal energy and position resolution. In practice, however, a much longer time is needed to obtain sufficient energy and position linearity. Characterization measurements of the PSD using our 4 MeV He<sup>+</sup> microprobe are also described. A position resolution of 0.47 mm and a position linearity of better than 0.15% of the detector length are found. In addition, an energy linearity better than 0.3% and an energy resolution of 36 keV are measured. The latter should be improved, to make the PSD suitable for charged-particle spectroscopy applications.*

Related publication: "Exploration of X-ray and Charged-Particle Spectroscopy with CCDs and PSDs", D.P.L. Simons, P.H.A. Mutsaers, L.J. van IJendoorn, M.J.A. de Voigt, Nucl. Instr. and Meth. B139 (1998) 273-278.

## 2.1 Introduction

X-ray and charged-particle spectroscopy are techniques that are widely used in ion-beam analysis experiments. The aim of this work is to study alternative detector types for spectroscopy in the scanning ion microprobe set-up [1], in order to overcome limitations of the currently used detectors.

In section 2.2, the choice of an alternative detector type for both X-ray spectroscopy and charged-particle spectroscopy is made and motivated. In section 2.2.1, it is shown that a charge-coupled device (CCD)-based detector is a candidate for improved X-ray spectroscopy over a conventional Si(Li) detector, especially for low-energy ( $<1$  keV) X-ray spectroscopy. In section 2.2.2, it is shown that a position sensitive detector (PSD) based on the resistive charge-dividing mechanism is a candidate for improved charged-particle spectroscopy over a conventional energy-disperse detector.

In section 2.3, the applicability of CCDs as X-ray detectors for PIXE in a microprobe set-up ( $\mu$ PIXE) is studied. In section 2.4, some properties of the SiTek [2] type 1L30 PSD for charged-particle spectroscopy are studied. Conclusions are given in section 2.3.3 for the CCD and in section 2.4.7 for the PSD.

## 2.2 Alternative detector types

### 2.2.1 X-ray spectroscopy

X-ray spectroscopy is used in various diagnostic applications. One of these is the particle induced X-ray emission (PIXE) technique [3], where X-ray spectroscopy is used to perform (trace-)elemental analysis. If PIXE is applied in a scanning ion microprobe set-up ( $\mu$ PIXE), elemental concentration distribution maps at micrometer-scale can be obtained [1].

For X-ray spectroscopy, commercially available  $\text{LN}_2$ -cooled Si(Li) or ultra-pure Ge detectors are often used. These offer a good energy resolution, system-noise limited to about 130 eV Full Width at Half Maximum (FWHM) for the Mn-K $\alpha$  line, due to rather large crystal size and detector capacitance.

However, one major disadvantage of Si(Li) detectors, at least for the detection of light elements ( $Z < 11$ ) using PIXE, is the presence of an entrance window (for example 8  $\mu\text{m}$  beryllium). This window shields the detector crystal, which is liquid-nitrogen cooled, from the vacuum chamber. This prevents crystal icing from (residual) water vapor in the vacuum chamber. Hence, the detection efficiency for X-rays with energies below 1 keV is reduced significantly and PIXE is limited to trace-element detection of sodium and heavier elements. Efficient detection of low-energy (soft) X-rays from sodium and magnesium, which are biomedically-interesting elements, remains difficult. Efforts have been made to increase the detection efficiency of a Si(Li) detector for low-energy X-rays by using ultra-thin entrance windows. In ref. [4], for example, a 0.25  $\mu\text{m}$  boron-nitride window is used, but there it is

found that icing problems due to residual water vapor within the vacuum inside the detector limit the detection efficiency of soft X-rays significantly.

Alternative detector systems for X-ray spectroscopy include wavelength disperse spectrometers (WDS) [5] and silicon drift detectors (SDD) [6]. Although a WDS has a much better energy resolution than a Si(Li) detector, which results in better adjacent peak separation and enhanced signal-to-background ratios, its detection efficiency is very low and only a limited part of the spectral range can be recorded simultaneously.

Initial reports on X-ray spectroscopy with silicon drift detectors are very promising. Their energy resolution performance at room temperature approaches that of a Si(Li) detector at cryogenic temperatures. Drift detectors are, however, relatively new and not readily available. In this work, the applicability of charge-coupled devices (CCDs) to (low-energy) X-ray spectroscopy is studied, especially for use in  $\mu$ PIXE applications. This is inspired by the progress that has been achieved in low-energy X-ray spectroscopy with CCDs in the field of astronomy [7]. Enhanced detection efficiencies for soft X-rays are reported, through windowless detection and use of special deep-depletion, backside illuminated devices. At the same time, excellent energy resolutions are obtained, through on-chip amplification, mild cooling and special readout algorithms, which make use of the position sensitivity of the CCD. The applicability study of CCD-based X-ray detectors for use in the scanning ion microprobe that was performed in this work will be described in section 2.3.

### 2.2.2 Charged-particle spectroscopy

For charged-particle spectroscopy, as applied in ion-scattering techniques like Rutherford back-scattering spectroscopy (RBS) [8], conventionally energy-disperse diode-detectors are used, such as surface barrier detectors (SBD) and p-n diode detectors [9]. Especially the passivated implanted planar silicon (PIPS) detectors, manufactured by Canberra [10], display an excellent energy resolution, like 10 keV FWHM for 6 MeV alpha particles [11]. The counting statistics are, however, typically low. Enlargement of the detector solid angle improves the counting statistics, but is likely to worsen the energy resolution. This is caused by the increased system noise, which is inherent to a larger detector, and by the increased kinematic spread of the incoming ions. The latter can be corrected for if the detector is scattering-angle-disperse, in addition to energy disperse.

Detectors that are both energy- and position sensitive include the CCD, the silicon strip and pixel detectors (SSD/SPD), silicon drift detectors (SDD), and resistive charge-dividing position sensitive detectors (PSD).

In section 2.3, where X-ray spectroscopy with a CCD is discussed, it will be shown that a CCD is not suitable for detection of charged particles. This is caused by limitations in radiation hardness, depletion layer depth, full-well capacities, and readout speed.

The SPD and SSD are one and two-dimensional position sensitive detectors, respectively. These discrete detectors, that consist of an array of isolated diodes, are widely used as fast

tracking-devices in high-energy physics. Only a few applications in charged-particle spectroscopy have been reported. Rosenfeld *et al.* [12] report on a  $7 \times 7 \text{ mm}^2$  strip detector with an energy resolution for each strip of about 20 keV for 5.8 MeV alpha-particles and a position resolution of  $1 \text{ }\mu\text{m}$ . However, to obtain this (noise) performance, each of the 28 strips has to be connected to an external amplifier chain. Therefore bulky electronics is necessary. Furthermore, the noise performance of strip detectors is in general strongly dependent on the strip geometry [13] and must be optimized for each application.

The SDD has been developed very recently [14]. One-dimensional position information is deduced from the drift time of the electrons from the point where they are freed by the incoming radiation to the collecting anode. Two-dimensional position sensitivity can be obtained by segmenting the collecting anode. Thus, in contrast to the SSD, it has a very small number of output signals. The detector has a low capacitance and the first transistor can be integrated on-chip, which allows for low noise levels. However, to ensure good position resolution and linearity, both temperature stabilization and very pure and homogeneous silicon are required, in addition to an extensive calibration procedure. The SDD is very sensitive to radiation damage. The induced inhomogeneities will reduce position resolution and linearity. Furthermore, the detector leakage current, that is already quite high, will increase further. This makes the detector less suitable for charged-particle detection.

The simplest energy- and position-sensitive silicon detector is based on the resistive charge-dividing principle [15]. The detector consists of a silicon p-n diode, where the front electrode is made of a continuous resistive layer. This results in a one-dimensional position-sensitive detector. Optionally the backside may also be made resistive, giving a two-dimensional position-sensitive detector. The charge that is collected on an electrode is divided over the two contacts at the opposite edges of the resistive electrode layer. The ratio of charge division depends on the position of incidence. Hence, only two signals are sufficient to obtain the position information in one dimension. The energy signal is obtained from the backside electrode or optionally from the sum of two front-side position-contact signals. This PSD is widely used for laser-light tracking, but it has been shown that this type of detector can also be used for charged-particle spectroscopy. Lindroos *et al.* [16] used a  $12.2 \times 12.2 \text{ mm}^2$  commercially available 2-D PSD for alpha particle spectroscopy. They achieved an energy-resolution of 16.2 keV FWHM for 5.8 MeV alpha particles and a position resolution of  $70 \text{ }\mu\text{m}$  FWHM.

Based on the above overview, it is concluded that the PSD based on the resistive charge-dividing process is the most flexible and suitable choice for energy- and angle-disperse charged-particle spectroscopy in our ion-beam analysis applications. In section 2.4, the theoretical and experimental characterization of a commercially available PSD, the SiTek [2] type 1L30, is described.

## 2.3 X-ray spectroscopy with a CCD

### 2.3.1 CCD operation principle

The CCD is a discrete pixel detector, which can be made either one-dimensionally or two-dimensionally position-sensitive. It has originally been developed as an optical imaging sensor for video applications, which still is its main application. It has, however, also successfully been used for X-ray spectroscopy [7], mainly in the field of astronomy.

The most common type of CCD is the metal-oxide-semiconductor CCD (MOS-CCD). This type of CCD consists of a p-type silicon substrate covered with an insulating dielectric (oxide or nitride) layer and an array of oxide-isolated poly-silicon control electrodes (gates) (see Fig. 2.1). An n-type layer is present, either directly below the front electrode structure (surface channel) or a few  $\mu\text{m}$  below the front electrode-structure (buried channel). Applying a positive voltage to an electrode creates a potential well below this electrode within the (buried) layer. The well depth is controlled via the voltage applied to the electrodes, and the remaining region of the silicon substrate remains field free and thus undepleted. By applying different voltages to neighboring electrodes, potential wells in which charge can be stored are created below the electrodes. In this way, a one-dimensional array of charge storage elements is obtained. To create a two-dimensional matrix of storage elements, channel-stops of p-type silicon are diffused into the buried layer to divide this layer into separate columns.

Electrons that are freed by incoming ionizing radiation will drift and/or diffuse to the ‘deepest’ potential wells below the electrodes, in which they are then stored. Mostly a buried instead of surface channel is used, because in that case stored electrons are pulled away from the dielectric layer and trapping at the surface of this layer is reduced.

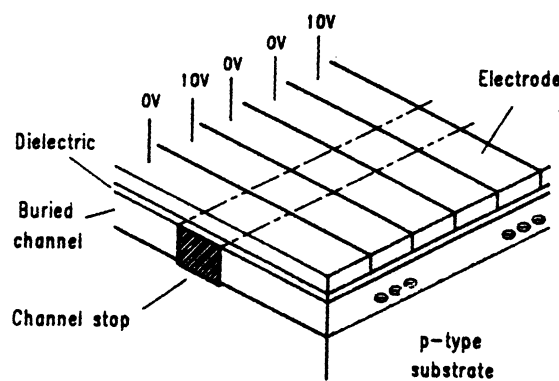


*Fig. 2.1: Schematic MOS-CCD cross section [17].*

*The typical dimension of the shown CCD area is  $20 \times 20 \mu\text{m}^2$ .*

A relatively new type of CCD is the pn-CCD [18]. This type differs from the MOS-CCD in that reverse-biased pn-diodes are used for the front-side electrodes together with a large pn-diode on the backside to fully deplete the CCD. Advantages of this type of CCD over the MOS-CCD are that it is sensitive to incoming ionizing radiation over the full detector thickness because of the full depletion, and that it is less sensitive to radiation damage than a MOS-structure. Its operation principles are similar to the MOS-CCD.

A basic 5×5-pixel CCD array is shown in Fig. 2.2. Here, each pixel corresponds to a charge storage element. In the vertical direction such an element is limited by three adjacent control electrodes and in the horizontal direction by the channel stops. This type of CCD is called a three-phase CCD.

The area in which incoming ionizing radiation can be detected forms the image section. All integrated charge that is stored in the pixels of this image section can simultaneously be transferred row-by-row in the vertical (parallel) direction by clocking the electrode voltages in a cyclical way via drive pulses. The electrons shift from pixel to pixel as a result of the *fringing field* drift between potential wells of neighboring electrodes.

Below the image section, a horizontal (serial) readout section is present. Charge from the bottom row of image-section pixels will be transferred into this readout section. Usually, before the next vertical row shift, the charge in the readout section is horizontally shifted, pixel-by-pixel, to the output register. In this way, the charge content of each individual pixel from the image section is serially clocked into the output register.

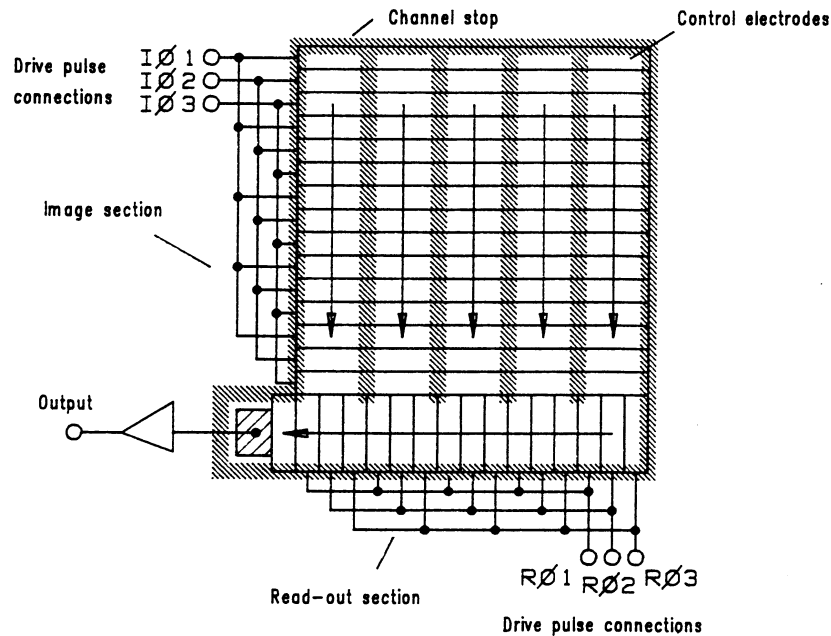


Fig. 2.2: Basic CCD array layout [17].



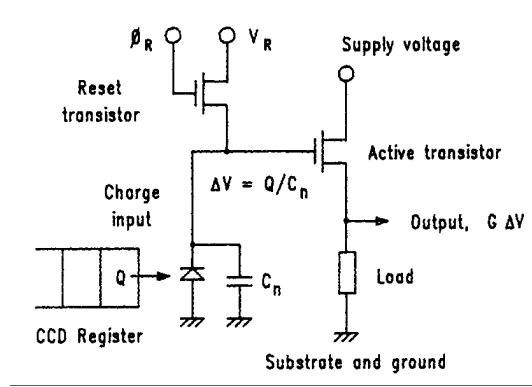


Fig. 2.3: CCD Charge-to-voltage output circuit [17].

Charge-to-voltage conversion is done on-chip at the output register and the associated output circuit (see Fig. 2.3). First, through a pulse on the reset gate  $\phi_R$  of the reset transistor, the voltage over the output node capacitance  $C_n$  is set to the reference voltage  $V_R$ . Next, the signal charge  $Q$  is clocked from the output register into the output diode. The voltage over the output capacitance  $C_n$  will decrease linearly with  $Q$ :  $\Delta V = Q/C_n$ . The source-follower, that consists of an active MOS-transistor and its load, will serve as an impedance buffer between the high diode impedance and the much lower impedance of the external electronics. It has a small output gain  $G$ , which results in an output voltage signal equal to  $GQ/C_n$ .

### 2.3.2 Aspects of CCD X-ray spectroscopy

With respect to the applicability of a CCD as a detector for X-ray spectroscopy, several aspects are relevant. The most important ones are: noise performance, energy resolution, detection efficiency, readout time together with event confusion and smearing, and radiation damage effects. Each of these aspects will be discussed in more detail.

#### *Noise performance and energy resolution*

For a CCD to compete with a conventional Si(Li) detector in X-ray spectroscopy, its noise performance and associated energy resolution should be comparable or even better. For a standard silicon detector the Full Width at Half Maximum (FWHM) energy resolution  $\delta E$  is given by equation 2.1 [9].

$$\delta E = 2.355 \cdot w \cdot \sqrt{n^2 + \frac{F \cdot E}{w}} \quad (2.1)$$

Here,  $n$  is the readout noise in electrons,  $F$  is the Fano factor (about 0.115),  $E$  is the photon energy (in eV), and  $w$  is the X-ray energy to charge conversion factor ( $w = 3.6\text{-}3.7$  eV per electron/hole-pair).

For a CCD, the most dominant factor of the readout noise is thermal ( $kTC$ ) noise from the reset transistor operation [17]. This noise can effectively be reduced using the correlated double sampling (CDS) technique [19]. This technique eliminates the influence of the thermal reset-voltage fluctuation, by taking the difference between the output signals sampled after reset and again after the signal charge has been transferred onto the output capacitor. Additional transistor noise consists of a white-noise component and a  $1/f$ -noise component. The  $1/f$ -noise component is independent of the readout speed and determines the noise floor at low readout speeds. For this slow-scan CCD operation, when pixel readout rates are low and sampling times are long ( $>1 \mu\text{s}$ ), the total Noise Equivalent Signal (NES) amounts to a few electrons rms. For high-speed CCD operation, the additional white-noise component increases the total readout noise to tens or hundreds of electrons rms for very short sampling times (see Fig. 2.4).

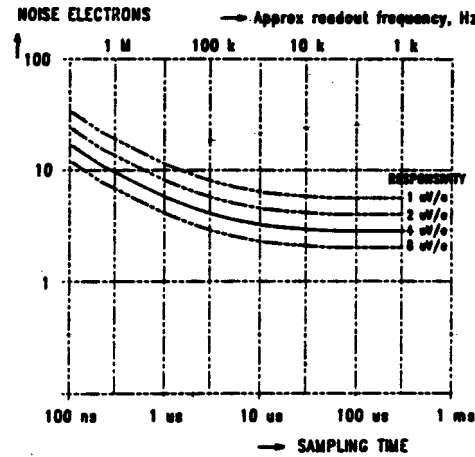


Fig. 2.4: Typical output noise performance of a CCD. Curves were calculated from transistor noise theory, for several responsivities, and agree well with measurement [from 17].

In slow-scan operation, with CDS, noise levels below 10 electrons rms can easily be achieved, corresponding to a system resolution of better than 85 eV, as can be calculated via equation 2.1. For example, Lumb [7] reports on a commercial  $450 \text{ mm}^2$  CCD, operated at  $T = 180 \text{ K}$  and clocked at  $\sim 35000$  pixels per second. The system noise here is about 6.5 electrons rms, resulting in an energy resolution of 120 eV for 5 keV X-rays.

Several other factors that affect the energy resolution, besides electronic noise, have to be taken into account. Charge carriers that have been freed in the depletion layer by an incoming X-ray photon will drift to the overlying potential well and generally all charge is confined to one single pixel. Charge carriers, however, that were freed in the field-free region, will not move to the potential wells by drift but by diffusion. They will also diffuse radially and charge clouds may split at pixel boundaries and divide over various neighboring pixels. To maintain an excellent energy resolution, the amount of 'split events' has to be minimized [20]. One way

to do this is to reduce the field free region by use of deep- or full-depletion devices. An other option is to match the pixel size to the desired level (fraction) of split events. The influence of split events may also be reduced by applying software event-recognition and reconstruction algorithms. Generally, however, the energy of reconstructed events appears to be somewhat lower than that of single-pixel events. Hence, the histogram structure and energy resolution are still affected. Selection of only single-pixel events will result in the best energy resolution. In this case, however, the detection efficiency will decrease, especially for those X-ray energies that have many interactions in the field free region. For each individual application, it has to be decided whether the gain in energy resolution balances the loss in detection efficiency. The latter may be as high as 35% [20].

The effect of split events can also be used advantageously for charged-particle discrimination during X-ray spectroscopy. Parasitic charged particles, with an energy in the order of an MeV, that hit the X-ray detector through scattering processes, deposit most of their energy at the end of their track. Because of radial diffusion effects, most charged particles will result in split events. Furthermore, the large amount of charge that is initially collected in the potential well of a single pixel will, because of limited full-well capacities, overflow into neighboring pixels and also result in split events. Charged-particle discrimination and rejection can thus be done either using an energy threshold after event reconstruction or based on the multiple-pixel signature itself. Note that the overflow of charge-storage elements in case of charged particles prevents a CCD from being used as a detector for charged-particle spectroscopy.

The energy resolution is also affected by charge transfer inefficiency (CTI). During the transfer of charge to the output register, every time charge is shifted to the adjacent pixel, a very small fraction of this charge is lost or left in the previous pixel, which results in charge trailing. The amount of charge lost due to CTI depends on the number of parallel and serial shifts for each pixel and therefore has a spatial distribution over the pixel array. In principle, if the CTI has been determined, a correction for charge trailing can be applied by using a pixel dependent function [7].

Last but not least, the energy resolution is affected by the thermally generated leakage current or dark current that adds up to the signal charge during charge integration. In this way, a shot-noise component is added to the output signal. This noise is proportional to the square root of the total number of integrated electrons. Furthermore, dark current can cause potential wells to saturate and overflow in case of very long integration times. Dark current has a strong temperature dependence, through which it can effectively be reduced. Roughly, the dark current decreases by a factor 2 for each 5 degrees of cooling. Operating temperatures in the range of 140-230 K will therefore be sufficient to reduce the dark current to acceptable levels. In summary, a CCD can give a very good, almost Fano-limited energy resolution, much better than that of a conventional Si(Li) detector. However, this requires cooled ( $\sim 200$  K), slow-scan ( $10^5$  pixels/s) operation, together with software event recognition and discrimination techniques.

### Detection efficiency

Detection efficiency should be as high as possible. It is determined by the detector solid angle, the detector quantum efficiency (QE), and event selection criteria.

CCD arrays can have active areas of several  $\text{cm}^2$ , much larger than the active area of a Si(Li) detector. An increased detector area, however, does not necessarily imply an increased detector solid angle. Notably in the microprobe setup, a CCD X-ray detector will have a maximum solid angle that is comparable to that of a conventional Si(Li) detector, because of the geometry of ion beam, sample, and detector.

The QE is defined as the detected fraction of all X-rays that hit the detector. Ideally, each X-ray hitting the detector should be detected, regardless of its energy. In practice, however, this is not the case. Commercial CCDs have been developed and optimized for optical wavelengths and have thin active layers. These active thicknesses are in the order of a few micrometers, which is much shorter than the attenuation length of high-energy X-rays ( $> 5$  keV). This results in a poor QE for high-energy X-rays and in event splitting. Moreover, the rather thick ( $\sim 1 \mu\text{m}$ ) front-side electrode structure results in a low QE for soft X-rays ( $< 1$  keV). In summary, the quantum efficiency of standard CCD devices is poor for both soft X-rays and high-energy X-rays.

To improve the overall QE, special types of CCDs have been developed. To improve the quantum efficiency for high-energetic X-rays, the active-layer thickness of the CCD has to be increased. This can be done by use of high-resistivity silicon ( $2 \text{ k}\Omega\text{cm}$  instead of  $20 \Omega\text{cm}$ ), which results in deep or even full depletion of the device ( $30 \mu\text{m}$  thick depletion layer instead of  $5 \mu\text{m}$ ) [7].

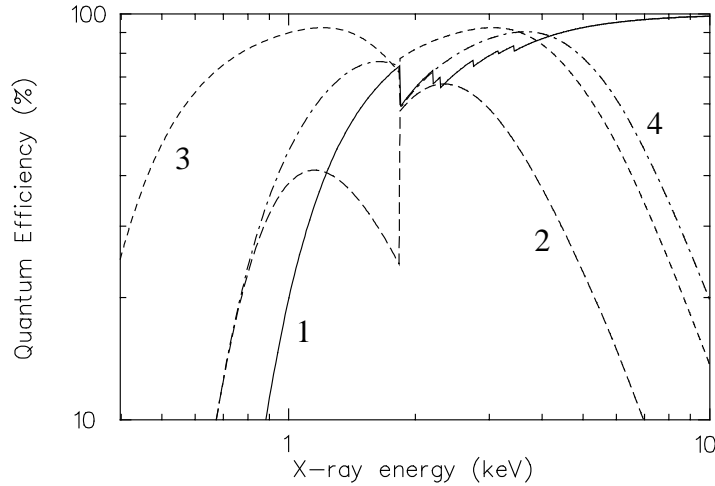


Fig. 2.5: Comparison of X-ray QE between a Si(Li) detector (1), a standard CCD (2), a back-illuminated CCD (3), and a deep-depletion CCD (4). The dip at 1.8 keV originates from the K-absorption-edge of silicon. See text for more details.

The quantum efficiency for soft X-rays may be improved either by thinning the electrode structure (thinned-electrode CCD), via for example removal of the overlying oxide layers, or by reduction of the electrode structure area (virtual-phase CCD), via reducing the number of electrodes and freeing part of the pixel from poly-silicon.

A different approach is the development of backside illuminated (BSI) devices. In this case, the backside of the CCD device is etched away until the remaining epitaxial silicon layer matches the expected depletion-layer depth. Subsequently, the new backside is implanted and annealed, which results in a dead layer of less than 100 nm. The X-rays then hit the CCD on its backside and do not have to cross the electrode structure, but only the thin dead layer. In this way, a practically windowless detector is obtained, which can have an enhanced QE for soft X-rays, especially if it is fully depleted and if the number of split events is kept low [7].

A comparison of (calculated) X-ray quantum-efficiency curves of a Si(Li) detector, a standard CCD, a deep-depletion CCD, and a back-illuminated CCD is shown in Fig. 2.5. From this figure, it can be seen that, compared to a Si(Li) detector, a CCD can give improved X-ray QE for low-energy X-rays. At high X-ray energies ( $> 10$  keV), however, the QE is worse, because of the limited CCD depletion-layer thickness. Through use of a deep-depletion CCD, with a depletion layer thickness of up to 30  $\mu\text{m}$ , instead of a standard CCD (about 5  $\mu\text{m}$ ), X-rays up to about 10 keV can still be detected efficiently. For enhanced X-ray detection, compared to a Si(Li) detector, at low X-ray energies, back-illuminated CCDs should be used. These offer a relatively large QE down to about 500 eV and detection of elements down to carbon may be feasible. Furthermore, the depletion layer thickness of about 20  $\mu\text{m}$  allows for the detection of X-rays up to  $\sim 10$  keV.

Since for a CCD only mild cooling down to 150-200 K is required, compared to  $\sim 100$  K for a Si(Li) detector, surface icing can be reduced and the quantum efficiency at low X-ray energies will be much less affected by ice layers on the detector surface.

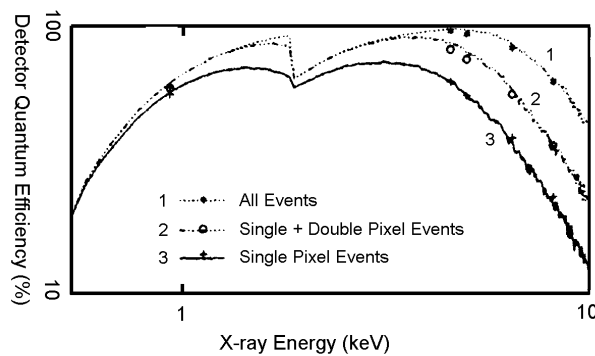


Fig. 2.6: Comparison of the effect of event selection criteria on the detector efficiency, in this case for a front-side illuminated CCD [20].

A last factor in the detection efficiency is formed by the event selection criteria [20]. These criteria are applied to improve energy resolution. However, throwing away events, such as split events, will decrease the detection efficiency for those X-ray energies that are likely to give split events. Depending on the device type, this may be either the low- or the high-energy X-rays. Fig. 2.6 depicts the QE of a front-side illuminated CCD, which shows that single-event selection significantly affects this efficiency. In this case this occurs especially for the high-energy X-rays, since only these create charge carriers in the field-free detector region that may diffuse radially and give split events.

In summary, if an ultra-thin-window deep-depletion back-illuminated CCD is used, a detection efficiency for soft X-rays (<1 keV) can be obtained that is enhanced compared to that of a conventional Si(Li) detector. Detection of elements down to carbon may be feasible, with reasonable efficiency. On the other hand, efficient X-ray detection with CCDs is limited up to about 10 keV, because of the limited depletion-layer thickness. Notice that the depth of this active region of a CCD is small compared to typical MeV charged-particle path-lengths in silicon. This is one of the reasons why a CCD is not suitable for charged-particle spectroscopy.

#### *Speed aspects*

For many applications, a high CCD operating speed is essential. For spectroscopy, this speed is limited by several factors: pixel readout frequency, count-rate limits, and frame readout frequency.

The first factor is the pixel readout frequency, which is determined by three parameters: parallel charge transfer, serial charge transfer, and charge detection at the output circuit.

The speed of parallel transfer is limited by the time-constant of the CCD gates, which is determined by the gate resistivity and capacitance, and which determines the minimum rise and fall time of the drive pulses. The maximum clocking frequency  $f_{p,max}$  for parallel charge transfer can be estimated using equation 2.2, as derived in [17]:

$$f_{p,max} \approx 1/W^2 \quad [\text{MHz}] \quad (2.2)$$

where  $W$  is the electrode width in centimeters perpendicular to the transfer direction. Typical values for  $W$  are a few mm, which limits the parallel clocking frequency to a few MHz.

The serial charge transfer speed is fundamentally limited by the drift speed of the charge carriers in silicon, but in practice by the speed of the clock-signal generation. The fundamental maximum clocking frequency  $f_{s,max}$  for serial charge transfer can be estimated using equation 2.3 as derived in [17]:

$$f_{s,max} \approx 5 \cdot 10^5 / L^3 \quad [\text{MHz}] \quad (2.3)$$

where  $L$  is the length of one CCD element along the serial transfer direction, in micrometers. Typical values for  $L$  are in the order of ten micrometers, which gives an upper limit for the serial clocking frequency of about 100 MHz.

The speed of charge detection at the output circuit is intrinsically limited by the time constant of the MOS source-follower transistor, which is determined by the gate-source capacitance. In a single-stage output circuit, with only one source-follower (see Fig. 2.3), the pixel readout frequency  $f_{\text{pixel,readout}}$  is limited to a few MHz [17]. The maximum pixel readout frequency can be increased by implementing a cascade of multiple source-follower stages, with increasing transistor size and gate-source capacitance. The pixel readout frequency can be increased up to 35 MHz for a two-stage output circuit and perhaps to 60 MHz for a three-stage output circuit [17]. The maximum pixel readout frequency can also be improved by using multiple parallel outputs. Fig. 2.7 shows some arrangements for implementing such outputs. Although these designs may increase frame readout rates a few times, the associated increased power dissipation and complexity of the electronics also has to be taken into account.

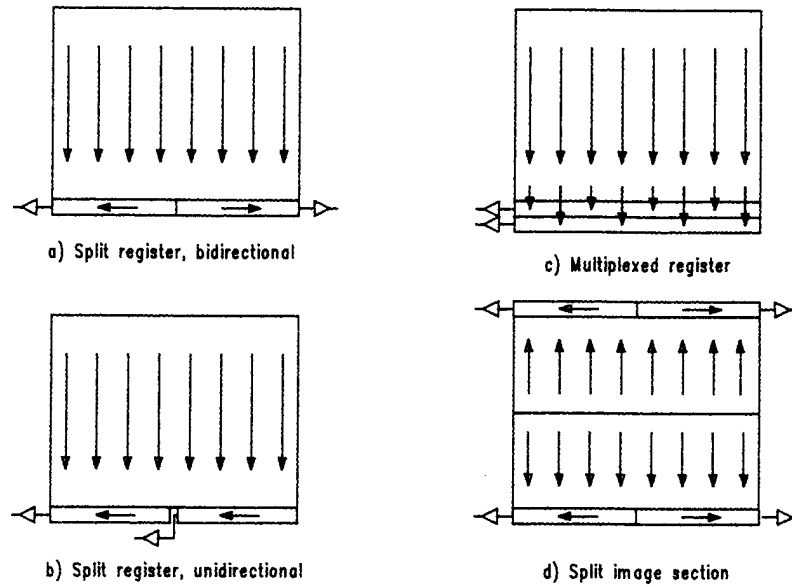


Fig. 2.7: CCD configurations with multiple parallel outputs [17].

A second essential factor that is relevant for the CCD operating speed is the count-rate limit  $f_{\text{count-rate,max}}$  of X-ray events. Ideally, at most one photon per pixel is detected during the integration and readout of one frame. In practice, to avoid event confusion, much less than one photon/pixel/frame should be detected. When a choice of 1% event confusion is made, Poisson statistics yields [21] a maximum of about 0.15 photons/pixel/frame, thus a filling level of 15%. Often, to ensure single-pixel events, an additional condition of all 8 surrounding pixels to be free of photons is imposed. This corresponds to a limit of 0.018

photons/pixel/frame and a filling level of  $n_{filling} = 2\%$ . The maximum count-rate  $f_{count-rate,max}$  is determined by the filling level  $n_{filling}$  and the pixel readout frequency  $f_{pixel,readout}$ . It is independent of the number of pixels or the size of the CCD array (see equation 2.4):

$$f_{count-rate,max} = n_{filling} \cdot f_{pixel,readout} \quad (2.4)$$

For example, for a given  $f_{pixel,readout} = 1$  MHz, a desired  $n_{filling} = 2\%$  limits  $f_{count-rate,max}$  to 20 kcps. A higher count-rate limit requires either more event confusion or a higher pixel readout frequency, which has a negative effect on the noise performance.

A third essential factor for the CCD operation speed is the frame readout frequency, which depends on the number of pixels in the frame, the pixel readout frequency, and the speed of parallel and serial transfer. Furthermore, the frame readout frequency can be improved by *binning*, i.e. combining the integrated charge of groups of neighboring pixels into one pixel before charge conversion. The frame readout frequency  $f_{frame,readout}$  for a standard CCD array can be calculated using equation 2.5:

$$f_{frame,readout} = \frac{bin_{ver}}{n_{ver} \left( bin_{ver} \cdot t_{ver} + \frac{n_{hor}}{bin_{hor}} (bin_{hor} \cdot t_{hor} + t_{sample}) \right)} \quad (2.5)$$

where  $n_{hor}$  and  $n_{ver}$  are the horizontal and vertical number of pixels of the CCD array, respectively. Furthermore,  $t_{hor}$  and  $t_{ver}$  are the horizontal (serial) and vertical (parallel) pixel-shift time, respectively.  $t_{sample}$  is the sampling time of the readout circuit, which is the reciprocal of  $f_{pixel,readout}$ . Finally,  $bin_{hor}$  and  $bin_{ver}$  are the horizontal and vertical binning factor (=number of neighbouring pixels that are combined), respectively.

For a typical 320×500 pixel CCD, with  $t_{hor} = 0.6$  μs,  $t_{ver} = 6$  μs, and  $t_{sample} = 10$  μs ( $f_{pixel,readout} = 100$  kHz), a frame readout speed of 0.59 frames/s without binning and 312 frames/s with full array binning is obtained.

Binning therefore increases the frame readout speed. However, the increase in frame readout speed does not compensate the loss in the effective number of pixels. In fact, either the filling level  $n_{filling}$  will increase or, in practice when the filling level has to be constant, the maximum overall count-rate  $f_{count-rate,max}$  will decrease, as can be seen in equation 2.6:

$$\frac{n_{filling}}{f_{count-rate,max}} = \frac{(bin_{hor} \cdot bin_{ver} \cdot t_{ver} + bin_{hor} \cdot n_{hor} \cdot t_{hor} + t_{sample} \cdot n_{hor})}{n_{hor}} \quad (2.6)$$

A few examples using equation 2.6 are given in table 2.1. Clearly, using vertical binning a compromise between a high frame-rate and a high maximum count-rate may be obtained.

*Table 2.1: The effects of binning on frame-rate and maximum count-rate.*



Binning (horizontal $\times$ vertical)	$f_{\text{frame, readout}}$ (frames/s)	$f_{\text{count-rate, max}}$ (counts/s) when $n_{\text{filling}} = 2\%$
None	0.59	1883
2 $\times$ 2	2.22	1774
3 $\times$ 3	4.7	1671
5 $\times$ 5	11.6	1485
10 $\times$ 10	36	1119
30 $\times$ 30	125	446
320 $\times$ 500	312	6
320 $\times$ 1	9.6	96
1 $\times$ 500	156	1001

Although binning can increase the frame readout frequency, pixel resolution is sacrificed and this will reduce the maximum count-rate. There are several more disadvantages to the binning of CCD X-ray data.

- In addition to the binning of integrated charge from ionizing radiation, also the charge from integrated dark current is binned. This will cause the charge-storage wells to overflow more quickly. During cooling, however, this effect will be negligible.
- Through binning it becomes difficult, if not impossible, to correct for CTI using pixel-dependent correction functions.
- At a high degree of binning, split-event reconstruction becomes impossible. Single-event histograms, required for high-resolution X-ray spectroscopy, can no longer be generated.
- Incoming parasitic charged-particles cause the content of the binned area, in which they occur, to be useless for X-ray spectroscopy. The larger the pixel area that is binned, the larger the area that may become useless. Thus, X-ray detection efficiency may be reduced by binning, in case of a large number of charged particles. Furthermore, charged-particle discrimination will become more difficult.
- Defect pixels will affect the whole area that is binned around these pixels. One defect pixel in a binned area will make this area useless.

In summary, typical single-stage CCD arrays can support pixel readout frequencies up to several MHz. This speed can be increased to tens of MHz by integrating multiple cascaded output-stages or multiple parallel output circuits on the chip. More important for scanning microprobe X-ray spectroscopy, however, is the frame readout rate of the CCD array, which depends, in addition to the pixel readout frequency, on the total number of pixels and on the degree of binning.

Binning can improve the frame rate, but for X-ray spectroscopy it has the disadvantage of, amongst others, reducing the maximum count-rate. Without binning, for a typical single-stage

320×500 pixel CCD array, frame rates of less than 1 frame/s @ 100 kHz sampling up to 10 frames/s @ 10 MHz sampling may be reached. To ensure low-noise performance, however, the sampling rate should not exceed 100 kHz. It therefore can be concluded that the frame readout speed is limited to a few frames/s and that in X-ray spectroscopy a CCD can be used for slow-scan applications only.

#### *Radiation damage effects*

Much research has been done on the effects of (parasitic) radiation on the operation of CCDs, especially for use in astronomical applications in space. Likewise, when a CCD is used as an X-ray detector or charged-particle detector in ion-beam experiments, the effect of radiation damage is very important. Generally, three effects will occur in CCDs with radiation damage [22]:

- Change in MOS flat-band voltage (voltage needed for depletion to occur) through positive charge build-up (trapped holes) in the insulating (oxide) layer, resulting from ionizing radiation. This effect can be compensated by adjusting the DC-bias voltages.
- Increase in dark current, largely through an increased density of generation-recombination centres at the silicon/oxide interface, and also through an increased density of damage. Cooling can be used to reduce the dark current.
- Increase of CTI, through bulk damage (displacement effects and increased charge trapping). This will result in a degraded energy resolution.

From many studies it appears that MeV protons form the most damaging type of radiation, compared to neutrons, electrons, and gammas, since they cause the largest amount of displacement. Of course, radiation damage will occur gradually. Serious degradation occurs at doses of  $10^8$ - $10^9$  protons/cm<sup>2</sup>. For a 1 cm<sup>2</sup> CCD irradiated with protons at 1 kcps, this limits its lifetime to roughly one week. In X-ray spectroscopy, the amount of parasitic charged particles must therefore be reduced. Notice that a CCD is not suitable for charged-particle spectroscopy, particularly of MeV ions.

### 2.3.3 Conclusions

In conclusion, a CCD has a great potential to become an excellent X-ray detector, but only in slow-scan applications with frame readout rates of a few frames/s. For use as X-ray detector in the Eindhoven scanning ion microprobe, it is found that a CCD is not applicable. Since measurement times of the microprobe are typically 1 ms per sample position, the frame readout rate of the CCD should be larger than 1000 frames/s, to avoid X-ray event confusion between sample positions. This conflicts with the limited frame readout frequency of at most a few frames/s, as required for X-ray spectroscopy.

## 2.4 Charged-particle spectroscopy with a PSD

### 2.4.1 PSD operating principle

The continuous-resistive charge-dividing position-sensitive detector (PSD in short) is a  $pn$ -junction detector that provides both an energy measurement and a measurement of the position of incidence of incoming ionizing radiation. It can be made position sensitive in either one dimension (1-D) or two dimensions (2-D). The PSD is rectangular, and Fig. 2.8 shows the schematic layout of the 1-D PSD.

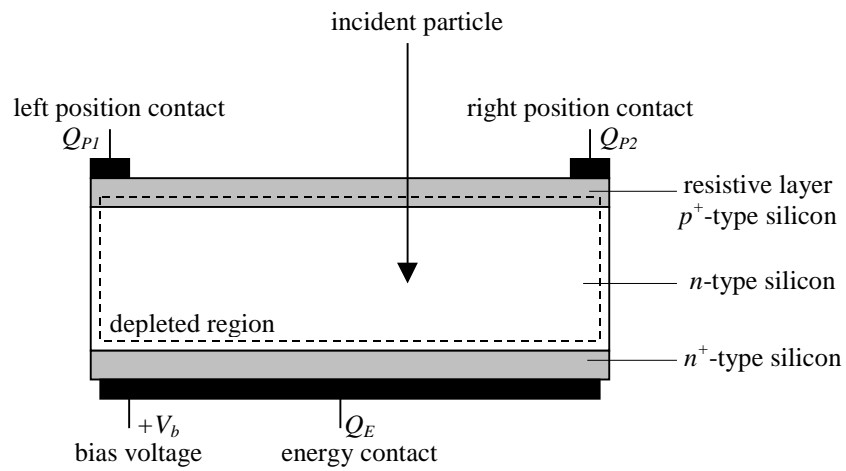


Fig. 2.8: Schematic layout of the 1-D PSD. The typical width is 10-50 mm. The typical thickness is 300  $\mu\text{m}$ . See text for details.

An  $n$ -type Si wafer has a front-side boron-implanted  $p^+$ -type resistive layer, forming a  $pn$ -junction diode. Incoming ionizing radiation creates electron/hole-pairs within the sensitive region of the detector, which has been depleted from free charge carriers by applying an external reverse bias voltage  $V_b$  across the detector. The electrons and holes will be swept to the electrodes by the electric field. The energy signal is obtained from the total charge  $Q_E$  that is collected at the backside  $n^+$ -type electrode, whereas the position signals are obtained from the charge fractions  $Q_{P1}$  and  $Q_{P2}$ . These are collected at the outer edges of the front-side resistive strip. The position of incidence is determined from the charge fractions  $Q_{P1}$  and  $Q_{P2}$  (amplitude method) or via pulse-shape analysis of the charge pulses (time method). Generally, the amplitude method is used.

A 2-D PSD can be made by replacing the backside electrode with a second resistive layer and two more position contacts, which are aligned perpendicular to the front-side position contacts. The energy signal is then obtained from the summed front- or backside signals. A second way to obtain a 2-D PSD is by equipping the detector with four contacts at the corners of the front-side electrode. The energy signal is then obtained from the backside electrode.

In this dissertation we will focus on a commercially available 1-D PSD, a nuclear version of the SiTek [12] type 1L30. For this nuclear version, contrary to the standard version, the  $\text{SiO}_2$  anti-reflective coating has not been added, to obtain a dead layer of less than 100 nm. The detector has an active area of  $30 \times 5 \text{ mm}^2$ , and an  $n$ -type high-resistivity silicon wafer thickness of  $280 \text{ }\mu\text{m}$  with a front-side boron-implanted resistive layer. Measurements show that at full depletion (80 V reverse bias), the resistive-layer resistance  $R_d$  equals  $60 \text{ k}\Omega$  and the junction capacitance  $C_d$  equals  $60 \text{ pF}$ .

#### 2.4.2 Theory of PSD operation

The 1-D PSD can be modeled as an  $RC$ -line with a homogeneously distributed capacitance  $C_d$  and resistance  $R_d$  along the detector [23]. This is shown in Fig. 2.9, where  $\sum \partial R = R_d$  and  $\sum \partial C = C_d$ . The resistive  $p^+$ -layer corresponds to  $R_d$  and the junction capacitance to  $C_d$ . The complete process of charge collection is equivalent to instant charging of a capacitance  $\partial C$  at the position of incidence with a charge  $Q$  and, next, the collection of this charge via the resistances  $\partial R$  at the position contacts  $Q_{P1}$  and  $Q_{P2}$ . At the energy contact, collection of a charge  $Q_E = -Q$  takes place, since no charge is created within the detector volume. The  $RC$ -line has a time constant defined as  $\tau_d = R_d C_d / \pi^2$ .

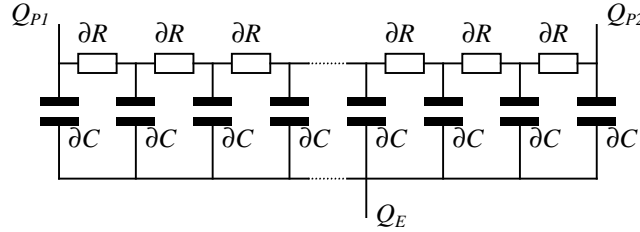


Fig. 2.9: The PSD electrical equivalent with the homogeneously distributed resistance  $\sum \partial R = R_d$  and capacitance  $\sum \partial C = C_d$ .

Three assumptions have to be made, in order to be able to obtain an analytical expression for the distribution of the collected charge at the three contacts [23]:

- 1) Charge injection is confined to a single point. In practice, the lateral extent of charge injection (micrometer range) may be neglected compared to the length of the resistive layer (centimeter range) and hence this assumption is satisfied.
- 2) The capacitance is instantly charged. In practice, charge collection in the depletion zone (nanosecond range) is much faster than charge collection across the resistive layer (microsecond range).
- 3) Both position contacts are grounded. In practice, the pre-amplifiers connected to the contacts must have an input impedance that is much smaller than the output impedance of the detector junction (see also section 2.4.3).

The physical process of charge collection at the contacts is described by the diffusion-like differential equation 2.7 [23]:

$$\frac{\partial U}{\partial t} = \frac{L^2}{R_d C_d} \cdot \frac{\partial^2 U}{\partial x^2} \quad (2.7)$$

where  $U(x_i, x, t)$  is the voltage in the resistive  $p^+$ -layer as a function of position  $x$ , position of incidence  $x_i$ , and time  $t$ . Furthermore,  $L$  is the length of the resistive layer.

The  $\delta$ -pulse injection of charge  $Q_0$  at  $x = x_i$  at  $t = 0$  is described by the initial condition  $U(x=x_i, t=0) = \infty$ . The virtually grounded position contacts are described by the boundary conditions  $U(x=0, t \geq 0) = 0$  and  $U(x=L, t \geq 0) = 0$ .

The solution of the differential equation is given in equation 2.8:

$$U(x_i, x, t) = \left( \frac{2Q_0}{C_d} \right) \cdot \sum_{n=1}^{\infty} \sin\left(\frac{n\pi x_i}{L}\right) \cdot \sin\left(\frac{n\pi x}{L}\right) \cdot \exp\left(-\frac{n^2 \pi^2 t}{R_d C_d}\right) \quad (2.8)$$

In Fig. 2.10 the voltage distribution  $U(x_i, x, t)$  across the resistive layer as a function of position  $x$  and time  $t$  is plotted for a  $\delta$ -pulse charge injection at  $t=0$  and  $x_i=0.3L$ .

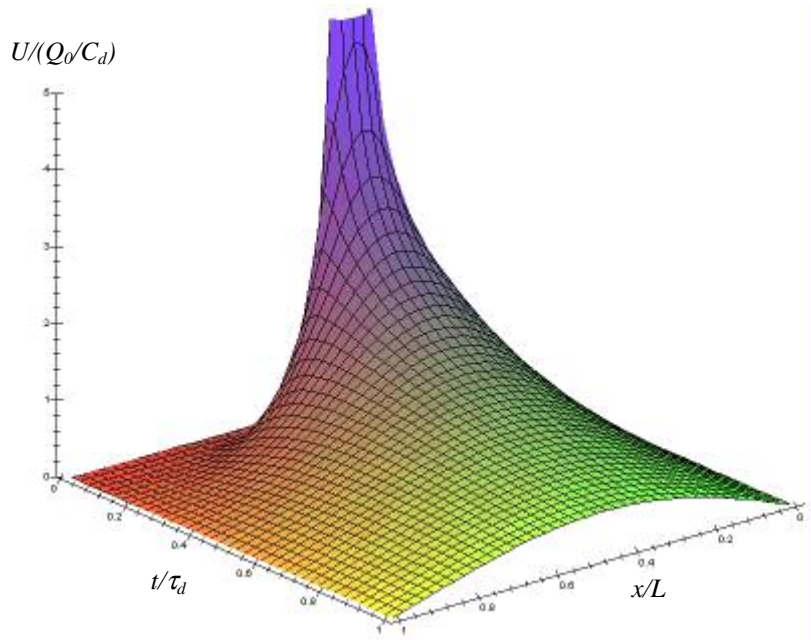


Fig. 2.10: Voltage distribution  $U(x_i, x, t)$  across the resistive layer as a function of position  $x$  and time  $t$  for a  $\delta$ -pulse charge-injection at  $t=0$  and  $x_i=0.3L$ .

The charges  $Q_{P1}$  and  $Q_{P2}$  collected at the position contacts are derived from equation 2.9.

$$Q_{P1,P2} = \frac{L}{R_d} \int_0^t \frac{\partial U(x_i, x, t')}{\partial x} \Big|_{x=0,L} dt', \quad (2.9)$$

The charge  $Q_E$  collected at the energy contact is the negative sum of the charges collected at the position contacts:  $Q_E = - (Q_{P1} + Q_{P2})$ . This results in the expressions given in the equations 2.9a-c:

$$Q_{P1}(x_i, t) = \frac{2Q_0}{\pi} \sum_{n=1}^{\infty} \frac{1}{n} \cdot \sin\left(\frac{n\pi x_i}{L}\right) \cdot \left(1 - \exp\left(\frac{-n^2 \pi^2 t}{R_d C_d}\right)\right) \quad (2.9a)$$

$$Q_{P2}(x_i, t) = -\frac{2Q_0}{\pi} \sum_{n=1}^{\infty} \frac{1}{n} \cdot \sin\left(\frac{n\pi x_i}{L}\right) \cdot \cos(n\pi) \cdot \left(1 - \exp\left(\frac{-n^2 \pi^2 t}{R_d C_d}\right)\right) \quad (2.9b)$$

$$Q_E(x_i, t) = -\frac{2Q_0}{\pi} \sum_{n=1}^{\infty} \frac{1}{n} \cdot \sin\left(\frac{n\pi x_i}{L}\right) \cdot (1 - \cos(n\pi)) \cdot \left(1 - \exp\left(\frac{-n^2 \pi^2 t}{R_d C_d}\right)\right) \quad (2.9c)$$

In the limit of  $t \rightarrow \infty$  these equations simplify to equations 2.10a-c:

$$Q_{P1}(x_i) = \left(1 - \frac{x_i}{L}\right) Q_0 \quad (2.10a)$$

$$Q_{P2}(x_i) = \frac{x_i}{L} Q_0 \quad (2.10b)$$

$$Q_E(x_i) = -Q_0 \quad (2.10c)$$

From this equation it can be seen that for large charge-collection times, the PSD acts like a linear charge divider between the position contacts. Furthermore, the charge collected at the energy contact is independent of the position of incidence, as expected. A visual representation of the charge collected as a function of position of incidence  $x_i$  and time  $t$  is shown in Fig. 2.11, for both the position contact at  $x=0$  and the energy contact.

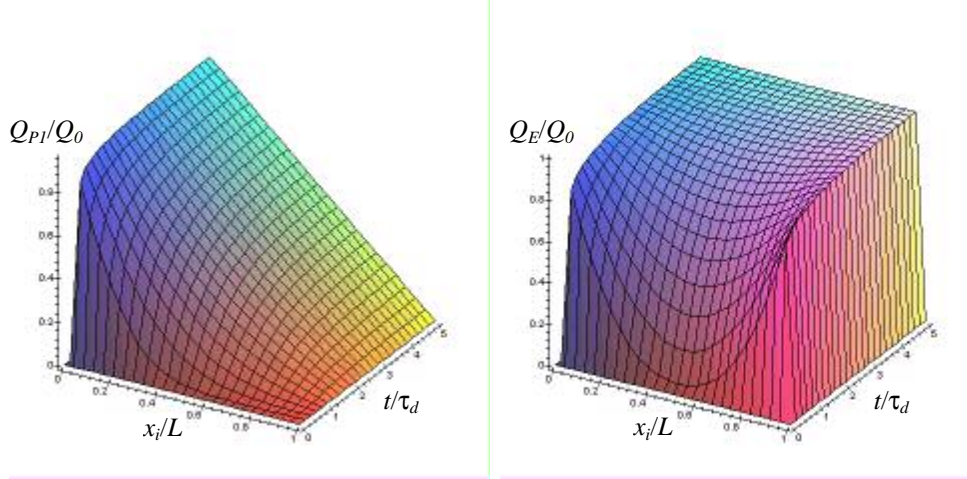


Fig. 2.11: Charge collection at the position contact at  $x=0$  (left-hand side) and the energy contact (right-hand side) as a function of position of incidence  $x_i$  and time  $t$ . For large collection times, a linear dependence is observed.

In practice, however, infinite (in time) charge collection will not take place. The collected charge at each of the three contacts is supplied to a charge-sensitive pre-amplifier and a shaping amplifier, successively. The purpose of the first is to perform charge-to-voltage conversion, and the purpose of the latter is to perform pulse-shaping and filtering to improve the signal-to-noise ratio. The pre-amplifier is described in more detail in section 2.4.3. Neglecting their  $RC$  (integrating) effect, the pre-amplifiers convert the charge pulse, which in the ideal case of instant charge collection is a step function, into a step voltage pulse. The shaping amplifier, that consists of a differentiator ( $CR$ ) and an integrator ( $RC$ ) with equal shaping times  $\tau_{sh}=R_{sh}C_{sh}$ , converts this step pulse into a shaped pulse. Ideally, the pulse-height of this pulse is proportional to the amount of charge from the detector output.

In case of the PSD, however, charge is not collected instantly, but is collected more slowly due to the resistive charge-dividing layer. The rise-time of the charge-pulses is therefore finite and depends on the position of incidence. The amplitude after shaping will be lower than that of shaped step-pulses carrying the same amount of charge. The difference is called the *ballistic deficit*. From Fig. 2.11 it can be seen that the ballistic deficit in both the position and the energy signals reaches a maximum for  $x_i=L/2$ .

The presence of a ballistic deficit results in a non-linearity in both the position and the energy signals of the PSD. From a practical point of view, the PSD characteristics are defined to be linear if the ballistic deficit of the energy measurement at  $x_i=L/2$  is smaller than 1% of the energy pulse-height measured at  $x_i=0$  and  $x_i=L$ . Theoretically (equation 2.9) it can be shown that this is the case for a charge-collection time  $t > 4.915 \cdot \tau_d$ . It can also be shown [24] that this corresponds to  $\tau_{sh} > 5.26 \cdot \tau_d$ .

### 2.4.3 Pre-amplifier requirements, theory, and design

The small charge pulses of typically  $10^6$  electrons that are generated by incoming charged particles in the PSD are to be converted into voltage pulses (in the mV range) by charge-sensitive pre-amplifiers. These pre-amplifiers have to satisfy several requirements:

- 1) A step-response output to allow for linear pulse amplification. This requires the output-pulse rise-time to be as short as possible and comparable to the charge collection time in the PSD (typically  $10^{-7}$  s). The output-pulse decay-time, on the other hand, has to be large in order to enable full charge collection [9].
- 2) A virtually grounded input to ensure full charge collection from the PSD. In practice, this is achieved by a low input impedance of the pre-amplifier compared to the output impedance of the detector in the frequency range of interest (roughly 10 kHz - 10 MHz).
- 3) Low-noise performance. This is required for good energy and position resolution. One of the ways to improve noise-performance is to reduce the input capacitance  $C_{in}$ , which is formed by the detector capacitance, the input capacitance of the operational amplifier (opamp) in the pre-amplifier, and the capacitance of the cables between the detector and the pre-amplifier.

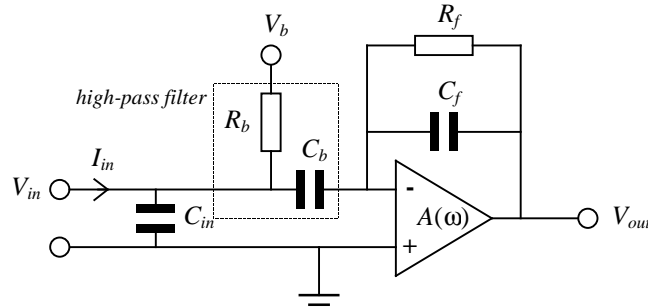


Fig. 2.12: The charge-sensitive pre-amplifier with the operational amplifier  $A(\omega)$ , feedback loop ( $C_f$  and  $R_f$ ), and the high-pass filter ( $C_b$  and  $R_b$ ) that isolates the bias-voltage  $V_b$  from the PSD signal  $V_{in}$  via AC-coupling.

The schematic layout of a charge-sensitive pre-amplifier is shown in Fig. 2.12. The charge pulse from the detector is represented by the input current  $I_{in}$ . Normally, this current would charge the input capacitance  $C_{in}$ . In the charge-sensitive pre-amplifier configuration, however, a feedback loop to the inverting input is present containing a capacitance  $C_f$ . The condition for correct charge-sensitive pre-amplifier operation is that the open-loop gain of the pre-amplifier is made much larger than  $(C_{in}+C_f)/C_f$ . In that case, the input voltage  $V_{in}$  is kept very small and the detector output is virtually grounded. Instead of charging the input capacitance  $C_{in}$ , now the feedback capacitance  $C_f$  is charged by  $I_{in}$ . The output voltage  $V_{out}$  of the pre-amplifier is proportional to the collected charge  $Q_0$  ( $V_{out}=Q_0/C_f$ ) and independent of the input capacitance  $C_{in}$  [9].



After several charge pulses,  $C_f$  may become saturated, prohibiting the pre-amplifier to respond to incoming charge pulses. To prevent this, a feedback resistance  $R_f$  has been added parallel to  $C_f$ , in order to discharge the latter. The feedback time-constant  $\tau_f = C_f R_f$ , which determines the decay-time of the output pulse, has to be large compared to the PSD charge collection time (typically  $10^{-7}$  s) and the shaping time-constant  $\tau_{sh}$  (typically  $10^{-6}$  s).

The pre-amplifier also provides a means to apply a bias voltage to the detector to which it is connected. The reverse bias voltage  $V_b$  is applied via an AC-coupling filter, formed by the bias resistance  $R_b$  and coupling capacitance  $C_b$ , which act as a high-pass filter towards the pre-amplifier input and thus isolate this input from the bias voltage.

It can be shown [25] that the charge-sensitive pre-amplifier with an input current at the inverting input of the operational amplifier has an equivalent circuit in which the feedback impedance  $Z_f = 1/(j\omega C_f + 1/R_f)$  has been replaced by an equivalent input impedance  $Z_{in}$  as given in equation 2.11. In this equation,  $A(\omega) = A_0/(1+j\omega\tau_0)$  is the open loop gain of the operational amplifier, with  $A_0$  the dc-gain and  $\tau_0$  the corresponding time constant.

$$Z_{in} = \frac{Z_f}{A(\omega)+1} = \frac{R_f}{1 + j\omega R_f C_f} \cdot \frac{1}{\frac{A_0}{1 + j\omega\tau_0} + 1} \quad (2.11)$$

The behavior of  $|Z_{in}|$  depends on the frequency  $\omega$  and four regions can be distinguished (it is assumed that  $\tau_0 \gg \tau_f$ ):

- |                                     |                                       |  |
|-------------------------------------|---------------------------------------|--|
| 1) $\omega < 1/\tau_0$              | : The impedance is resistive:         | $Z_{in} \approx R_f/A_0$ .               |
| 2) $1/\tau_0 < \omega < 1/\tau_f$   | : The impedance is inductive:         | $Z_{in} \approx j\omega\tau_0 R_f/A_0$ . |
| 3) $1/\tau_f < \omega < A_0/\tau_0$ | : The impedance is <b>resistive</b> : | $Z_{in} \approx \tau_0/A_0 C_f$ .        |
| 4) $\omega > A_0/\tau_0$            | : The impedance is capacitive:        | $Z_{in} \approx 1/j\omega C_f$ .         |

The ratio  $A_0/\tau_0$  is often called the gain-bandwidth product.

In Fig. 2.13 the absolute pre-amplifier input impedance  $|Z_{in}|$ , obtained from equation 2.11, is plotted as a function of frequency  $\omega$ , using values of  $A_0 = 10^6$ ,  $\tau_0 = 12.5$  ms,  $C_f = 15$  pF,  $R_f = 10$  M $\Omega$ , and hence  $\tau_f = 150$   $\mu$ s (these values are taken from the designed pre-amplifier, for which the gain-bandwidth product equals 80 MHz, see below).

In the frequency range of interest (15 kHz – 15 MHz),  $Z_{in}$  is resistive. To preserve a fast and complete charge-flow out of the PSD and full charge collection on the feedback capacitance, the input impedance and hence the resistance of the pre-amplifier should be kept as low as possible.

One of the ways to do this is to maximize the feedback capacitor, since  $Z_{in} \approx \tau_0/A_0 C_f$ . This reduces, however, the output voltage  $V_{out} = Q_0/C_f$  and increases the feedback time-constant  $\tau_f = C_f R_f$ .

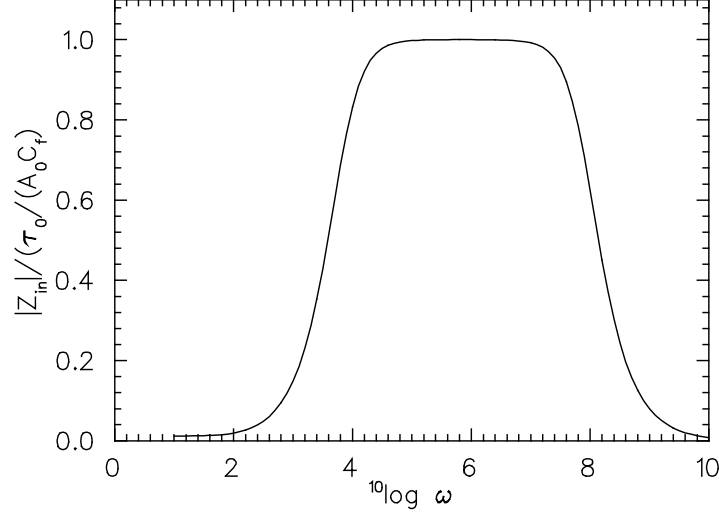


Fig. 2.13: The calculated absolute pre-amplifier input impedance  $|Z_{in}|$  as a function of frequency  $\omega$ . See text for details.

Since it is difficult to determine for commercially available pre-amplifiers whether they satisfy the requirements mentioned above, charge-sensitive pre-amplifiers were designed and built ourselves. An OPA637 [26] operational amplifier was used, together with a feedback capacitance  $C_f$  of 15 pF and a feedback resistor  $R_f$  of 10 M $\Omega$ . The OPA637 has an open-loop voltage gain of 120 dB ( $A_0 = 10^6$ ) and a gain-bandwidth product of 80 MHz. From this, it is calculated that  $\tau_0 = 12.5$  ms and that the input impedance in the frequency range of interest is about 800  $\Omega$ . This pre-amplifier input impedance of 800  $\Omega$  is very small compared to the PSD resistive-layer resistance of about 60 k $\Omega$ . This satisfies the requirement that the PSD position contacts should be virtually grounded. Furthermore, the feedback time-constant  $\tau_f$  is 150  $\mu$ s, which gives a relatively long pulse-decay time compared to typical charge-collection times and pulse-shaping times.

A second factor in the pre-amplifier design concerns the choice of the bias resistance  $R_b$  and the bias capacitance  $C_b$ . In general, a very large value for  $R_b$  is preferred, to reduce its thermal noise contribution. The two coupling capacitances  $C_b$  of both pre-amplifiers connected to the PSD position contacts are connected to each other via the resistive layer of the PSD. After a charge pulse, the charge on both capacitances  $C_b$  will be balanced by a current through this resistive layer. This should not affect the charge collected on the feedback capacitance  $C_f$  and thus the position signals. Therefore, the characteristic time constant  $C_b R_d$  (with  $R_d$  the PSD resistive-layer resistance) has to be much larger than the charge collection times and shaping times. A bias capacitance of  $C_b = 10$  nF was chosen, which results in a time constant  $C_b R_d$  of about 0.5 ms.

#### 2.4.4 Noise theory and optimum shaping time

In this section, noise calculations for our system consisting of the PSD and amplifiers are described. Three types of noise can occur: thermal noise, shot noise, and flicker noise.

*Thermal noise* (or Johnson noise) arises in resistors due to the Brownian motion of electrons, even in the absence of current. Since this motion is random, no average voltage  $v$  is expected. A mean-square voltage  $v^2$ , however, is present. The square spectral voltage density  $S_v$ , i.e. the mean square voltage  $d(v^2)$  in a frequency interval  $df$ , for thermal noise in a resistance  $R$  is given by equation 2.12 (with Boltzmann's constant  $k$  and absolute temperature  $T$ ):

$$S_v = \frac{d(v^2)}{df} = 4kTR \quad [\text{V}^2\text{Hz}^{-1}] \quad (2.12)$$

The thermal noise can also be expressed in a corresponding square spectral current density  $S_i$  (equation 2.13):

$$S_i = \frac{d(i^2)}{df} = \frac{4kT}{R} \quad [\text{A}^2\text{Hz}^{-1}] \quad (2.13)$$

For analytical purposes, thermal noise is assumed to have a uniform ('white') frequency distribution. The resistor  $R$  can be replaced by an ideal resistor  $R_{ideal}$  either in series with a voltage noise source  $v_{noise}$  or in parallel with a current noise source  $i_{noise}$ .

*Shot noise* originates from the statistical fluctuations in the number of charge carriers in a current. It occurs in every device that carries a current. Its square spectral current density for a current  $I$  is given by equation 2.14 (with  $e$  the electron charge):

$$S_i = 2eI \quad [\text{A}^2\text{Hz}^{-1}] \quad (2.14)$$

Shot noise also has a white noise frequency distribution, and can be represented by a current noise source.

*Flicker noise* or  $1/f$  noise arises in a wide variety of devices, but no single mechanism can explain its presence. Instead of a uniform 'white' frequency distribution, it has a spectral density inversely proportional to the frequency ('pink' noise distribution). It is therefore dominant for low-frequency signals. For high-frequency signals, like in this work, it may be neglected compared to other noise sources.

For a total noise calculation, it is necessary to know the PSD impedance as seen from the pre-amplifier input. From transmission-line theory [27] it follows that, the continuously distributed  $RC$ -line, like the PSD, is equivalent to a transmission line without inductivity. Its complex impedance is given by  $Z_p = Z_0 \tanh(\gamma L)$  for the position signal, and  $Z_E = \frac{1}{2} Z_0 \coth(\gamma L)$  for the energy signal, where  $Z_0 = \sqrt{R_d / j\omega C_d}$  is the characteristic impedance of the transmission line and  $\gamma L = \sqrt{j\omega R_d C_d}$ , with  $\gamma$  the propagation coefficient of the line in  $\text{m}^{-1}$  and  $L$  the length of the line in m. Using a Taylor approximation, these expressions may be simplified [25] as follows:

$$Z_p = \sqrt{\frac{R_d}{j\omega C_d}} \tanh(\sqrt{j\omega R_d C_d}) \cong \left( \frac{1}{R_d} + j\omega \frac{C_d}{3} \right)^{-1} \quad (2.15)$$

$$Z_E = \frac{1}{2} \sqrt{\frac{R_d}{j\omega C_d}} \coth(\sqrt{j\omega R_d C_d}) \cong \frac{R_d}{12} + \frac{1}{j\omega C_d} \quad (2.16)$$

For the position signal,  $Z_p$  corresponds to a parallel connection of the PSD resistance  $R_d$  and one third of the PSD capacitance  $C_d$ . For the energy signal,  $Z_E$  corresponds to a series connection of  $C_d$  and one twelfth of  $R_d$ . These approximations are valid for frequencies  $\omega$  up to several MHz.

Noise contributions to the position and energy signals results from both current noise sources and voltage noise sources. *Current noise* sources include: thermal noise from the detector resistance  $R_d$  (position signal), from the virtual detector resistance  $R_d/12$  (energy signal), from the feedback resistance  $R_f$ , and from the bias resistance  $R_b$ . Further current noise sources are: shot noise from the leakage current  $I_l$  (about 20 nA @ 80 V bias) and from the operational amplifier at the inverting input. All these current noise sources are combined into a total current noise source with square spectral current density  $S_{i,in}$ . Using the pre-amplifier input impedance in the frequency range of interest,  $Z_{in} \approx \tau_0 / A_0 C_f$ , and the operational amplifier open-loop gain  $A(\omega)$ , the square spectral voltage density  $S_{v,out}$  at the pre-amplifier output can be calculated:  $S_{v,out} = |A(\omega)|^2 \cdot |Z_{in}|^2 \cdot S_{i,in}$ . This results in the following expressions:

$$S_{v,out,currentnoise,p} = \left( \frac{A_0}{\omega \tau_0} \right)^2 \left( \frac{\tau_0}{A_0 C_f} \right)^2 \left( \frac{4kT}{R_d} + \frac{4kT}{R_b} + \frac{4kT}{R_f} + 2eI_l \right) \quad (2.17)$$

$$S_{v,out,currentnoise,E} = \left( \frac{A_0}{\omega \tau_0} \right)^2 \left( \frac{\tau_0}{A_0 C_f} \right)^2 \left( 4kT \frac{12}{R_d} + \frac{4kT}{R_b} + \frac{4kT}{R_f} + 2eI_l \right) \quad (2.18)$$

A *voltage noise* source is formed by the internal noise of the operational amplifier. This is represented by a voltage noise source with square spectral voltage density  $S_{v,in}$  at the non-inverting input of the operational amplifier. Using the transfer function  $H(\omega)$  for a signal on the non-inverting input of the operational amplifier [25], which depends on the detector impedance ( $Z_p$  or  $Z_E$ ) and the feedback impedance ( $Z_f \approx 1/j\omega C_f$ ), the square spectral voltage density  $S_{v,out}$  in the frequency range of interest, can be calculated:  $S_{v,out} = |H(\omega)|^2 \cdot S_{v,in}$ . This results in the following expressions:

$$S_{v,out,voltage\ noise,p} = \left| \frac{C_f + \frac{C_d}{3}}{C_f} + \frac{1}{j\omega R_d C_f} \right|^2 \cdot S_{v,in} \quad (2.19)$$

$$S_{v,out,voltage\ noise,E} = \left| \frac{C_f + C_d}{C_f} \cdot \frac{1 + j\omega \left( \frac{R_d}{12} \frac{C_d \cdot C_f}{C_f + C_d} \right)}{1 + j\omega \frac{R_d}{12} C_d} \right|^2 \cdot S_{v,in} \quad (2.20)$$

The square spectral voltage densities of both current and voltage noise sources may be added. The output signal of the pre-amplifier is shaped by a shaping main amplifier. Generally, one *CR*-filter (differentiator) and one *RC*-filter (integrator) with equal shaping time-constants  $\tau_{sh}$  are used. Using the transfer function  $H_{sh}(\omega) = j\omega\tau_{sh}/(1 + j\omega\tau_{sh})^2$  of the shaping amplifier, the total square voltage noise  $v_{out}^2$  after filtering by the shaping amplifiers can be derived:

$$v_{out}^2 = \int_0^\infty \left( S_{v,out,current\ noise} + S_{v,out,voltage\ noise} \right) \cdot \left| \frac{j\omega\tau_{sh}}{(1 + j\omega\tau_{sh})^2} \right|^2 d\omega \quad (2.21)$$

Solving the integral, for both the position and the energy contacts, yields:

$$v_{out,p}^2 = \frac{\pi}{4C_f^2} \left[ \left( \frac{4kT}{R_d} + \frac{4kT}{R_b} + \frac{4kT}{R_f} + 2I_l e \right) \tau_{sh} + S_{v,in} \left( \frac{\tau_{sh}}{R_d^2} + \frac{(C_d/3 + C_f)^2}{\tau_{sh}} \right) \right] \quad (2.22)$$

$$v_{out,E}^2 = \frac{\pi}{4C_f^2} \left[ \left( \frac{4kT}{R_d/12} + \frac{4kT}{R_b} + \frac{4kT}{R_f} + 2I_l e \right) \tau_{sh} + S_{v,in} \left( \frac{C_d^2 + 2C_d C_f}{(\tau_{sh} + C_d R_d/12)^2} \tau_{sh} + \frac{C_f^2}{\tau_{sh}} \right) \right] \quad (2.23)$$

From these expressions, it can be seen that there exists an optimal shaping time  $\tau_{sh}$  for which the noise  $v_{out}^2$  is minimal. For practical values of  $\tau_{sh}$ , current noise contributes to  $v_{out}^2$  proportional to  $\tau_{sh}$ , whereas voltage noise contributes inversely proportional to  $\tau_{sh}$ . The optimal shaping time may differ between the position and the energy signals and depends on the parameters of the PSD and the pre-amplifier. At  $T=300$  K and  $V_b=80$  V these are  $C_f=15$  pF,  $R_f=10$  M $\Omega$ ,  $R_d=60$  k $\Omega$ ,  $C_d=60$  pF,  $R_b=10$  M $\Omega$ ,  $I_f=20$  nA, and  $S_{v,in}=20 \cdot 10^{-18}$  V<sup>2</sup>/Hz [26].

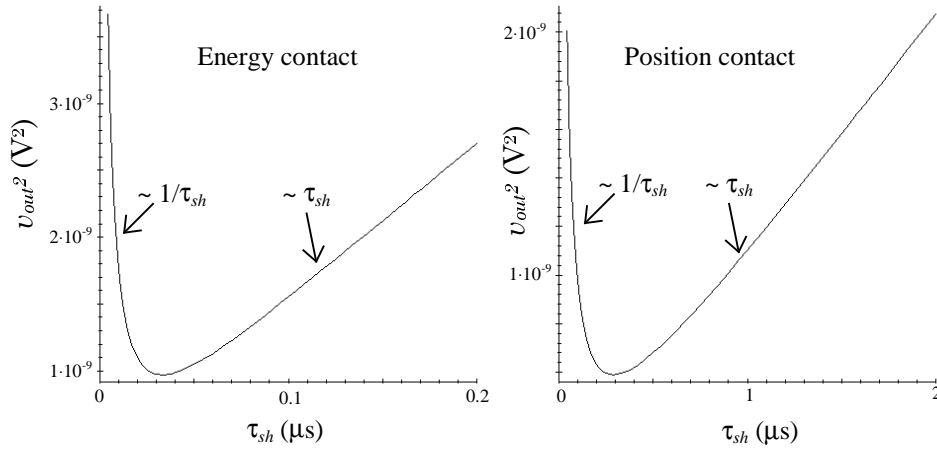


Fig. 2.14: Total square voltage noise  $v_{out}^2$  as a function of shaping time  $\tau_{sh}$  for the energy contact (left) and the position contacts (right).

For the position signals, the optimum shaping time  $\tau_{sh} = 0.3$   $\mu$ s, with a corresponding total voltage noise  $|v_{out}| = 24$   $\mu$ V rms. For the energy signals,  $|v_{out}| = 31$   $\mu$ V rms for  $\tau_{sh} = 0.03$   $\mu$ s. A 4 MeV alpha-particle creates about  $1.1 \cdot 10^6$  electron/hole-pairs in the detector, which after the pre-amplifier results in a voltage pulse of about 12 mV. Therefore, an energy and position resolution of about 0.5% FWHM seems feasible. This corresponds to about 24 keV and 0.14 mm, respectively.

The minimum noise level and the associated optimum shaping time are largely determined by the resistive layer  $R_d$  of the PSD. It is calculated that if  $R_d$  is increased, the minimum noise level decreases for all signals and the optimum shaping time increases. For  $R_d \rightarrow \infty$ , a shaping-time in the order of 1  $\mu$ s gives a noise level of about 10  $\mu$ V. In practice, however,  $R_d$  is fixed for a given PSD. Furthermore, increasing  $R_d$  without decreasing  $C_d$  will increase the ballistic deficit and reduce the linearity.

In section 2.4.2, the condition  $\tau_{sh} > 5.26 \cdot R_d C_d / \pi^2$  ( $=1.9$   $\mu$ s) was found to reduce the ballistic deficit and to improve the linearity. Hence,  $\tau_{sh}$  should be in the order of a few  $\mu$ s which,

however, reduces position and energy resolution. For a shaping time of  $\tau_{sh}=3 \mu s$ , it can be calculated that for a 4 MeV alpha particle, the position resolution amounts to about 0.3 mm and the energy resolution to about 145 keV. In practice, the latter would be unacceptable for charged-particle spectroscopy.

Notice that the theoretical total noise for the position signals is somewhat smaller than for the energy signal and that this is achieved at a somewhat larger shaping time. This suggests that the sum-signal of the position contacts may give a better resolution in the energy measurement than the energy signal itself, also because of correlated-noise cancellation effects. This has not been investigated further.

## 2.4.5 Characterization measurements

### *Detector resistance and capacitance*

The resistance  $R_d$  and the capacitance  $C_d$  of the SiTek type 1L30 PSD were measured. By measuring the dc resistance between the two position contacts, using an Ohm meter, it was found that  $R_d=60 \text{ k}\Omega$ . The detector capacitance was measured, as a function of bias voltage  $V_b$ , using an ac voltage-dividing network. As expected, the capacitance decreased with bias voltage and at  $V_b=80 \text{ V}$  it was found that  $C_d=60 \text{ pF}$ .

### *Detector and system noise*

Noise measurements were performed using a Hewlett-Packard 3400A rms voltmeter connected to the output of the shaping amplifier, which on its turn was connected to the pre-amplifier and the PSD.

In contrast to the theoretical calculations, it was found that the measured rms noise voltage  $|v_{out}|$  decreases with increasing shaping time  $\tau_{sh}$ . This motivates the choice of  $\tau_{sh}=3 \mu s$  for all following experiments, which gives good linearity, a relatively low noise level and not too much pile-up. An external noise source, which has not been taken into account, must be responsible for this discrepancy between theory and practice.

At a shaping time of  $\tau_{sh}=3 \mu s$ , the rms voltage of the noise  $|v_{out}|$  was found to decrease with increasing bias voltage. From theory, however, this is not so obvious. The detector capacitance  $C_d$  decreases with increasing bias voltage  $V_b$ , which would reduce the noise  $|v_{out}|$ , especially for the position signal. On the other hand, the leakage current  $I_l$  increases with increasing bias voltage  $V_b$  and this, on its turn, would increase the noise  $|v_{out}|$ . It was decided to use a bias voltage of  $V_b=80 \text{ V}$  in the following measurements, which gives full depletion of the detector and the smallest detector time-constant  $\tau_d$ .

### *Rise-time and ballistic deficit*

Rise-time measurements were performed using a radioactive AmCm alpha source and a movable slit in front of the PSD. For various slit positions and hence positions of incidence  $x$ , the pre-amplifier output pulses at both the position and energy contacts were recorded with a digital storage oscilloscope. By applying an exponential fit function, the pulse rise-times and

heights were determined. As expected from theory, the largest pulse rise-times were observed at  $x=L/2$ . From theory, it was also derived that the charge-collection time  $t$  should be larger than  $4.915 \cdot \tau_d = 1.8 \mu\text{s}$ , to limit the ballistic deficit to 1%. The pulse rise-time and height measurements support this theoretical condition. It was found that a charge collection time larger than about  $1.5 \mu\text{s}$  is required to limit the ballistic deficit to 1%, for all signals. This corresponds to a lower limit for the shaping time  $\tau_{sh}$  of about  $1.6 \mu\text{s}$ . In the following measurements, a shaping time of  $\tau_{sh}=3 \mu\text{s}$  was used. Although this conflicts with the condition for minimal noise (section 2.4.4), this is done since, for lower shaping times, linearity is reduced much more than the resolution is improved.

#### *Position linearity and resolution measurements*

From the rise-time and pulse-height measurements, using the AmCm alpha source and the movable slit, the position linearity and resolution can be determined. The accuracy is, however, limited by the finite slit width and the divergence of the alphas emitted from the AmCm source. Therefore, the PSD was positioned in the focus of the Eindhoven scanning ion microprobe set-up [1]. A 4 MeV  $\text{He}^+$  beam with a spot size of  $\sim 2 \mu\text{m}$  and a current of  $\sim 1000$  ions/s was used. In this way, the PSD can be irradiated with a position accuracy of a few  $\mu\text{m}$ .

The PSD was irradiated at ten points along its active area, equidistantly spaced at 2.5 mm, with known reference to the PSD edge. The PSD is moved, with respect to the focussed ion beam, using the stepper motors of the target wheel. The PSD signals are amplified by the pre-amplifiers and shaped and amplified by the shaping-amplifiers with equal gain and shaping time-constants  $\tau_{sh}=3 \mu\text{s}$ . Since the beam-energy spread is limited to about 1 ‰ (a few keV), the position signals should show a linear dependence on the position of incidence.

In Fig. 2.15, the measured pulse-height histograms for position signal  $Q_{p2}$  are shown, normalized to equal yields. A Gaussian fit of each peak was used to determine the mean pulse-height (channel) of the position signal for each irradiation position and the position resolution.

In Fig. 2.16, the mean pulse-height is plotted vs. the known position of incidence, for each of the position signals. A linear least-squares (LSQ) fit was performed, from which the position calibration and the position non-linearity were derived. Subsequently, this calibration was used to convert the horizontal axis of Fig. 2.15 from channels into position units.

It was found that the position resolution is better than 0.47 mm FWHM, which corresponds to 1.6% FWHM of the detector length. It is assumed that the beam-spot size of about  $2 \mu\text{m}$  and the beam-energy spread of about 1 ‰ can be neglected.

The deviation from linearity shows a sinusoidal shape, which is caused by the ballistic deficit. This ballistic deficit amounts to less than  $40 \mu\text{m}$ , which corresponds to a position linearity better than 0.15% of the detector length.



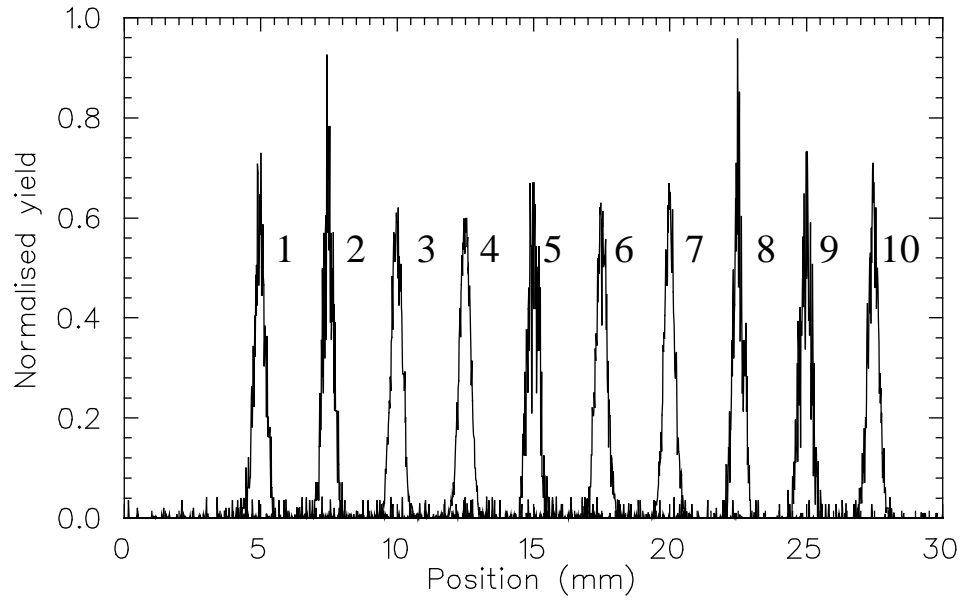


Fig. 2.15: Measured normalized pulse-height histograms of position signal  $Q_{P2}$ , for all ten irradiated points.

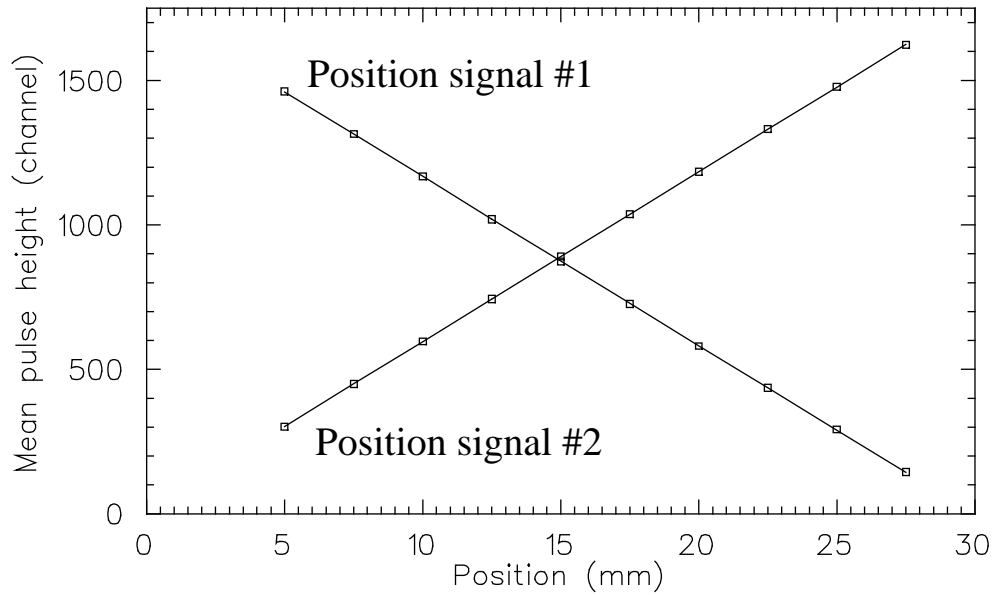
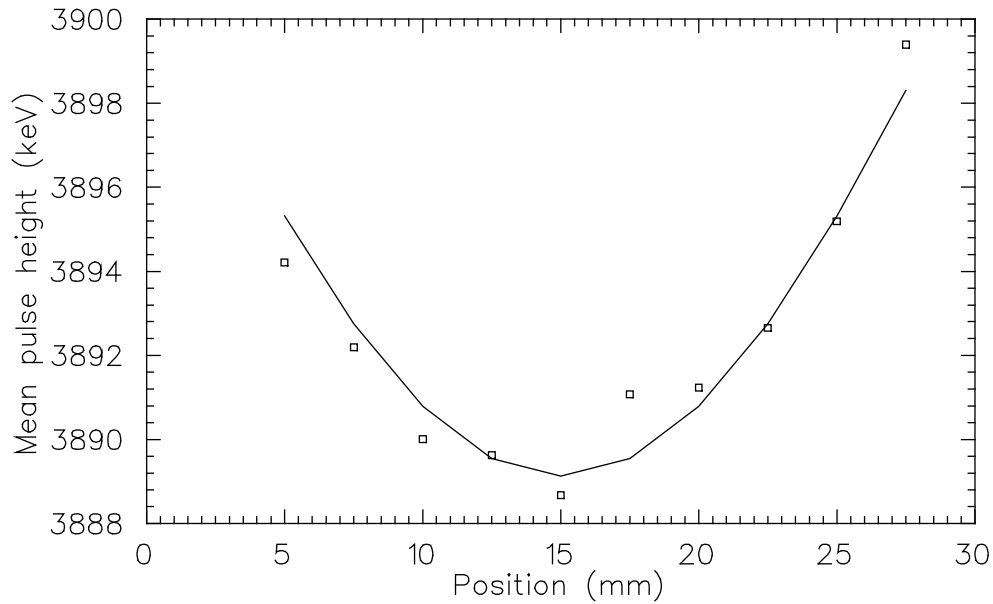


Fig. 2.16: Mean pulse height as a function of irradiation position, for each of the two position signals. Experimental data are plotted, together with a linear LSQ fit.

### *Energy linearity and resolution measurements*

For the energy signal, measurements similar to those for the position signals were performed. Gaussian fits of the energy pulse-height histograms yielded mean pulse height of the energy signal and energy resolution, for each irradiated point. The energy resolution amounts to about 36 keV FWHM for 4-6 MeV helium ions, which was found by irradiating a small region of the PSD using both the microprobe and an AmCm alpha-source. The latter measurement was also used for the energy calibration. Fig. 2.17 shows the measured mean pulse-height for the energy signal as a function of irradiated position. A sinusoidal non-linearity was observed in this mean pulse-height of the energy signal, which agrees with the theoretical ballistic deficit (section 2.4.2). The ballistic deficit amounts to less than 12 keV, which corresponds to an energy linearity better than 0.3%.



*Fig. 2.17: Mean pulse-height as a function of irradiation position, for the energy signal. Experimental data are plotted, together with a sinusoidal LSQ fit.*

### 2.4.7 Conclusions

Both theoretical noise calculations and experimental characterization measurements of the SiTek type 1L30 position sensitive detector and the associated amplifier chain, including the self-made pre-amplifiers, have been presented.

From the noise calculations it follows that with this system, a position resolution of about 0.14 mm and an energy resolution of about 24 keV are feasible. This performance is largely determined and limited by the thermal noise from the resistive charge-dividing layer of the

PSD. An increase of this detector resistance can improve the noise performance, but will affect the linearity if the detector capacitance is not reduced proportionally.

The position and energy signal linearity are also reduced due to the ballistic deficit if the shaping time-constant is too small. Calculations show that, to ensure sufficient position and energy linearity, a shaping time is required, that is much larger than the optimal shaping time for minimum noise performance. The improvement in linearity has to be weighted against the loss in position and energy resolution.

From the characterization measurements, using a shaping time of  $\tau_{sh}=3 \mu s$ , it follows that the position linearity is better than 0.15% of the detector length and that the energy linearity is better than 0.3% of the signal height. The measured position resolution, at this shaping time, is 0.47 mm and the measured energy resolution is 36 keV. The noise performance as calculated from theory cannot be realized in practice, probably due to an unknown noise source.

The measured position resolution and linearity are sufficient to use this type of PSD as an angle-disperse detector in ion-scattering experiments, with an angle resolution of less than one degree. For charged-particle spectroscopy, however, the energy resolution, both calculated and measured, is not good enough. Reduction of the contribution of one or more noise sources, like for example the detector leakage current, seems necessary. Furthermore, use of a PSD with a higher resistance of the charge-dividing layer may improve noise performance.

## References

- [1] P.H.A. Mutsaers, Design and Realisation of the Eindhoven Scanning Proton Microprobe, (Ph.D. Dissertation, Eindhoven University of Technology, 1995).
- [2] SiTek Electro-Optics (www.sitek.se), Ögärdesvägen 13A, S-433 40 Partille, Sweden.
- [3] S.A.E. Johansson and J.L. Campbell, PIXE A Novel Technique for Elemental Analysis, (Wiley, New York, 1988).
- [4] M.F.C. Willemsen, A.E.T. Kuiper, Nucl. Instr. and Meth. B61 (1991) 213-220.
- [5] D.H. Morse, G.S. Bench, S.P.H.T. Freeman, A.E. Pontau, Nucl. Instr. and Meth. B99 (1995) 427-430.
- [6] P. Lechner *et al.*, Nucl. Instr. and Meth. A377 (1996) 346-351.
- [7] D.H. Lumb, Nucl. Instr. and Meth. A290 (1990) 559-564.
- [8] W.-K. Chu, J.W. Mayer, M.-A. Nicolet, Backscattering Spectrometry, (Academic Press, New York, 1978).
- [9] G.F. Knoll, Radiation Detection and Measurement (Wiley, New York, 1989).
- [10] Canberra Semiconductor N.V. (www.canberra.com), B-2250 Olen, Belgium.
- [11] E. Steinbauer, P. Bauer, M. Geretschlager, G. Bortels, J.P. Biersack, P. Burger, Nucl. Instr. and Meth. B85 (1994) 642-649.
- [12] A.B. Rosenfeld, V.M. Pugatch, O.S. Zinets, P.G. Litovchenko, L.I. Barabash, Yu.N. Pavlenko, Yu.O. Vasiljev, Nucl. Instr. and Meth. A326 (1993) 234-238.
- [13] W.R.Th. Ten Kate, Nucl. Instr. and Meth. A253 (1987) 333-349.

- [14] E. Gatti, P. Rehak, Nucl. Instr. and Meth. 225 (1984) 608.
- [15] E. Laegsgaard, Nucl. Instr. and Meth. 162 (1979) 93-111.
- [16] M. Lindroos, Ö. Skeppstedt, Nucl. Instr. and Meth. A306 (1991) 225-228.
- [17] D.J. Burt, Nucl. Instr. and Meth. A305 (1991) 564-573.
- [18] L. Strüder, P. Holl, G. Lutz, Nucl. Instr. and Meth. A253 (1987) 386-392.
- [19] M.H. White *et al.*, IEEE J. Solid-State Circuits SC-9 (1) (1974) 1-13.
- [20] A. Owens, T. Mineo, K.J. McCarthy, A. Wells, Nucl. Instr. and Meth. A346 (1994) 353-365.
- [21] D.H. Lumb, J.A. Nousek, IEEE Trans. Nuc. Sci. 39 (1992) 1379-1383.
- [22] T. Roy, S.J. Watts, D. Wright, Nucl. Instr. and Meth. A27 (1989) 545.
- [23] S. Kalbitzer and W. Melzer, Nucl. Instr. and Meth. 56 (1967) 301-304.
- [24] A. Doebling, S. Kalbitzer and W. Melzer, Nucl. Instr. and Meth. 59 (1968) 40-44.
- [25] F. Verheul, Characterization and application of a one-dimensional position sensitive semiconductor particle detector in ion beam experiments, (Graduation thesis VDF/NK 96-19, Eindhoven University of Technology, 1996).
- [26] Burr-Brown ([www.burr-brown.com](http://www.burr-brown.com)), IC Data book, 1992.
- [27] A.F. Harvey, Microwave engineering, (Academic Press, New York, 1963)

# Chapter 3

## Radiation damage in silicon detectors caused and analyzed by a microprobe

*Charged-particle detectors are commonly used in ion-beam analysis experiments. In the work reported in this chapter, radiation damage effects in a particle implanted and passivated silicon (PIPS) charged-particle detector have been studied. This has been done through direct irradiation of the detector with a focussed ion microprobe. In this way, only specific detector areas are irradiated, depending on the beam spot size and the beam-scanning pattern, and relatively high areal doses may be applied. From the detector output pulses, the total ion dose and the pulse height are obtained. The pulse-height dependence on ion dose and the lateral differences of pulse height between non-irradiated and irradiated detector areas have been studied. This was done for both full and partial depletion of the detector.*

*The pulse height was found to decrease linearly with ion dose. This could already be observed after only a few ions per irradiated position within the beam-scanning pattern, which corresponds to a dose of roughly  $10^7$  /cm<sup>2</sup>. At full depletion of the detector, a pulse-height decrease of 8.0 eV per ion per scan position was measured, using 3.9 MeV He<sup>+</sup> ions. For a beam spot-size of about 20 μm<sup>2</sup>, this corresponds to a decrease of  $1.6 \cdot 10^{-9}$  keV·cm<sup>2</sup>. At partial depletion, a much more dramatic decrease of 48.8 eV per ion per scan position was found ( $9.8 \cdot 10^{-9}$  keV·cm<sup>2</sup>). For protons, a pulse-height decrease with ion dose of 0.6 eV per ion per scan position was measured ( $1.7 \cdot 10^{-10}$  keV·cm<sup>2</sup>).*

*Pulse-height changes were found to be restricted to the vicinity of irradiated detector areas. A pulse-height decrease was measured up to a distance of about 10 μm from the previously irradiated spots, at full depletion. At partial depletion, this distance increased to about 17 μm. The effect of the observed pulse-height changes on the accuracy of Scanning Transmission Ion Microscopy analyses with the microprobe is discussed.*

Related publication: “Study of localised radiation damage to PIPS detectors by a scanning ion microprobe: Measured effects and the consequences for STIM analysis”, D.P.L. Simons, A.J.H. Maas, P.H.A. Mutsaers, M.J.A. de Voigt, Nucl. Instr. And Meth. B130 (1997) 160-165.

### 3.1 Introduction

The lifetime of semiconductor particle detectors is limited by damage from charged-particle irradiation. Over the years, much effort has been put into studies of radiation damage in these detectors and some of its effects are relatively well known [1, 2]. For example, detector leakage current is known to increase linearly with irradiation dose. Usually, in these studies, the whole area of the detector under study is uniformly irradiated and damaged [3].

In the work reported here, a focussed ion microprobe is used, which can directly irradiate small, accurately defined areas of the detector, depending on the beam spot size and the beam-scanning pattern. In this way, relatively high areal doses may be applied and multiple regions of the detector may be studied separately. Effects of 3 MeV protons and 4 MeV  $\text{He}^+$ -ions on the pulse-height-to-energy calibration of a Canberra PIPS [4, section 3.2] charged-particle detector have been studied. The pulse-height dependence on ion dose and the lateral differences in pulse height between previously non-irradiated (virgin) and irradiated (damaged) detector areas have been determined.

Similar to the Ion Beam Induced Charge (IBIC) technique [5, section 3.4.2], the pulse height is recorded for each incoming ion. This is done for a large number of ions and a large number of positions of the micrometer-sized beam spot on the detector surface (scan position or pixel). The ion dose can be determined accurately from the total number of detector output-pulses, for each scan position. By combining the pulse-height measurements from a small ion dose interval and multiple scan positions, the accuracy in pulse-height-to-energy calibration is improved, as is the sensitivity to changes in this calibration.

This damage study is especially relevant for Scanning Transmission Ion Microscopy (STIM) [19, section 3.4.1] applications where, in bright-field mode, the detector is placed behind a thin sample and thus almost directly irradiated by the ion microbeam. The accuracy of the associated energy loss measurement increases approximately with the square root of the ion dose per scan position and resolutions as good as 1 keV have been reported [6]. This requires, however, doses of tens to hundreds of ions per scan position. It remains to be seen whether, in this case, the pulse-height-to-energy calibration is constant in time and independent of ion dose and scan position. If this is not the case, it can be corrected for if the dependence on ion dose and scan position is known. The latter is the objective of this work.

In the future, a wide range of measurements of semiconductor particle-detector properties using a scanning ion microprobe can be foreseen. Radiation-hardness tests and charge-collection efficiency studies, which might comprise a wider range of detector types, bias voltages, shaping-time constants, and ion types and ranges, are feasible. Especially the ability of the scanning ion microprobe to study position dependent properties, like depletion-layer thickness variations, is very promising. The extension of pulse-height measurements with transient current measurements and pulse-shape digitizing techniques is another interesting development.

In section 3.2, a description of the detector under study is given. In section 3.3, an overview of causes and effects of damage in Si detectors from ion irradiation is presented. Section 3.4

contains a description of the measurement techniques and data-analysis techniques used in this work, followed by the experimental procedures, in section 3.5. The results are presented and discussed in section 3.6. Conclusions and recommendations are given in section 3.7.

### 3.2 PIPS detectors

The charged-particle detector under study is a Canberra [4] passivated implanted planar silicon (PIPS) detector. This is a  $p^+n$ -junction diode detector, prepared from an  $n$ -type Si wafer, typically about 300  $\mu\text{m}$  thick, with a thin (50 nm), well-conducting, heavily-doped ( $p^+$ ) front-contact. This contact is created by low-energy implantation of boron, annealing and etching. Furthermore, an  $n^+$ -layer on the back-side forms a metallic contact to the bulk material. This is shown schematically in Fig. 3.1. The most important advantages of this type of detector compared to Surface Barrier detectors are a lower leakage current and a thinner, more homogeneous entrance window ( $p^+$ -layer).

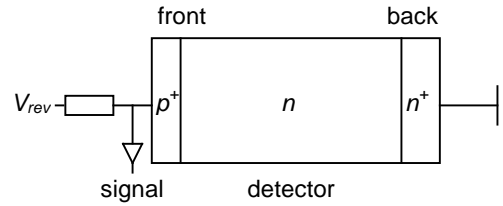


Fig. 3.1: Schematic layout of a PIPS  $p^+n$  junction silicon detector (not to scale)

At the  $p^+n$  junction, free electrons will diffuse from the  $n$ -type region into the  $p$ -type region, to equalize the free charge-carrier concentrations. The electrons will recombine with free holes creating a fixed negative space charge at the  $p^+$ -side of the junction and leaving a fixed positive space charge at the  $n$ -side of the junction. Due to this charge transfer by diffusion, a contact-potential  $V_0$  and an electric field  $E_0$  are present. All free charge carriers are swept out by this electric field and a depletion layer is created. Applying an external reverse bias voltage  $V_{rev}$  increases the thickness  $W$  of this depletion layer.

In case of a silicon  $p^+n$ -junction diode, in which the depletion layer mainly extends into the  $n$ -type material, one can write:

$$W = 0.53 \sqrt{\rho(\Omega\text{cm}) \cdot (V_{rev} + V_0)(\text{V})} \quad (\mu\text{m}) \quad (3.1)$$

with  $\rho$  the specific resistivity of the  $n$ -type material.

Apart from a thin ‘dead’ top-layer, the detector can be fully depleted, or even slightly over-depleted. In both cases, the region that is optimal for charge collection from incoming (ionizing) radiation is extended to cover the full detector volume.

In this work, a 100 mm<sup>2</sup> PIPS detector is used, that has a total thickness of 315  $\mu\text{m}$ , a bulk resistivity of 8700  $\Omega\text{cm}$ , and a nominal operating bias voltage of 60.0 V.

### 3.3 Detector radiation damage

#### 3.3.1 Causes of damage

In general, charged particles that move in (detector) material transfer their energy and momentum to electrons by excitation and ionization (electronic stopping) and to atoms by nuclear collisions (nuclear stopping). Recoiled atoms, on their turn, transfer a part of their energy into (secondary) excitation and ionization via electronic stopping. The remaining part of their energy is used to create lattice vibrations (thermal motion) and crystal damage.

In silicon detector material a 3 MeV proton, for example, loses most of its energy via electronic stopping. Less than 0.1% of its energy is lost in nuclear stopping processes.

In the excitation and ionization processes in silicon, recoiled electrons have energies up to 2 keV and will lose their energy through the creation of electron/hole pairs along their path. These electron/hole pairs give rise to the detector output pulse, when they move out of the depletion region because of the electric field and thus induce an electric charge at the contacts.

A large part of the energy transferred in nuclear collisions, however, does not contribute to electron/hole pair creation and the detector output-pulse. In the best case, the energy is used to generate lattice vibrations. If, however, the energy imparted to a silicon lattice atom in a nuclear collision is larger than the displacement energy  $E_d$  (around 20 eV for Si), the silicon atom is knocked out of its lattice site as a recoil. It can move away several lattice constants and a so-called *Frenkel-pair* is formed, consisting of an interstitial atom  $I$  and a vacancy  $V$ . These interstitials and vacancies can migrate through the crystal by diffusion, which gives rise to pair annihilation and formation of complexes between vacancies (di-vacancies), interstitials, and impurity atoms. These damage complexes are called *traps* or *point defects* [1, 2].

The Si recoil on its turn might, in addition to secondary ionizations, cause a cascade of short-range displacements. The associated high density of lattice defects enhances the formation of defect *clusters*, which are often electrically inactive.

Fortunately, the interaction between defects by thermal motion, during and after detector irradiation, causes a large fraction (up to 98% [7]) of the point defects and clusters to annihilate or decay to smaller clusters (*self-annealing*). The remaining defects rearrange, become stable and possibly more complex.

Heating cycles can be used to enhance annealing of damage and to remove defects and damage structures. However, the amount of vacancy-impurity complexes (carbon- and oxygen-vacancy complexes) might also increase with time or modest heating (*reverse annealing*). Single isolated defects have less pronounced reverse annealing effects than defect complexes and clusters [2].

#### 3.3.2 Effects of damage

Defects distort the lattice symmetry of the silicon crystal. This, in turn, creates discrete energy levels inside the forbidden band gap of the semiconductor material, especially for single



defects. Clusters of defects, on the other hand, are associated with a continuum of mid-band energy levels [1, 2]. Defect levels will act as either generation/recombination centers or as charge carrier trapping centers, in the latter case depending on their charge state (neutral and ionized, respectively).

The generation/recombination centers have deep energy levels which are located in the middle of the band gap, which gives them high transition probabilities and thus a high generation-recombination rate. This results in an increased leakage current, which will decrease the detector energy resolution (through increase of electronic noise). As a small, secondary effect, this leakage current may give a small voltage drop over the bias series resistor, thus decreasing the effective bias voltage and the electric field strength in the detector. This decreases the overall charge collection efficiency.

The trapping centers, on the other hand, are associated with energy levels near the band edges and will only interact with either the valence or the conduction band. If ionized, they will act as electron or hole traps. An increase of trap concentration will decrease the free charge-carrier lifetime and mobility and will thus affect the charge collection. Charge collection will be incomplete or delayed (in case of de-trapping), and the detector output-pulse shape is distorted. This results in pulse-height reduction after shaping, increased output-pulse rise-times, and possibly degradation of energy resolution.

The plasma effect is thought to be another cause of pulse-height reduction [8]. If an ion hits the detector, the charge carrier densities can be high enough ( $>10^{21} \text{ cm}^{-3}$ ) to create, around the ion track, a dense plasma column of electrons and holes, in which the electric field cannot penetrate. From an initial radius of  $\sim 1 \text{ }\mu\text{m}$ , the plasma column will grow radially, through outward diffusion, up to  $\sim 10 \text{ }\mu\text{m}$  in a few ns. The electric field can only extract electrons from the plasma column edges, until the plasma charge carrier density has decreased far enough to eliminate the plasma. Only then, the electric field is restored and charge can be collected. Although the radius of one damage track ( $\sim 10 \text{ nm}$ ) is small compared to that of the plasma, it causes, together with damage from previous incoming ions within the plasma column, an increased probability of charge recombination during the existence of the dense plasma and the absence of an electric field. This results in charge collection deficit and reduction in pulse-height, which is called the plasma effect.

For completeness, it is mentioned that, at very high doses of irradiation, type inversion of the semiconductor material by damage may occur. The formation of phosphorous-vacancies will decrease the number of shallow donor levels and the *n*-type silicon will eventually turn into *p*-type.

In conclusion, effects that can be expected from defects in a silicon detector are [2]:

- Increased leakage current
- Degraded energy resolution and pulse-height reduction
- Increased output-pulse rise times
- Material type changes

Of course, damage effects like leakage current increase, decrease of charge-collection efficiency, pulse-height reduction and energy resolution worsening are dose dependent.

A widely used parameter to monitor radiation damage is the detector leakage current. From various experiments ([2], [3]), it is concluded that the leakage current increases almost linearly with irradiation dose, with a certain threshold dose below which no effects are measurable. A similar behavior has been reported for the pulse-height-to-energy calibration [9]. A classic damage factor model is often applied [2], in which a proportionality constant  $K$ , or damage constant is defined, to relate the dose to the carrier recombination probability and thus to the leakage current.

The damage-effect increase may also be dependent on the rate at which the ion dose is applied, especially at high dose-rates, for example if the beam spot-size is reduced like in focused ion-beam irradiation [10]. The dose-rate dependence starts to play a role when defect introduction competes with dynamic defect annealing; defects have not stabilized and self-annealing is not complete before further defects are introduced.

## 3.4 Techniques

### 3.4.1 Scanning Transmission Ion Microscopy (STIM)

The Scanning Transmission Ion Microscopy (STIM) technique [6] is generally used in a microprobe set-up for the visualization of thin samples, such as organic tissue and of polymer domain formation. Sample visualization is required for accurate sample positioning before subsequent elemental analyses are performed. Sometimes, STIM is used to determine the areal mass-density distribution of a sample.

In STIM, the energy of ions is measured after their transmission through the sample. Since the detector is positioned directly behind the sample, a detection efficiency of almost 100% is achieved. Therefore, the beam current can be reduced to below 1 fA, while still obtaining a detection rate of  $\sim 1000$  ions/s. A low beam current allows one to reduce the microprobe diaphragm-slit widths, which generally results in a smaller spot size of the focussed beam than in elemental analyses. STIM visualizations therefore usually have a higher lateral resolution than elemental concentration distributions.

By scanning this beam spot across the sample and recording the energy of each transmitted ion, a mapping of the energy-loss signal can be made. In that case, the ions are assumed to be initially mono-energetic, which in practice is not completely true. Together with an estimate of sample composition and thus stopping power, the energy loss can be converted into an areal mass-density distribution. The uncertainty in the determination of the energy-loss is limited by the beam-energy spread, the energy-loss (Bohr) straggling in the sample, the detector resolution, the electronic resolution, determined by the noise in the amplifier chain, and the resolution and (differential) non-linearity of the analog-to-digital converter (ADC).

Conversion into areal mass densities gives an additional error from uncertainties in the elemental composition estimation and stopping power.

Combining the results of multiple measurements for each scan position can reduce the error in the determination of the energy-loss signals. Since beam-energy spread, energy-loss straggling, detector noise, and electronic noise are all (nearly) Gaussian, the total error is given by their squares sum. The uncertainty in the determination of the mean energy-loss is then given by  $\sigma/\sqrt{N}$ , with  $\sigma$  the standard deviation of a single energy-loss measurement and  $N$  the number of detected ions [6]. Data-analysis of multiple events per scan position (averaging over many particles) is treated in section 3.4.3. The improvement in energy-loss measurement by taking multiple measurements of course only holds as long as sample damage or detector damage do not play a role.

### 3.4.2 Ion Beam Induced Charge (IBIC)

The Ion Beam Induced Charge (IBIC) technique [5] is another imaging technique that can be applied in a scanning microprobe. In contrast to STIM, it is not based on energy-loss measurement, but on measurement of the induced charge in the sample itself. It is very suitable for imaging thin, buried depletion regions of microelectronic devices covered by thick surface layers [5] as well as defects and dislocations in semiconductor material [11]. Accurate positioning of the sample within the microprobe setup is then possible for subsequent diagnoses like radiation hardness tests and single event upset immunity tests [12].

A focussed ion beam (typically MeV protons or helium ions) is scanned across the device under study. During irradiation, the pulse-height from the device itself is measured, for each scan position. A detection efficiency close to 100% is achieved, making an extremely low beam current ( $\sim 1$  fA) and, consequently, a sub-micrometer beam spot-size possible.

Devices studied with IBIC typically have thin (a few  $\mu\text{m}$  thick) depletion regions on a thick (field free) substrate. The measured pulse-height results from charge collected within the depletion layer, and from charge collected from the field-free region outside the depletion layer by diffusion processes [5]. A mapping of the measured charge pulse-height will, if the image contrast is high enough, reveal depletion-layer regions as well as defect locations.

Like in STIM, to improve the signal-to-noise ratio and image contrast, multiple ions per scan position are measured, from which the most-likely pulse height is calculated (section 3.4.3). Furthermore, the image contrast can be improved by changing the ion type and energy, since the stopping power and thus the signal-to-noise ratio increases with atomic number  $Z$  and the ion depth range depends on the beam energy. However, improved statistics through higher dose and the use of higher  $Z$  ions to improve the signal-to-noise ratio increases the ion-induced damage. This will eventually degrade image contrast. Koh *et al.* [9] showed that only five helium ions per scan position were sufficient to obtain a reasonable IBIC image, and that this dose lies well below the threshold dose for observing a degraded pulse-height-to-energy calibration.

Breese [13, 5] and Sexton [12] modeled the IBIC charge collection and its degradation with dose, using parameters like ion type and energy, minority carrier diffusion length, depletion layer and dead layer thickness. Pulse-height reduction due to ion-induced damage can be predicted with the model, which is supported by experimental results. For ions that are fully stopped within the depletion layer, an almost linear decrease of pulse height as a function of dose was found. In contrast, for ions that have a range much larger than the depletion depth, a non-linear decrease of pulse height with dose was found. It was concluded that charge collection by diffusion is much more rapidly affected by ion-beam induced damage than charge collection by drift inside the depletion region.

Even more related to the work described in this chapter are the results of Angell *et al.* [11], who already in 1989 reported about Charge Collection Ion Microscopy (CCIM), which is similar to IBIC. They showed the first results of measurements on electrically active defects in a silicon *pn*-diode. The pulse-height from a region damaged with 2 MeV helium ions ( $2.4 \cdot 10^{11} \text{ cm}^{-2}$ ) was imaged, using a low additional dose of about 30 ions per scan position. The contrast in pulse-height was found to vary with bias voltage, supposedly due to changes in electric-field strength and its effect on trapping and recombination. They suggested to vary the depletion layer thickness to generate damage depth-profiles, and to apply pulse-shape analysis in addition to pulse-height analysis.

### 3.4.3 Data-filtering techniques

Although one ion per scan position would be sufficient to obtain a pulse-height measurement, it is common in STIM and IBIC to improve the accuracy of the pulse-height determination by taking the most-likely pulse-height from multiple measurements. The various ways in which the most-likely pulse-height can be determined from a distribution will be discussed.

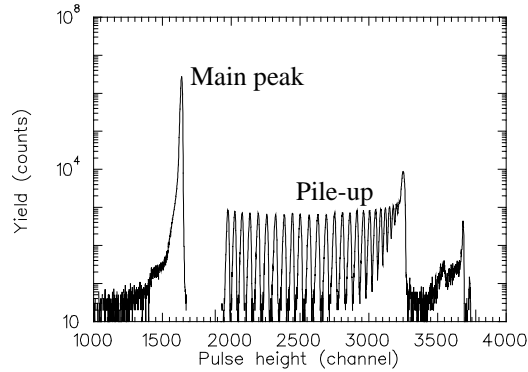


Fig. 3.2: Example of an IBIC pulse-height (sum-)histogram. STIM histograms have similar properties as IBIC histograms.

Fig. 3.2 shows a pulse-height histogram of the IBIC measurements on the charged-particle detector, which will be discussed below. These IBIC measurements are similar to STIM measurements without a sample in front of the detector. Notice that, for clarity, this histogram

has been summed over many ions and many scan positions. Usually, much less events per histogram are recorded.

In this histogram, the main peak corresponds to the distribution of measured pulse-heights around the most-likely pulse-height. The most-likely pulse-height is defined as the pulse-height that would have been recorded in an ideal detection system, without any peak broadening by statistics, noise, and other physical processes. In that case, a pulse-height measurement for only one ion would be sufficient.

The use of a logarithmic scale emphasizes small parasitic features, such as strange and outlying events, including pile-up pulses. Furthermore, it can be seen that the pulse-height distribution of the main peak is asymmetric and therefore not Gaussian, as is often assumed. The pulse-height distribution is determined by the beam-energy spread and the detector response function. The latter includes electronic energy-loss straggling in the dead layer, the distribution of the energy corresponding to excitation and ionization  $D_{s,e}$ , the statistics in electron/hole-pair creation, and the electronic noise. All of these are Gaussian, except for  $D_{s,e}$ , which is asymmetric [14]. Nevertheless, for most purposes, like in this work, the pulse-height distribution will be approximated by a Gaussian distribution, because this approximation has no significant effect on the results.

The most straightforward way to determine the most-likely pulse-height from a pulse-height histogram is to take the (weighted) *average* pulse-height value. For a large number of measured pulse-heights, that have a Gaussian distribution, this average value will converge to the most-likely pulse-height. However, strange and outlying events can have a large disturbing effect on the result, especially for a few measurements which, as mentioned above, is usually the case.

A way to reduce the effect of strange and outlying events, is to use *median filtering*. This selects the middle one of an ordered, odd set of measured pulse-height values. In case of an even number of values, the average of the middle two of the ordered set is taken. Although median filtering is less susceptible to strange and outlying events than average filtering, the best accuracy that can be attained is limited to the channel width of the pulse-height histogram, since only one value is selected. In case of averaging and a large number of measurements, the most-likely pulse-height can be determined with an accuracy that is below the channel width.

The effect of outlying events, such as pile-up, on the average pulse-height can be reduced by manual selection of a region-of-interest (ROI) that encloses the main peak and by discarding all events outside this ROI. One should, however, be conservative and careful when rejecting data, because for a Gaussian distribution, outliers are possible, and the probability of detecting an outlier increases with the number of measurements.

A filtering criterion that can be used for the selection and rejection of doubtful measurements is the *Chauvenet criterion* [15, 16, 17], which is an approximation of the Pierce criterion [17]. According to the Chauvenet criterion, a measurement from a set of  $N$  measurements of the same quantity  $x$  may be rejected if its probability of occurring is less than  $1/2N$ . Assume that

the measurement set has a Gaussian probability function with a mean  $\bar{x}$  and a standard deviation  $\sigma$ . Table 3.1 lists the maximum deviation  $d$  from the mean  $\bar{x}$  outside which measurements can be discarded. After rejection of doubtful measurements, the mean and standard deviation can be recalculated from the remaining measurements. Repeated application of the Chauvenet criterion may eliminate most or all measurements and should not be carried out [16].

*Table 3.1: Maximum deviations for the Chauvenet criterion. The maximum deviation  $d$  from the mean is given outside which events can be discarded.  $N$  is the number of measurements and  $\sigma$  their standard deviation.*

N	d/ $\sigma$	N	d/ $\sigma$
1	0.68	25	2.33
2	1.15	30	2.39
5	1.65	40	2.49
6	1.73	50	2.57
7	1.81	60	2.64
8	1.86	80	2.74
9	1.91	100	2.81
10	1.96	150	2.93
12	2.04	200	3.02
14	2.10	300	3.14
16	2.15	400	3.23
18	2.20	500	3.29
20	2.24	1000	3.48

The main contribution to strange and outlying events in this work is pile-up, which has the characteristic feature, displayed in Fig. 3.2, due to our pulsed cyclotron beam. Since pile-up should certainly not be used to determine the most-likely pulse-height and since pulse-heights much higher than those of the main peak are not expected, in this work a manual ROI selection is applied. This comprises selection of the main peak and its low-pulse-height tail. The upper margin is chosen just below the pile-up features (around channel 1800 in Fig. 3.2). The lower margin is chosen far below the main-peak and its tail, to cut away events in the lowest channels only, since these generally correspond to sampling errors.

In this work, the application of the Chauvenet criterion does not have a significant effect on the average pulse-height of the remaining events after manual ROI selection. The results for manual ROI selection with and without Chauvenet filtering before averaging are the same within 1%. Chauvenet filtering, without manual ROI selection, has not been studied in detail.

### 3.5 Experimental

#### 3.5.1 Experimental set-up

Experiments have been performed using the Eindhoven scanning ion microprobe set-up. A 3.9 MeV  $\text{He}^+$  beam was used and the beam current was reduced to less than 1 fA (about 3000 ions/s). The beam-spot size was  $(2.9 \pm 0.3) \times (2.3 \pm 0.3) \mu\text{m}^2$  Full Width at Half Maximum (FWHM). In contrast to the FWHM area, that contains about 70% of the Gaussian-shaped beam-spot intensity, the Full Width at Tenth Maximum (FWTM) area contains about 97% of the intensity. The FWTM was  $(5.0 \pm 0.5) \mu\text{m}$ , which, assuming an elliptic beam spot, corresponds to an area of  $(20 \pm 3) \mu\text{m}^2$  FWTM. The latter is used in the calculations below.

A new 100 mm<sup>2</sup> Canberra PIPS detector is placed in the focus of the microprobe (see Fig. 3.3) by mounting it in the target wheel. This detector has a total thickness of 315  $\mu\text{m}$ , a bulk resistivity of 8700  $\Omega\text{cm}$ , and a nominal operating bias voltage of 60.0 V.

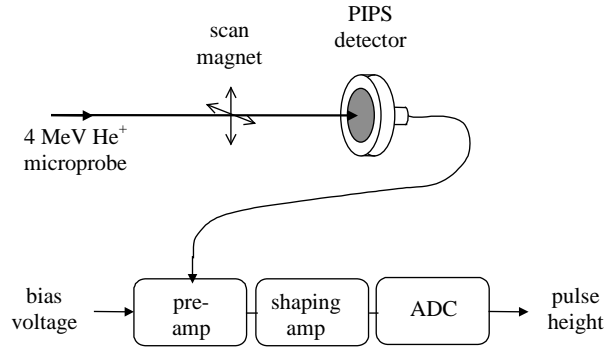


Fig. 3.3: Schematic experimental set-up

A scan pattern of  $128 \times 128$  points with a scan step-frequency of 10 kHz and a step size of  $(4.94 \pm 0.05) \mu\text{m}$  is selected, giving a total width of  $(632 \pm 8) \mu\text{m}$  for the area that is irradiated. The step-size has been derived from the calibration of the scan-magnet.

In each of the experiments, the detector is irradiated directly and the output pulse-height for each incident ion is recorded. This is done via a charge-sensitive pre-amplifier and a main-amplifier ( $\tau_{\text{shaping}} = 1 \mu\text{s}$ ), after which the pulse height is digitized and recorded together with the position of the ion beam. The collected data is stored in list-mode, in time intervals of about 10 seconds and at a count-rate of about 3000 cps.

The initial pulse-height-to-energy calibration is determined afterwards, using a radioactive AmCm alpha-particle source. This source irradiates the whole detector area in order to reduce the influence of damaged areas, if present, on the calibration. For 60.0 V bias, an initial pulse-height-to-energy calibration of 2.42 keV/channel was found. For 5.0 V bias, 2.57 keV/channel was found.

Two effects of damage were measured. First, the dependence of pulse height on ion dose was studied (section 3.5.2). Second, the position dependence of pulse height at a previously damaged region was studied (section 3.5.3).

### 3.5.2 Pulse-height vs. dose

To study the *dose dependence* of the pulse-height-to-energy calibration, a virgin area of the detector is positioned in the focus point of the scanning ion microprobe. In these measurements, it is assumed that the initial pulse-height-to-energy calibration and the sensitivity to damage are equal for the whole virgin area, which assumption will appear to be valid. This virgin area is irradiated for several hours with a scanning beam until a certain areal dose has been reached. During irradiation, the measured pulse-heights are recorded in list-mode. Afterwards, this list-mode data is divided into time intervals of 10 seconds. For each interval, the ion dose can be calculated from the number of events. The list-mode data from each interval is then sorted out into a pulse-height histogram.

Each histogram contains nearly 30000 events, thus improving the accuracy in the pulse-height determination through data filtering to a few percent of the histogram channel width (section 3.4.3). At the same time, the areal doses are kept low, because a large number of positions ( $128 \times 128$ ) is irradiated and the number of ions per scan position and time interval is limited to about two. Damage thus is not likely to affect the pulse-height distribution within one time interval, and data filtering may be applied without correcting for pulse-height loss. The applied ion dose is calculated from the cumulative sum of the number of ions detected in the preceding time intervals.

To obtain an areal dose, the area of irradiation has to be known. This can either be calculated from the scan-step size of  $(4.94 \pm 0.05) \mu\text{m}$ , or from the beam-spot size of  $(5.0 \pm 0.5) \mu\text{m}$  FWTM. In this work the beam-spot size is comparable to the scan-step size (see section 3.5.1) such that overlap of neighboring beam spots can be neglected. The beam-spot size of  $(20 \pm 3) \mu\text{m}^2$  FHTM is used to calculate areal dose, instead of the scan-position area ( $4.94 \mu\text{m} \times 4.94 \mu\text{m} = 24.4 \mu\text{m}^2$ ).

### 3.5.3 Pulse-height vs. position

To study the *position dependence* of the pulse-height-to-energy calibration in the vicinity of a previously damaged region, the detector is moved in such a way that the new scan pattern overlaps with a corner of the damaged area. Then, a short low-dose scan is made of less than 100 ions per scan position, corresponding to less than 4% of the damaging dose. This low-dose scan does not affect the existing pulse-height-to-energy calibrations significantly.

For each ion that hits the detector, the pulse-height plus beam-position are stored in list-mode. Afterwards, the data is sorted by beam position. In this way, for each scan position, a pulse-height histogram is obtained. After applying data filtering (section 3.4.3) to these histograms, the detector pulse-height response distribution can be plotted.



## 3.6 Results and discussion

### 3.6.1 Pulse-height vs. dose

Two *in-situ* measurements of the pulse-height decrease with ion dose were performed. In Fig. 3.4, the schematic layout of the irradiated areas is shown. The detector was biased at 60.0 V (nominal bias, overdepleted) for scanning area #1 and at 5.0 V (partially depleted) for scanning area #2. In both cases, the range of 3.9 MeV  $\text{He}^+$  ions ( $\sim 17 \mu\text{m}$  in silicon) is much smaller than the depletion-layer thickness.

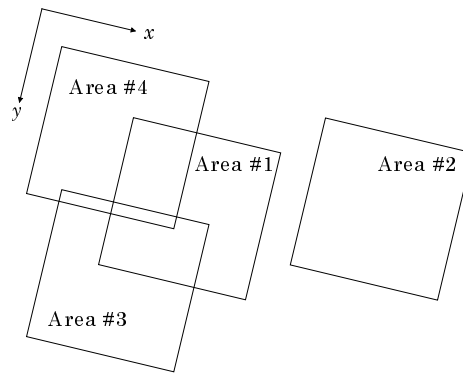


Fig. 3.4: Schematic layout of the detector areas that were scanned with the microprobe. Areas #1 and #2 are irradiated to study the pulse-height dependence on dose, at 60.0 and 5.0 V bias, respectively. Areas #3 and #4 are scanned shortly at 60.0 and 5.0 V, respectively, to study pulse-height variations over a partly damaged detector area. The scanned areas are slightly rotated as a result of scan-magnet misalignment. See text for further details.

A scan-magnet calibration procedure had revealed a misalignment of this magnet (a rotation around the beam axis by  $13.4^\circ$ ). This causes the square scan-pattern to be rotated with respect to the directions of the target-wheel movement, though this does not affect the results below.

During the irradiation of virgin area #1, at 60.0 V bias, about 2047 counts per scan position (pixel) were recorded, which corresponds to a total areal dose of  $(1.0 \pm 0.2) \cdot 10^{10} \text{ cm}^{-2}$ . During the irradiation of virgin area #2, at 5.0 V bias, on the average 677 ions per scan position were detected, corresponding to an areal dose of  $(3.4 \pm 0.5) \cdot 10^{10} \text{ cm}^{-2}$ . It was observed that the peak in the energy histogram shifted to lower energies with ion dose, much faster for 5.0 V bias than for 60.0 V, as can be seen in Fig. 3.5. Significant broadening of the individual peaks was not observed, which suggests that the effect of damage on pulse-height smears out, at least over the full area of the beam spot.

Fig. 3.6a shows the pulse-height as a function of the applied ion dose, at 60.0 V bias. This data was obtained by filtering the data in each time interval of 10 seconds, as described in section 3.4.3. The measurement suggests a linear dependence of the pulse height on dose. A linear least-squares fit through the data is shown (shifted down by 2 keV for clarity) in Fig. 3.6a.

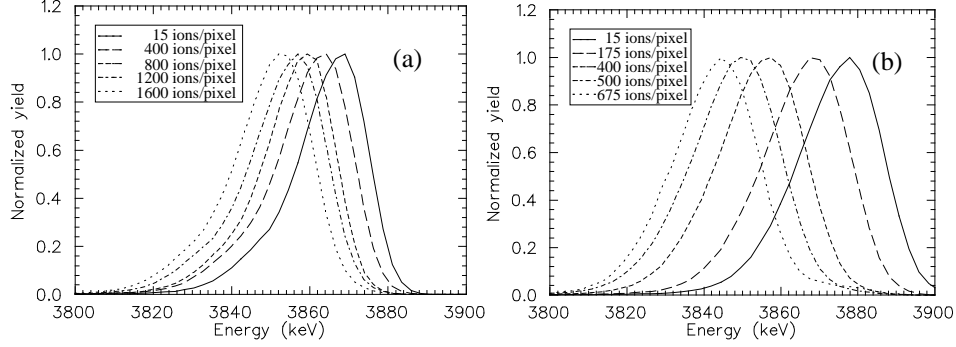


Fig. 3.5: The normalized main peak from the pulse-height histograms at several stages during irradiation, at 60.0 V (a) and 5.0 V (b) bias voltage. It is observed that the peak shifts from the initial pulse height down to a lower pulse height. This shift with dose is much faster at 5.0 V bias than at 60.0 V bias.

From this fit, the dose-dependent decrease of the pulse height is found to be 8.0 eV per ion/pixel, which corresponds to  $(1.6 \pm 0.2) \cdot 10^{-9}$  keV·cm<sup>2</sup>. The error in the areal dose dependence is largely determined by the uncertainty in the beam spot-size. The zero dose value of the energy response is found to be  $(3862 \pm 1)$  keV, which corresponds closely to the expected beam energy of 3.9 MeV. One should note that the exact beam energy of the cyclotron is not known. Furthermore, an inaccuracy in the initial pulse-height-to-energy calibration as determined using the AmCm calibration source might explain the difference.

The residual of the fit is plotted in Fig. 3.6b, which confirms the linear dependence of pulse height on dose, except for the first part, where the decrease is somewhat faster. The deviations from linearity (both the initial faster decrease and the overall fluctuations) could not be described by a dependence on *e.g.* count-rate, in contrast to what will be seen below, for the measurement at 5.0 V bias.

Fig. 3.7a shows the results of the measurement at 5.0 V bias, which are similar to Fig 3.6a, but now the pulse height decreases much faster. Furthermore, the deviations from linearity are much larger, which suggests a dependence on another parameter.

The detector pulse-height response was successfully fitted by a linear function ( $Energy = a \cdot Dose + b \cdot Count-rate + c$ ) of both the applied ion dose and count-rate. For the latter, the average count-rate for each interval of 10 s is taken. The following results were found:  $a = -48.8$  eV per ion/pixel,  $b = -1.59$  eV per ion/s and  $c = 3878$  keV. The pulse-height decrease with ion dose  $a$  corresponds to  $(9.8 \pm 1.5) \cdot 10^{-9}$  keV·cm<sup>2</sup>. This fit (on dose *and* count-rate) is plotted along with the measurement in Fig. 3.7a, where it is shifted down by 5 keV for clarity. Fig 3.7b shows the residual of this fit, which confirms the linear dependence of the pulse height on dose and count-rate. To illustrate the effect of dose on pulse-height, the part that is dependent on dose only ( $a \cdot Dose + c$ ) is plotted as a dashed line in Fig. 3.7a.

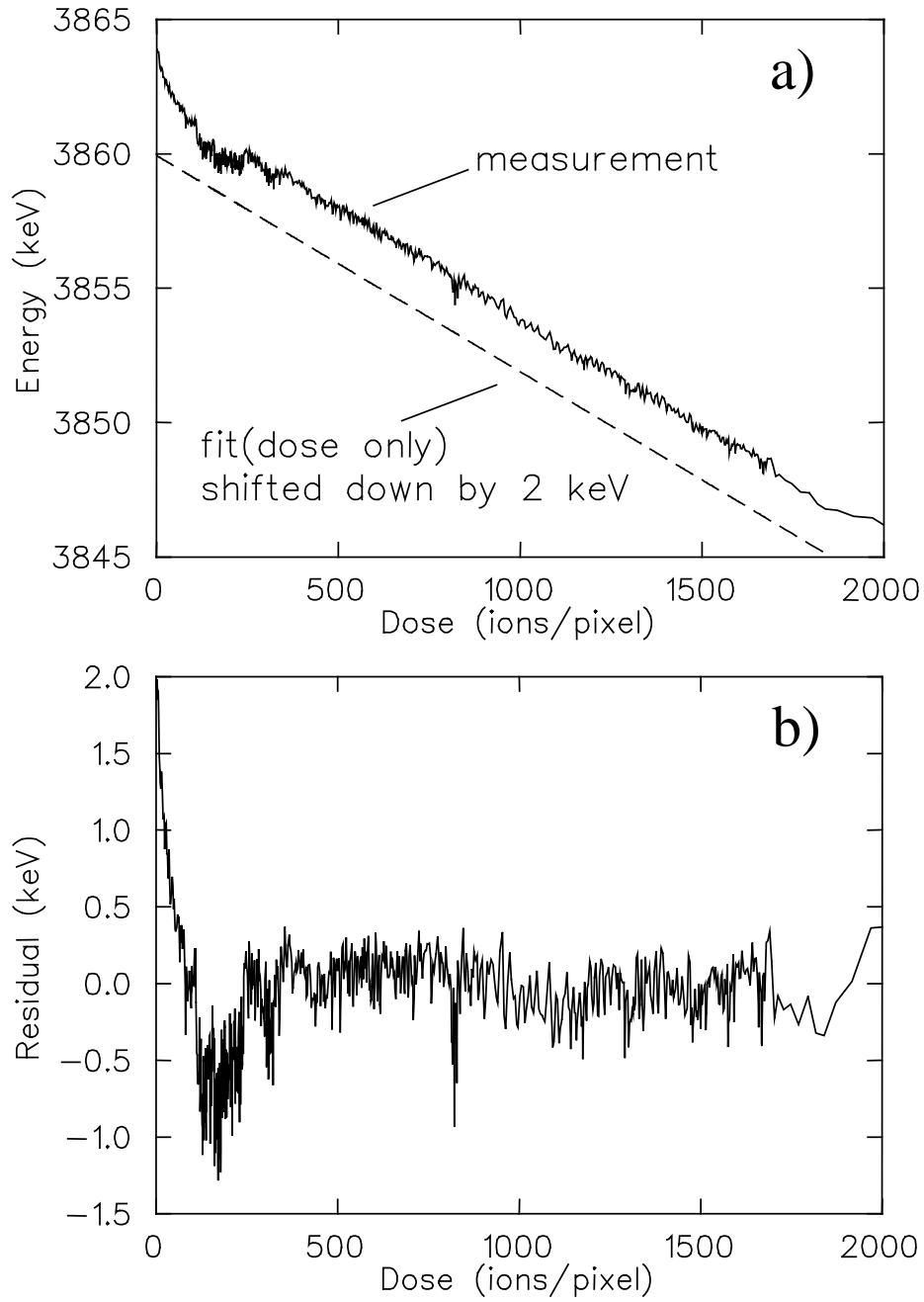
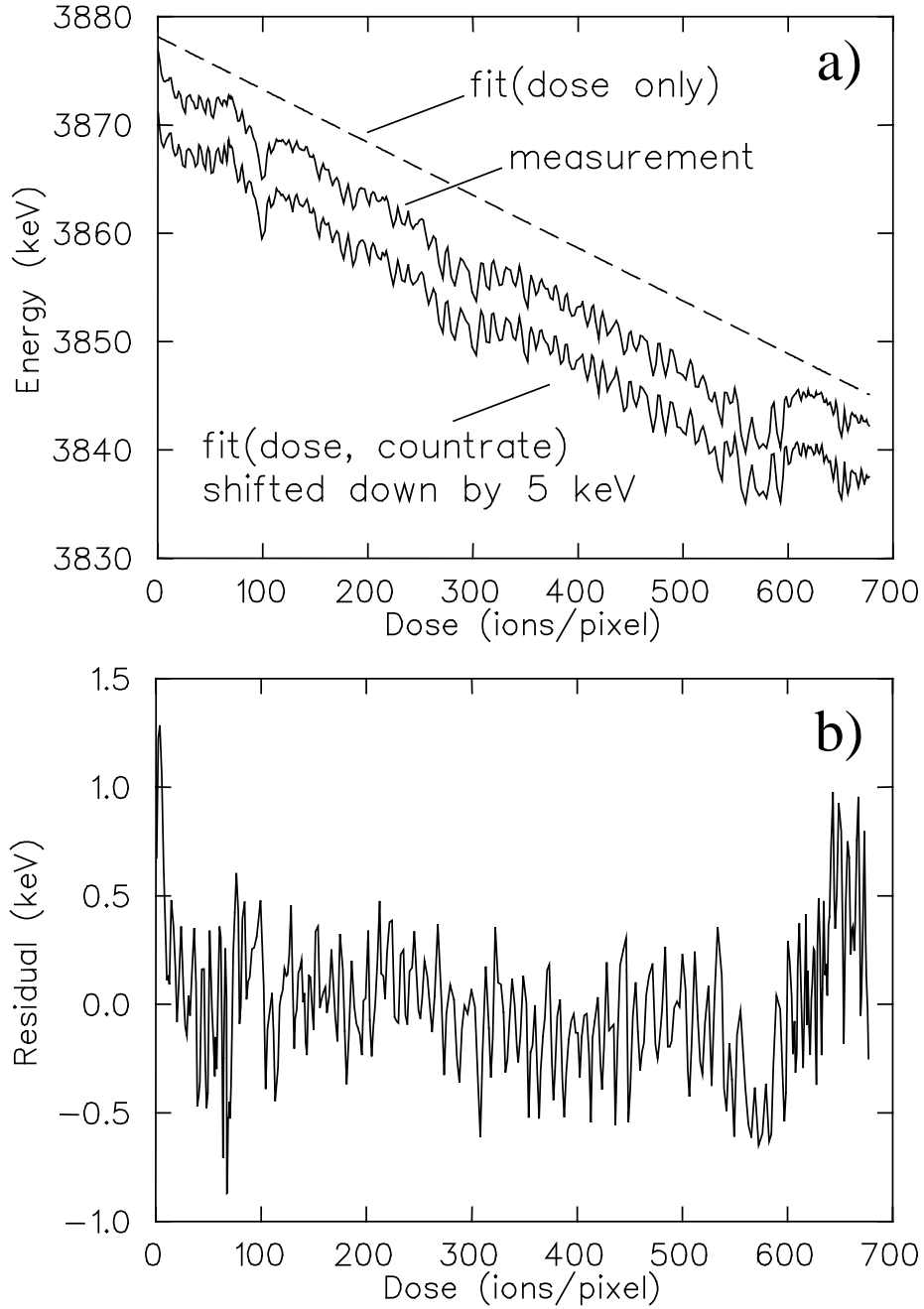


Fig. 3.6: a) Measurement of the pulse-height response as a function of applied ion dose at 60.0 V bias. A linear fit on dose (shifted down for clarity) is also shown. b) Fit residual.



*Fig. 3.7: a) Measurement of the pulse-height response as a function of applied ion dose at 5.0 V bias. A fit dependent on both dose and count-rate is shown. b) Residual of this fit. To show the dose effect on the pulse-height, the part of the fit that depends only on dose (see text) has been plotted as a dashed line in a).*

In the measurement of pulse-height vs. ion dose, a linear decrease has been measured. This decrease is observed already at a low ion-dose. The pulse-height loss is attributed to a decreased charge collection efficiency, which is caused by increased charge trapping and/or recombination effects. These effects are correlated to defect densities and thus to ion dose (see section 3.6.3).

The measured dependence of pulse height on ion dose is consistent with literature (section 3.4.2), in which a linear decrease is reported if the ions are fully stopped within the depletion layer. The latter is also the case in this work. Often, a threshold dose for observing pulse-height decrease is reported in literature. In this work, however, no such threshold dose was found. It is thought that the thresholds, as reported in literature, result from erroneous use of a semi-logarithmic scale in pulse-height vs. ion dose plots.

The accuracy in the determination of the most-likely pulse-height, for each time interval of 10 s, is about 0.1 keV. This is well below the channel width of the ADC, which is about 2.5 keV. The resolution of the pulse-height measurement, determined by the noise in the detector and the electronics, is about 15 keV, which is confirmed by the AmCm alpha-source calibration measurement. Thus, for the 30000 pulse-height measurements, that are used to determine the most-likely pulse-height, an accuracy of  $(15 \text{ keV} / \sqrt{30000}) = 0.1 \text{ keV}$  is attained. Since only about two ions per scan position are applied per time interval, the pulse-height decrease due to damage is kept below the accuracy of 0.1 keV. The differential non-linearity of the ADCs is specified as 1% of the channel width, and therefore does not affect the accuracy of 0.1 keV.

The observed initial, faster than linear, decrease of the pulse-height with dose has not been studied in more detail.

The pulse-height loss with ion dose was larger at 5.0 V bias (48.8 eV per ion/pixel) than at 60.0 V bias (8.0 eV per ion/pixel). This can be explained by the fact that the charge collection efficiency decreases with decreasing bias voltage, since the driving force of the electric field also decreases. For the detector used in these measurements, the electric field strength at the penetration depth of the 3.9 MeV  $\text{He}^+$  ions ( $\sim 17 \mu\text{m}$ ) is about 770 V/cm at 5.0 V compared to about 3000 V/cm at 60.0 V bias. At low electric field strengths, the charge-carrier drift-velocity is low, and radial diffusion can be large. Charge carriers that are liberated in the neighborhood of damage centers, have an increased probability of diffusing to the trapping centers. If this charge is trapped or if recombination occurs, the pulse-height will decrease.

Pulse-height changes with count-rate also have been measured. If these changes are large enough, they can be fitted and a linear decrease of pulse height with increasing count-rate is found. The observed dependence on count-rate probably has an electronic rather than a detector-intrinsic origin, like damage or self-annealing effects. The effect seems to be larger at lower bias voltages, and thus increased detector capacitance, and larger shaping-time constants. This has not been studied in more detail.

### 3.6.2 Pulse-height vs. position

To study the lateral damage distribution, two short scans (6 minutes each) were made of two different corners of the area #1 (see Fig. 3.4) which was previously damaged with about 2000 ions per scan position. The reverse bias voltage was set to 60.0 V for area #3 and 5.0 V for area #4. Additional ion doses for these measurements were  $\sim 50$  ions and  $\sim 70$  ions per scan position, respectively.

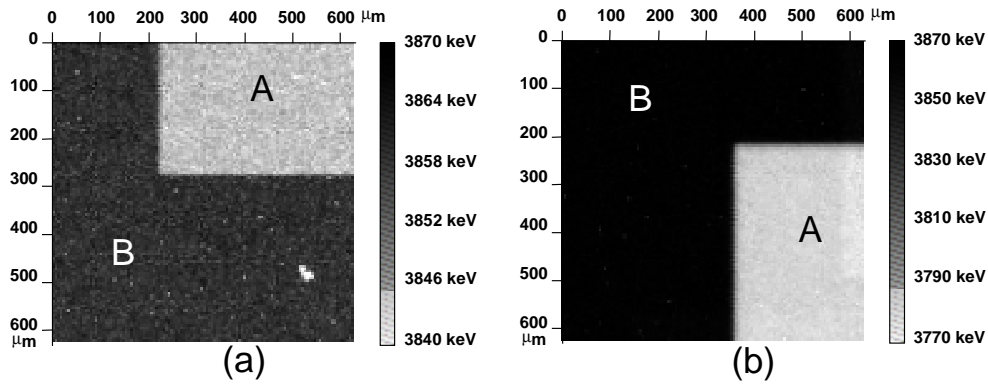
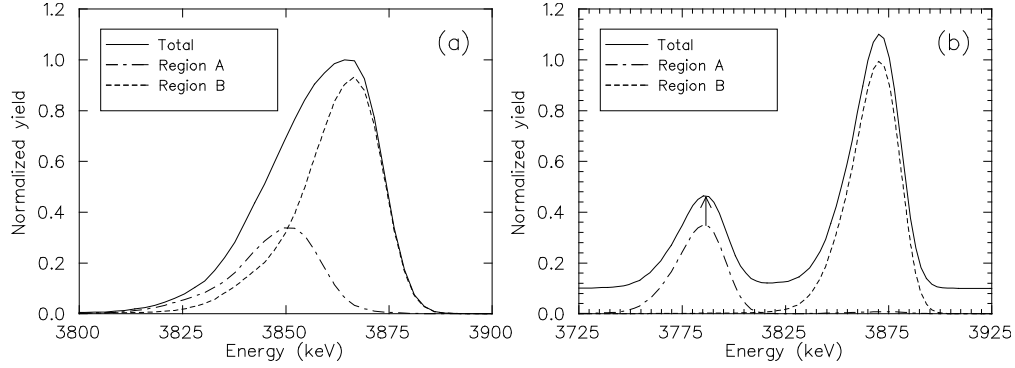


Fig. 3.8: Pulse-height distribution of a) area #3 at 60.0 V bias and b) area #4 at 5.0 V bias. Region A corresponds to a corner of the area #1 that was previously irradiated with a dose of about 2000 ions per scan position. Region B corresponds to a previously virgin area.

Fig. 3.8 shows the pulse-height distribution at a) 60.0 V and b) 5.0 V bias. In each map, two regions are clearly visible: region A, which corresponds to a corner of the already damaged region #1 and region B, which previously was virgin. Average pulse heights for region B correspond to 3861 keV (Fig. 3.8a) and 3866 keV (Fig. 3.8b), and are comparable to the zero-dose energy from the fits and the beam energy of about 3.9 MeV. For region A, the average response is 3846 keV at 60.0 V and as low as 3783 keV at 5.0 V bias. The pulse-height difference in this latter case corresponds to about 80 keV, or a pulse-height reduction of 2%. This is somewhat less than the decrease of  $(2000 \text{ ions} \times 48.8 \text{ eV/ion}) = 98 \text{ keV}$ , which would be expected from the dose-dependence measurement in section 3.6.1. This can be explained by the fact that the scan points in the short-scan areas #3 and #4 do not exactly coincide with the positions of the scan points in the damaged area #1. It was calculated that the beam spot centers are shifted by about  $(1.3 \pm 0.1) \mu\text{m}$ ; obviously the effect of damage on pulse height decreases with distance from the damage centers.

The effect of using a partially damaged detector area is illustrated in Fig. 3.9. Here, pulse-height histograms of the short scans are shown (solid lines) summed over all positions at 60.0 V bias (a) and at 5.0 V (b). Also shown (dashed lines) are the contributions of region A and B to these histograms. Clearly, use of a previously (partly) damaged area of a detector can cause energy-peak shifting, broadening, or even peak splitting, if contributions of virgin and damaged areas add up.



*Fig. 3.9: Contributions of the partial pulse-height histograms of regions A and B in Fig. 3.8a (60.0 V bias) and Fig 3.8b (5.0 V bias) to the total pulse-height histogram. a) It is clearly visible that peak broadening will occur if the contributions from damaged and undamaged regions are combined (60.0 V bias). b) Peak splitting occurs in the total pulse-height histogram (5.0 V bias), which is shifted up by 0.1 for clarity.*

Furthermore, the pulse-height-to-energy calibration across the edge between the irradiated area A and the virgin area B (Fig. 3.8) was analyzed, to study the lateral extent of damage in the vicinity of irradiated points and areas. In Fig. 3.10, the pulse-height response, averaged along the edge is plotted vs. the position. This is done for the measurements at both 60.0 V and 5.0 V bias. For each case, the pulse-height response across both the horizontal and the vertical edge is plotted.

These steps can be fitted with an error-function:  $PulseHeight = a + b \cdot \text{erf}(c \cdot Position + d)$ . From this fit the average position of the edge, the average pulse-height at both sides of the edge and, most importantly, the width (10-90%, FWTM) of the edge can be extracted. The results are shown in Table 3.2.

*Table 3.2: Fit results of the pulse-height change across the edge between the irradiated area and the virgin area, see Fig. 3.10.*

Fit of Fig. 3.10	Bias voltage (V)	Position edge ( $\mu\text{m}$ )	Edge width ( $\mu\text{m}$ FWTM)	Virgin area PH (keV)	Damaged area PH (keV)
a)	60.0	$x = 221 \pm 9$	$12.1 \pm 0.2$	$3861.0 \pm 0.2$	$3846.2 \pm 0.2$
b)	60.0	$y = 276 \pm 9$	$7.6 \pm 0.2$	$3861.1 \pm 0.2$	$3846.1 \pm 0.2$
c)	5.0	$x = 359 \pm 9$	$17.9 \pm 0.1$	$3865.9 \pm 0.2$	$3784.5 \pm 0.2$
d)	5.0	$y = 216 \pm 9$	$17.1 \pm 0.1$	$3866.0 \pm 0.2$	$3784.0 \pm 0.2$

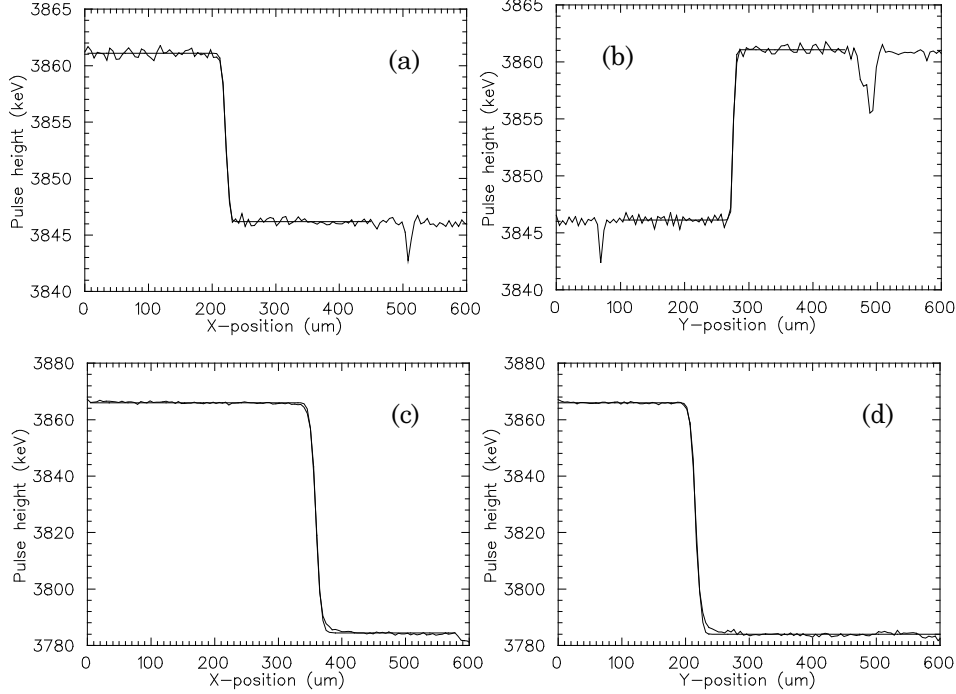


*Fig. 3.10: Pulse-height response across the edge between the damaged region A and the undamaged region B in Fig. 3.8. The measurement is plotted together with a fit function (see text). a) 60.0 V, horizontal cross-section of the edge, b) 60.0 V, vertical cross-section, c) 5.0 V, horizontal cross-section and d) 5.0 V, vertical cross-section.*

It can be seen that the influence of damage on the pulse-height-to-energy calibration extends outside the area of irradiated spots. This supports the suggestion in section 3.6.1 that the effect of damage on pulse-height smears out, at least over the full area of the beam spot. From these results it can be concluded that it also smears out over the distance of the scan step-size.

The measurements in this section show that the damage induced with the ion microprobe is confined to the irradiated area and its vicinity and that the pulse-height can vary significantly between an irradiated, and thus damaged detector area, and an undamaged area. The width of the pulse height variation across the edge between the damaged and the undamaged detector area has been determined. For the measurements with the 3.9 MeV  $\text{He}^+$  ions, this width was about 17  $\mu\text{m}$  FWTM at 5.0 V bias and roughly 10  $\mu\text{m}$  FWTM at 60.0V (see Table 3.2).

Basically, this width is determined by the distance over which damage centers, created by the (damaging) microprobe scan, can have an effect on the collection of charge carriers, created in ionization processes by the subsequent (probing) microprobe scan. Several factors determine this distance: 1) The spot-size and divergence of the ion beam in addition to the amount of overlap of both the damaging and the probing microprobe beam-spots, 2) The lateral range resulting from straggling of both the damaging and ionizing ions, 3) The depth distribution of



ionization and damage creation processes, and 4) The (lateral) diffusion of charge carriers, under the influence of an electric field.

In this work, the beam-spot size was about 5  $\mu\text{m}$  FWTM for both scans. The influence of beam divergence over a depth range of  $\sim 17 \mu\text{m}$  can be neglected. Calculations using the computer-code TRIM [18] show that the lateral range as a result of straggling of 3.9 MeV  $\text{He}^+$  ions in silicon is about 0.5  $\mu\text{m}$ , and that the creation of damage mainly occurs near the end of the ion tracks, at a depth of  $\sim 16.5 \mu\text{m}$ . This shows that the damage is confined to a small volume at a certain depth. In this work, the lateral damage distribution is fully determined by the beam-spot size.

The TRIM calculations also show that ionization takes place along the full ion track, with a maximum at a depth of about 15  $\mu\text{m}$ . Hence, charge carriers are generated in columns around the scan points, with a volume determined by the beam-spot size (for multiple ions) and the depth range of the ions. The interaction of the charge-carriers with damage obviously is influenced by the amount of overlap of the damaging and the probing microprobe beam-spots. From the scan-magnet and stepper-motor calibrations and the known scan-step size and target-wheel movement, it was calculated that the scan points of the probing scans of both areas #3 and #4 (see Fig. 3.4) were asymmetrically shifted by about 1.3  $\mu\text{m}$  with respect to the scan points of the damaging scan #1. Overlap of the beam-spots of the damaging and probing scan is thus slightly reduced. The somewhat asymmetric beam spot, together with the asymmetric shift, may explain the difference between the horizontal and the vertical edge-width measurements (see Table 3.2).

The diffusion of charge-carriers under the influence of the electric field may also cause them to interact with damage that lies outside the volume in which the ionization took place. This idea is supported by the measured edge-widths, that were a few times wider than the beam-spot diameters. Obviously, the diffusion range is larger at low bias voltages and field strengths, resulting in a larger edge-width at 5.0 V bias than at 60.0 V bias.

### 3.6.3 Protons vs. helium ions

It is common knowledge that protons produce less damage to silicon than helium ions of about the same energy. To study whether protons would give measurable pulse-height loss during detector irradiation, experiments similar to the ones in the previous sections were performed, but now using 2.94 MeV protons, the usual ion type and energy during microprobe analysis experiments, instead of 3.9 MeV  $\text{He}^+$  ions. The beam-spot size was about 30  $\mu\text{m}^2$  FWTM. A nominal bias voltage of 60.0 V was used, similar to common experimental conditions.

During the deposition of a total dose of about 900 protons per scan position, again a linear dependence of the pulse height on both ion dose and count-rate was found. The pulse-height decrease with ion dose was 0.6 eV per ion/pixel (about  $1.7 \cdot 10^{-10} \text{ keV} \cdot \text{cm}^{-2}$ ), and the count-rate dependence was  $-1.49 \text{ eV per ion/s}$ . The latter could only be fitted because of one sudden, large change in the beam current from the cyclotron and thus a large change in the count-rate

(~500 cps to ~ 2400 cps). Otherwise, the variations with count-rate would have been too small to be fitted.

Finally, short probing scans of the corners of a damaged area did not show sufficient contrast in pulse-height response to find an edge. This was the case for both nominal bias voltages and very low bias voltages.

The pulse-height decrease with dose of 0.6 eV per ion/pixel for 2.9 MeV protons is much less dramatic than the 8.0 eV per ion/pixel that was found for 3.9 MeV helium ions. The count-rate dependence of  $-1.49$  eV per ion/s is comparable to the value found for helium ions (at 5.0 V bias) and supports the idea that this dependence is caused by electronic effects.

From these findings it is estimated that, when using protons, either an increase in damage with at least a factor of ten, or a much longer probing scan (introducing additional damage!) will be necessary before pulse-height differences between damaged and undamaged detector areas will become distinguishable.

TRIM [18] calculations show that 3.9 MeV  $\text{He}^+$  ions lose about 0.33% of their energy in nuclear stopping processes, whereas for 2.94 MeV protons this is only 0.08%. This results in about 200 vacancies for each  $\text{He}^+$  ion, compared to about 40 vacancies for each proton. The MeV helium ions thus produce more damage than MeV protons, which results in a faster decrease of pulse-height with ion dose.

This factor of 4-5 in damage production cannot fully explain the difference of a factor of 13 in pulse-height loss with ion dose. For  $\text{He}^+$  ions, the damage is confined to a smaller volume than for protons. The radial range as a result of straggling for 3.9 MeV  $\text{He}^+$  ions is namely about  $0.5 \mu\text{m}$ , whereas for 2.94 MeV protons this is about  $3.8 \mu\text{m}$ . Furthermore, longitudinal straggling of these  $\text{He}^+$  ions ( $0.4 \mu\text{m}$ ) is much smaller than that of the protons ( $2.2 \mu\text{m}$ ). Thus not only the number of defects per  $\text{He}^+$  ion is higher, but also the volume in which they are created is smaller.

This difference in longitudinal and lateral range also causes ionization densities to be much higher for 3.9 MeV  $\text{He}^+$  ions than for 2.94 MeV protons. The plasma effect for  $\text{He}^+$  ions will be much stronger than for protons, and together with the higher defect densities and trapping, this may explain the missing factor in the pulse-height loss.

### 3.6.4 STIM vs. IBIC

During STIM measurements, the detector is not in the focus of the microprobe, as in the above IBIC measurements, but it is positioned a few centimeters behind a thin sample, out of the focus of the ion beam. To check whether pulse-height loss affects STIM measurements, experiments similar to the ones in sections 3.6.1 and 3.6.2 were performed, using a 3.9 MeV  $\text{He}^+$  microprobe with a beam spot-size of  $(3.4 \pm 0.3) \times (3.0 \pm 0.3) \mu\text{m}^2$  FWHM and a beam spot-area of about  $30 \mu\text{m}^2$  FHTM. This time, however, the same PIPS detector, biased at 60.0 V, was positioned a few centimeters behind the focus of the microprobe. Unfortunately, the beam-spot size and scan-step size on the detector surface are not known, but they can be estimated (see below). The detector output signal was recorded simultaneously with three

different shaping times:  $\tau = 0.5 \mu\text{s}$ ,  $\tau = 1 \mu\text{s}$ , and  $\tau = 3 \mu\text{s}$ . The latter was done to observe the effect of this shaping time on the speed of pulse-height decrease with dose, if any.

First, experiments were performed without a sample in front of the detector. At a count-rate of  $\sim 2000$  cps, about 600 ions per scan position were deposited on a virgin detector area. A pulse-height decrease with ion dose of 4.7 eV per ion/pixel was found ( $\tau_{\text{sh}} = 1 \mu\text{s}$ ). Comparing the results for the different shaping-times, it was found that the pulse-height decreases faster with ion dose for shorter shaping times ( $\tau_{\text{sh}} = 0.5 \mu\text{s}$ : 5.3 eV per ion/pixel,  $\tau_{\text{sh}} = 3 \mu\text{s}$ : 4.2 eV per ion/pixel). Because the beam-spot size is unknown, these values cannot readily be converted into an areal dose dependence. The dependence of pulse height on count-rate was too weak to be fitted. The residuals of the data for  $\tau_{\text{sh}} = 0.5 \mu\text{s}$  and  $\tau_{\text{sh}} = 1 \mu\text{s}$  showed an initial pulse-height decrease that is somewhat faster than linear.

Second, to check whether a partly damaged detector can affect the STIM measurements, the detector was moved (half a degree) to irradiate both the damaged part and a virgin part. Again, after a short scan, a distinct edge was observed between these regions. The width of this edge was about 7 scan-steps FWHM for all shaping-time constants. For shorter shaping-time constants, a larger contrast in pulse-height response was found, which confirms the faster pulse-height decrease with ion dose for shorter shaping-time constants. Damage therefore can result in a non-uniform pulse-height-to-energy calibration in STIM, at least without a sample.

Third, without moving the detector again, a thin ( $\sim 6 \mu\text{m}$ ), homogeneous poly-carbonate foil was placed in the focus of the microprobe, in front of the detector, to obtain an actual STIM set-up. A smooth density distribution of the film was obtained, and no contribution of the damaged detector area was visible. A similar result was obtained for a  $\sim 6 \mu\text{m}$  thin homogeneous Mylar foil instead of the poly-carbonate foil. This will be discussed below.

In STIM, the pulse-height-to-energy calibration is assumed to remain constant in time for all scan positions. In this work it is shown that, when directly irradiating the detector, this is not the case and that, at least for our PIPS detector, a dose of several hundreds of ions per  $\mu\text{m}^2$  generates a pulse-height reduction in the order of 1 keV. Moreover, if a partially damaged area of the detector is used, the pulse-height variations will result in a non-uniform distribution of the pulse-height-to-energy calibration, and the image structure of the sample under analysis may be distorted.

On the other hand, in the STIM set-up, the detector is positioned a few centimeters behind a thin sample, out of the focus of the ion beam. The beam spot size on the detector will thus be enlarged, depending on beam divergence. Furthermore, beam-spot broadening will occur by multiple scattering in the sample. This causes the damage to the detector to be less localized and the areal doses will decrease. Moreover, damaged regions will influence the imaging less dramatically, since their effect is smeared out.

Calculations show that, for the Eindhoven microprobe, at a few centimeters behind the sample the beam spot area has increased about 2-3 orders of magnitude because of beam divergence. However, the total scan area has increased by a factor of 2, at most, because this area is limited by the deflection of the scan magnet. Hence, instead of irradiating single, closely

spaced points, with little or no overlap, now the used detector area is irradiated uniformly because of the large overlap of the beam spots at the individual scan positions. Consequently, the areal dose is reduced by at most 1 order of magnitude. At a large number of ions per scan position, areal doses may thus still become high enough to cause a significant pulse-height reduction.

The experiments in this section show that, at least without a sample, significant pulse-height reduction can be observed if the detector is behind the focal plane of the micro-probe. Although the exact distance of the detector from the focal plane and hence the beam-spot size and scan-step size on the detector surface are unknown, it is estimated, using the microprobe set-up geometry, that the detector was about 2.5 cm behind the microprobe focal plane. Then the scan-step size on the detector surface was about 5.2  $\mu\text{m}$  and the total scan area thus has increased by only 11%. At the edge of the irradiated area, the measured width of about 7 scan-steps FWTM can then be converted to 36.4  $\mu\text{m}$  FWTM. Compared to the edge width of about 10  $\mu\text{m}$  that was found for the detector in the focus of the microprobe, this suggests that the beam-spot size on the detector out-of-focus has increased, but not drastically. Assuming, however, a uniform irradiation of the scan-area, the measured pulse-height reduction with dose of 4.7 eV per ion/pixel can be converted to  $1.3 \cdot 10^{-9} \text{ keV} \cdot \text{cm}^2$ , which is comparable to the  $1.6 \cdot 10^{-9} \text{ keV} \cdot \text{cm}^2$  that was found for the measurement in section 3.6.1.

Fortunately, when performing an actual STIM experiment on 6  $\mu\text{m}$  thin poly-carbonate and Mylar samples, no contribution of damaged detector areas could be seen. In this case, multiple scattering of ions traversing the sample probably smears out the effect of damage. During STIM analyses of very thin samples, however, detector damage could have an influence on image contrast and resolution, if no proper care is taken. Furthermore, protons instead of helium ions are often used in STIM, especially if subsequent trace-element analyses are to be performed. In this case, pulse-height loss with ion dose is less dramatic (section 3.6.3).

The count-rate dependence of the pulse-height may also affect STIM imaging. For protons, detected at nominal detector bias (60.0 V) and shaping ( $\tau=1 \mu\text{s}$ ), a pulse-height decrease with count-rate of 1.49 eV per ion/s was found. Especially at large beam-current fluctuations, this may significantly affect STIM imaging.

### 3.7 Conclusions and recommendations

The objective of this work is to study changes in the pulse-height-to-energy calibration of the charged-particle detector used in STIM analyses and to determine the implications of these changes for the STIM analyses. The same experimental configuration as during STIM analysis has been used, *i.e.* the charged-particle detector is directly irradiated by the scanning ion microprobe, in the absence of a sample in front of the detector. In this way, like in IBIC, changes in the pulse-height-to-energy calibration have been measured with increasing ion dose, between detector areas irradiated with different doses and, of equal importance, with varying count-rate. This has been done for both protons and helium ions.

For helium ions, a linear decrease of the pulse-height of several eV per ion/scan position has been measured. For protons, the measured decrease is about a factor of 10 lower. In case of several hundreds of ions per scan position, which is common in STIM analyses to improve the accuracy of the pulse-height measurement, this leads to changes in the pulse-height-to-energy calibration of up to 1 keV. This conflicts with the expected improvement of accuracy to below 1 keV. Furthermore, changes in the pulse-height-to-energy calibration were found to be restricted to the vicinity of irradiated detector areas. It is shown that simultaneous use of differently irradiated detector areas can lead to peak broadening or even peak splitting.

Fortunately, during actual STIM measurements, with a sample in front of the detector, the influence of damaged detector areas on the pulse-height distribution is found to be small. Still, it is recommended to avoid the use of already damaged detector areas. Furthermore, the distance between sample and detector should be increased as much as possible, to increase the used detector area and to decrease areal ion doses. Knowledge of the pulse-height loss with ion dose, as measured in this work, allows for the afterward correction for this loss, if necessary.

Of equal importance are the measured changes in the pulse-height-to-energy calibration with the beam current and thus count-rate. For a change in count-rate of 1000 ions/s, a change in pulse-height of about 1 keV has been observed. These count-rate dependent pulse-height changes are thought to be due to a non-linearity in the pre-amplifier amplification factor. This has to be confirmed by additional experiments.

In this work, the ions for which pulse-height loss was measured are the same ions that cause the damage. The ionizing ions have the same energy and thus the same depth range profile as the damaging ions. The depth at which most of the damage occurs (near the end of the ion range), however, does not exactly match the depth at which most of the charge carriers are generated. Future experiments may include studies in which range matching of damaging and ionizing radiation is applied. In this way, the effect of damage at a certain depth on the pulse-height of ions with exactly the same or a completely different range may be studied, possibly as a function of bias voltage and thus electric field strength. Furthermore, variation of the angle of incidence of the ion beam with respect to the damage tracks and the electric field may be used to study in more detail how damage affects charge-collection efficiency and thus pulse-height response.

## References

- [1] E. Borch, M. Bruzzi, Riv. del Nuo. Cim. 17 (1994) 1-63.
- [2] H.W. Kraner, Nucl. Instr. and Meth. 225 (1984) 615-618.
- [3] R. Grube, E. Fretwurst, G. Lindström, Nucl. Instr. and Meth. 101 (1972) 97-105.
- [4] Canberra Semiconductor N.V., B-2250 Olen, Belgium.
- [5] M.B.H. Breese *et al.*, J. Appl. Phys. 77 (1995) 3734-3741.
- [6] R.M. Sealock *et al.*, Nucl. Instr. and Meth. B29 (1987) 557-566.

- 
- [7] V.A.J. van Lint, Nucl. Instr. and Meth. A253 (1987) 453-459.
  - [8] E.C. Finch, Nucl. Instr. and Meth. 163 (1979) 467-477.
  - [9] M. Koh *et al.*, Nucl. Instr. and Meth B93 (1994) 82-86.
  - [10] R.A. Brown, J.C. McCallum, J.S. Williams, Nucl. Instr. and Meth. B54 (1991) 197-203.
  - [11] D. Angell, B.B. Marsh, N. Cue, J.-W. Miao, Nucl. Instr. and Meth. B44 (1989) 172-178.
  - [12] F.W. Sexton, IEEE Trans. Nuc. Sci. 43 (1996) 687-695.
  - [13] M.B.H. Breese, J. Appl. Phys. 74 (1993) 3789-3799.
  - [14] E. Steinbauer, G. Bortels, P. Bauer, J.P. Biersack, P. Burger, I. Ahmad, Nucl. Instr. and Meth. A339 (1994) 102-108.
  - [15] J.R. Taylor, An Introduction To Error Analysis (Univ. Sci. Books, Mill Valley CA, 1982) p. 142.
  - [16] H.D. Young, Statistical Treatment of Experimental Data (McGraw-Hill, New York, 1962) p. 76.
  - [17] W. Chauvenet, A Manual Of Spherical And Practical Astronomy, vol. II (J.B. Lippincott Company, Philadelphia, 1908) p. 558.
  - [18] J.F. Ziegler, J.P. Biersack, U. Littmark, The Stopping and Range of Ions in Solids (Pergamon, New York, 1985) <http://www.research.ibm.com/ionbeams/home.htm>.
  - [19] H. Lefevre *et al.*, Nucl. Instr. and Meth. B54 (1991) 363-370.

# Chapter 4

## $\mu$ PIXE study of organic semiconductor devices

*In this chapter, the study of two organic semiconductor device related effects with the  $\mu$ PIXE technique is presented.*

*First, for precursor-route pentacene-based field-effect transistors, the conversion efficiency of the precursor has been studied, as a function of conversion temperature. Since only the precursor leaving-group contains chlorine, the residual amount of chlorine in the organic layer was measured, to investigate the efficiency of the conversion en elimination process. A relation with the device performance has been found.*

*Second, for precursor-route poly-(phenylene-vinylene) based light-emitting diode structures, degradation of the indium-tin-oxide electrode by hydrochloric acid, which is released during precursor conversion, has been studied. The formation of  $\text{InCl}_3$  islands within the polymer layer will be shown.*

This work was done in collaboration with Philips Research Laboratories. In particular, Adam Brown and Peter v/d Weijer are acknowledged for their support.

## 4.1 Introduction

The electrical properties of conjugated polymers and oligomers have been of interest to worldwide research for almost two decades. At first, research was aimed at heavily doped organic systems, of *e.g.* polyacetylene, with metallic conductivity [1]. In the last decade, much interest lies in the lightly doped or undoped conjugated polymers and oligomers, because of their non-insulating, semiconducting, and electroluminescent properties [2], as well as the foreseen advantages over inorganic, solid-state material like silicon.

The (semi-)conducting properties of these polymers result from their delocalized  $\pi$ -electron system along the  $\pi$ -conjugated double bonds in their backbone [2]. Although the performance of organic semiconductors is inferior to that of single-crystalline silicon semiconductors, the potential advantages lie in the field of large area and/or non-planar flexible plastic electronics, like displays, back lights, smart chip-cards, and identification tags. Reduction of cost is also estimated to be an advantage.

Organic semiconductor devices that have been constructed include Schottky diodes [3], light-emitting diodes (LEDs) [4], thin-film metal-insulator-semiconductor field-effect transistors (MISFETs) [5,6] and photodiodes [2,7]. Initially, for these devices, only the active semiconducting layer was made of organic material. Recently, however, all-plastic electronic devices are reported [8].

A lot of problems have yet to be overcome. Device stability (both environmental and electrochemical) and device performance (*e.g.* light output, voltage amplification, operating frequency) have to be improved. These are directly related to the organic semiconducting properties (band-gap energy, *p*-type or *n*-type, charge-carrier mobility), to the physical and chemical structures, and to the purification thereof [2].

In measurements on actual devices, lateral position resolution in the order of a micrometer is often desirable. In studies, where precursor-conversion plays a role, sensitivity for minor or trace elements is required. The particle induced X-ray emission technique applied in a scanning ion microprobe ( $\mu$ PIXE) is known to offer a position resolution of a few micrometers and a sensitivity to trace elements of a few ppm. In this work, the results of two  $\mu$ PIXE studies of organic semiconductor device-related effects are presented.

For precursor-route pentacene field-effect transistors, the conversion efficiency as a function of conversion temperature was studied. For polymer electroluminescent diode structures, electrode-degradation was studied, that is caused by hydrochloric acid during precursor conversion.

An outline of the device manufacturing, layout, and operation of organic semiconductor devices will be given, in section 4.2 for the organic MISFETs and in section 4.4 for the organic LEDs. In section 4.3, the measurements on pentacene MISFETs are presented, and in section 4.5 the measurements on a poly(*p*-phenylene vinylene) (=PPV) LED structure are described. Conclusions are given in section 4.6.



## 4.2 Organic field-effect transistors

In this section, organic metal-insulator-semiconductor field-effect transistors (MISFETs) are described. Full details can be found in the extensive review by A.R. Brown *et al.* [5].

The schematic layout of the organic MISFET is shown in Fig. 4.1. A thick, heavily doped  $n^{++}$ -type silicon wafer forms the gate contact, on which an insulating layer of 200 nm  $\text{SiO}_2$  is thermally grown. A layer of titanium (10 nm), which acts as an adhesion layer, and subsequently a gold layer (90 nm), are thermally evaporated and photo-lithographically patterned to form the source and drain contacts. A typical source-drain geometry is presented in Fig. 4.5. The channel widths  $Z$  are typically 3-20 mm, and the channel lengths  $L$  are in the range of 2-20  $\mu\text{m}$ . Finally, a layer of the organic semiconductor is deposited, with a thickness  $t$  in the range of 10-100 nm. All samples are handled in air, and due to oxygen the organic layer will, unintentionally, be lightly doped into  $p$ -type semiconductor.

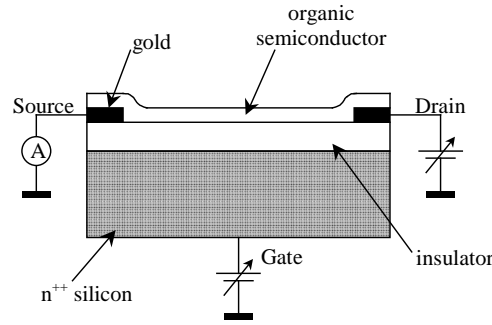


Fig. 4.1: Structure of an organic field-effect transistor.

Two parameters of the organic semiconductor film are essential for the operation of the MISFET: the conductivity  $\sigma$  and the field-effect charge-carrier mobility  $\mu$ .

The conductivity determines the ohmic source-drain current  $I_{sd}$  at a small drain bias voltage  $V_d$ , (in practice  $V_d = -1$  V) and zero gate bias voltage  $V_g$ . This is mathematically shown in Eq. 4.1:

$$\sigma \approx \left( \frac{L}{Zt} \right) \frac{I_{sd}}{V_d} \bigg|_{V_g=0, V_d \rightarrow 0} \quad (4.1)$$

By applying a negative bias voltage  $V_g$  to the gate, a positive charge accumulation layer is created at the semiconductor/insulator interface. If this charge is mobile, the source-drain current  $I_{sd}$  for a given  $V_d$  may increase. By measuring the change in  $I_{sd}$  as a function of  $V_g$ , at a given  $V_d$ , the field-effect mobility  $\mu$  may be calculated. This is shown in Eq. 4.2, with  $C_i$  the capacitance per unit area of the insulating layer:

$$\mu = \mu(V_g) = \left( \frac{L}{ZC_i V_d} \right) \frac{\partial I_{sd}}{\partial V_g} \bigg|_{V_d \rightarrow 0} \quad (4.2)$$

Applying a positive bias voltage to the gate will lead to depletion of charge carriers, starting at the insulator/semiconductor interface. In this way, a reduction in the source-drain current is realized. Therefore, the source-drain current can be modulated via the gate bias voltage.

For transistors to be used in commercial applications, high operating speeds ( $>10$  kHz) and high current modulations (on/off ratio  $>10^3$ ) are required. For high operating speeds, high charge-carrier mobilities are required. One way to achieve this is by intentional chemical doping [9]. In this way, mobilities in the order of  $0.1$ - $1$   $\text{cm}^2/\text{Vs}$ , comparable to amorphous silicon, have been obtained. However, doping also increases the conductivity of the semiconductor. This may affect the current modulation of the MISFET, which depends on  $(\mu/\sigma)$ .

Therefore, another approach instead of doping is applied. The intrinsic charge-carrier mobilities can be improved by increasing the amount of molecular order in the organic film, since this will enlarge the  $\pi$ -conjugation lengths. In this way, mobilities of  $10^{-5}$ - $10^{-4}$   $\text{cm}^2/\text{Vs}$  for poorly ordered systems have been improved to better than  $0.1$   $\text{cm}^2/\text{Vs}$ .

Several processing options have been reported, including electrochemical polymerization of a soluble monomer and vacuum deposition of small oligomers. For example, sublimed films of  $\alpha$ -sexithiophene oligomers, for which self-assembly leads to a crystalline structure, have shown mobilities as high as that of  $\alpha$ -Si. Both of these processing techniques, however, show little (commercial) advantages over  $\alpha$ -Si.

In this work, measurements have been performed on MISFET structures of which the organic layer has been deposited via a precursor route by spin coating. In that case, soluble precursor molecules, having side-groups and/or a broken through-conjugation, are spun from a solution onto the device substrate. Subsequently, the deposited layer is converted, for example by heat treatment, into the required, insoluble through-conjugated oligomer. Here, pentacene oligomers are used.

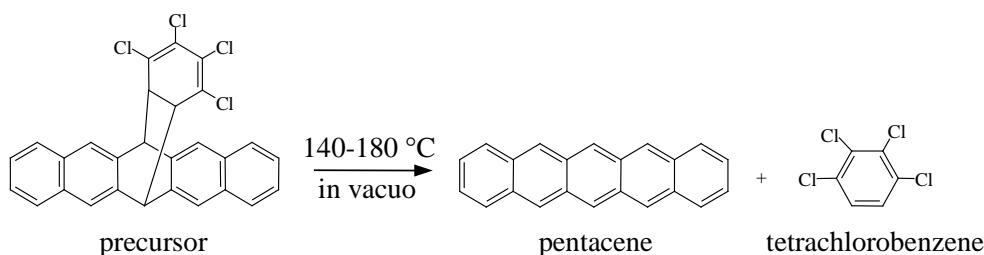


Fig. 4.2: Schematic overview of the conversion of precursor into pentacene and tetrachlorobenzene. The latter is to be eliminated (From [5]).

Fig. 4.2 schematically shows the conversion process of a precursor molecule [10] to pentacene, which is soluble in dichloromethane, and can be spun into amorphous films with a thickness of 10-100 nm. Via a heat treatment under vacuum, the precursor molecules are converted into pentacene (the organic semiconductor) and a tetrachlorobenzene *leaving group* that should be eliminated. Notice that only the leaving group contains chlorine. Hence, the amount of chlorine in the layer is a measure for the amount of (residual) leaving groups. During conversion, a morphological change in the film is clearly visible. Apparently, microcrystallites (confined crystalline areas on sub-micrometer scale) are formed, but the exact morphological structure depends very much on the conversion conditions [11].

For MISFET devices based on precursor-route poly(2,5-thienylene vinylene) (= PTV), it was shown earlier [6] that the charge-carrier mobility depends (linearly) on the conversion ratio of the precursor into semiconducting PTV. It was concluded that this was a result of the increasing effective  $\pi$ -conjugation length, as more through-conjugated polymer is formed with increasing conversion ratio. The latter was monitored using infrared spectroscopy techniques. Initial  $\mu$ PIXE measurements (see below) at Eindhoven University of Technology showed that, compared to an unconverted pentacene precursor film, still about 30% of the chlorine content was left over in a pentacene film that was converted under usual conditions (140 °C) at Philips. This indicated incomplete precursor conversion. Based on this new knowledge, for a conversion-temperature range of 120 °C - 220 °C, MISFET devices with a 60 nm thick organic film were converted under vacuum for 20 min, after which their electrical properties were measured (see [5] for experimental details).

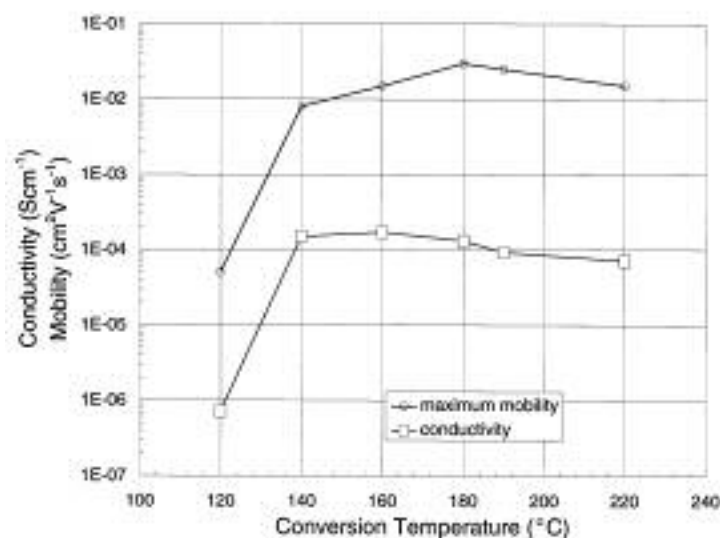


Fig. 4.3: Field-effect mobilities and conductivities as a function of conversion temperature for the precursor-route pentacene MISFET structures (From [5]).

Fig. 4.3 shows the resulting maximum mobility and conductivity as a function of conversion temperature. The measurement accuracy is about 15%. Surprisingly, a further improvement of the charge-carrier mobility in pentacene films is obtained by raising the conversion temperature from below 140 °C to higher temperatures. A maximum is reached at 180 °C. The slight decrease at higher temperatures is probably due to removal of impurities which act as a dopant [5]. Apart from an improved molecular order of the films (higher density of microcrystallites) as seen from microscope images [11], it is shown in this work that the higher charge-carrier mobility may be related to an increased conversion ratio of the precursor with increasing conversion temperature.

In section 4.3, the results of *in-situ*  $\mu$ PIXE measurements on these devices are presented. The purpose is to determine the precursor-to-pentacene conversion ratio as a function of conversion temperature, from the measured amount of chlorine in the MISFETs after conversion, relative to the measurement before conversion.

### 4.3 Precursor-route pentacene MISFET measurements

Six pentacene MISFET structures (one unconverted structure and five of the converted structures of which the electrical properties were measured) were mounted in the Eindhoven scanning ion microprobe set-up for  $\mu$ PIXE analysis of the amount of (residual) chlorine.

A 3 MeV proton beam ( $\sim 120$  pA) was focussed to a beam spot of about  $5 \times 4 \mu\text{m}^2$  FWHM that could be scanned across the sample. For PIXE analysis, a Si(Li) X-ray detector was used at a backward angle of 135 degrees. Additionally, for NBS analysis, a charged-particle detector was used at a backward angle of 147 degrees.

The detection of chlorine X-rays (2.622 keV) from the residual precursor is likely to be hindered by the large amount of silicon X-rays (1.740 keV) from the silicon wafer, unless special care is taken. Therefore, an absorber was placed in front of the X-ray detector, to specifically suppress Si X-rays, without affecting the Cl X-rays too much.

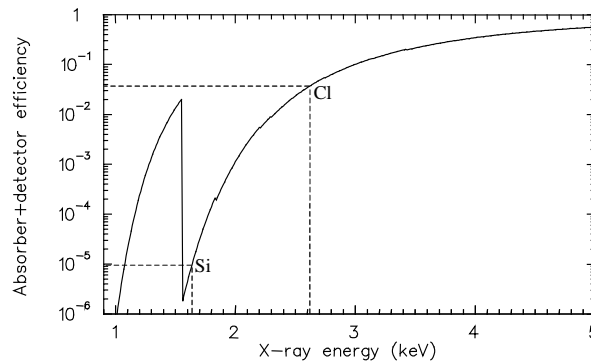


Fig. 4.4: Detection efficiency of the Si(Li) X-ray detector with an absorber of 100  $\mu\text{m}$  beryllium and 8  $\mu\text{m}$  aluminum. See text for details.

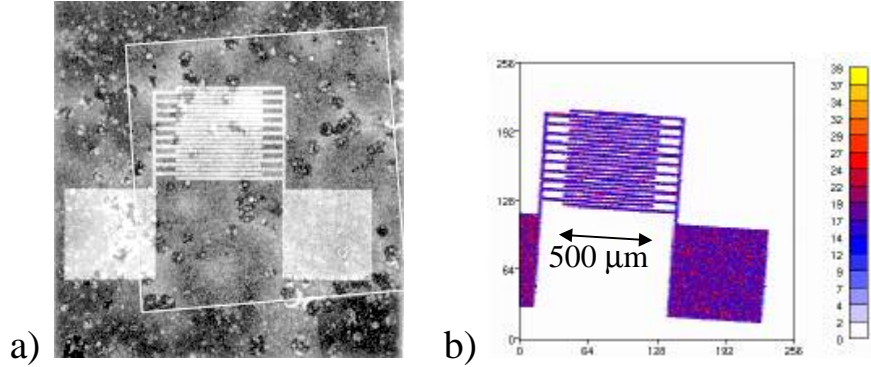


Fig 4.5: a) optical microscopy image of the pentacene-precursor FET structure, after the PIXE measurement. b) The PIXE yield-distribution for the Au X-rays (see text for details).

A combination of 100  $\mu\text{m}$  beryllium and 8  $\mu\text{m}$  aluminum appeared to be successful. In Fig. 4.4, the calculated [16] detection efficiency  $\epsilon T$  of the Si(Li) X-ray detector with the additional absorber is plotted, as a function of the X-ray energy. The detection of chlorine X-rays ( $\epsilon T \approx 6 \cdot 10^{-5}$ ) is over 600 times more effective than that of silicon X-rays ( $\epsilon T \approx 4 \cdot 10^{-2}$ ). Without the absorber, the efficiency for Si and Cl would be the same within 5%.

In Fig. 4.5a, an optical microscopy image of the pentacene-precursor FET structure after the PIXE-measurement is shown. The patterned source-drain structure is clearly visible. The large, slightly tilted area of about  $1.4 \times 1.4 \text{ mm}^2$  across which the ion beam was scanned is highlighted for clarity. In Fig 4.5b, the PIXE yield distribution for the gold X-rays in this scanned area is plotted. Again, the patterned Au source-drain structure is clearly visible.

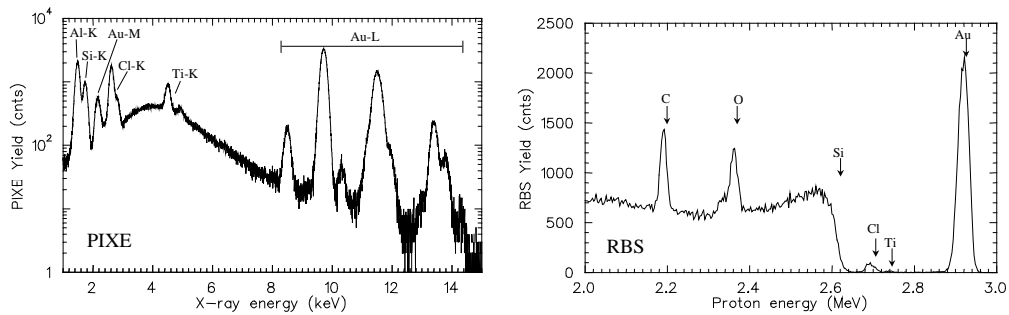


Fig. 4.6: The PIXE and NBS energy histograms, measured on the pentacene-precursor FET.

Fig. 4.6 displays the energy histograms for the simultaneous PIXE and NBS measurement on the (unconverted) pentacene-precursor FET, summed over all positions. In the PIXE histogram, X-ray lines from gold and titanium (patterned source-drain structure), chlorine (precursor), silicon (wafer) and aluminum (secondary X-rays from absorber) are detected above the continuous background. In the NBS histogram, peaks from gold, titanium, and chlorine are visible, which lie well above the silicon ridge. Also visible in the NBS histogram

are peaks from oxygen (insulating layer) and carbon (organic film), on top of the continuous silicon ridge.

The amount of chlorine in the sample is determined from the Cl-K X-ray peak content. A measure for the applied ion dose is obtained from the Si-K X-ray peak content. A measure for the organic film thickness is obtained from the NBS carbon peak content. Using these, a relative quantification of the chlorine in the samples can be performed.

From the measurement on the unconverted precursor, during which an ion dose of about 1.2  $\mu\text{C}$  was applied, a carbon to chlorine atomic ratio of  $6 \pm 1$  is found. In the precursor molecule, the C/Cl ratio equals 7. Furthermore, a chlorine loss of about 5% is observed during the measurement, which, however, would decrease the measured chlorine to carbon ratio. An absolute error in, for example, the absorber transmission may explain the difference between the two ratios.

For each of the six samples, the beam spot was scanned across the sample in a square pattern of  $32 \times 32$  points, each  $5.6 \mu\text{m}$  apart. The area was chosen such that it overlapped the source-drain structure of the FET, since it is this area that determines the electrical properties of the FET. A total ion dose of about 400 nC was applied to each sample, and areal doses were about 20 times higher than for the large area scan. Differences in dose between the samples were corrected for by normalization on the silicon PIXE yield. From this, a global decrease of the chlorine-to-silicon yield ratio with increasing conversion temperature is found.

From the NBS data, a variation in the normalized carbon yield of about  $\pm 35\%$  between the different samples is found. No significant loss of carbon with ion dose was observed. Furthermore, no trend of the normalized carbon yield with conversion temperature was found, although some carbon loss during conversion is expected. Therefore, the measured variations in carbon areal density reflect actual differences in the thickness of the organic film of the various samples, due to variations in the spin-coating process.

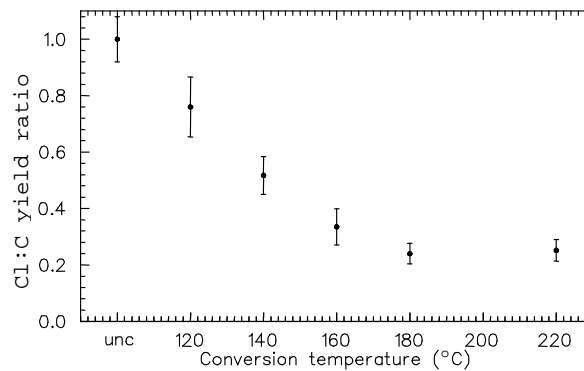


Fig. 4.7: The measured chlorine-to-carbon yield ratio, relative to the ratio for the unconverted sample, as a function of conversion temperature. (See text for details).

The corrections for the observed film-thickness variations have been carried out for the data presented in Fig. 4.7, where the ratio of the chlorine-to-carbon yield is plotted as a function of the conversion temperature, relative to the ratio for the unconverted sample. This chlorine-to-carbon yield ratio is a measure for the elimination of the Cl-containing precursor leaving group that is released upon conversion. A smooth decrease of the chlorine-to-carbon yield ratio with increasing conversion temperature is found, stabilizing above 160 °C.

Apparently, below 160 °C, the elimination of the tetrachlorobenzene leaving group from the devices is incomplete. This is similar to the result of Thermal Gravimetric Analysis (TGA) measurements on the pentacene precursor, from which it was found [11] that elimination of the tetrachlorobenzene leaving group is incomplete below 140 °C.

For conversion temperatures above 160 °C, the  $\mu$ PIXE measurements, which have been performed on actual devices, show a chlorine-to-carbon yield ratio of  $0.24 \pm 0.04$ . Obviously the precursor conversion and/or subsequent elimination of the tetrachlorobenzene leaving group is still incomplete at these higher temperatures.

The measurement is, however, not corrected for chlorine loss during ion-beam irradiation. It is estimated from the list-mode data that for the unconverted sample more than 20% of the chlorine is lost during ion beam irradiation, whereas for the samples converted at 160 °C and above this is only about 5%. Thus, the chlorine-to-carbon yield ratio for higher conversion temperatures will be up to 4 times lower than measured. Furthermore, the amount of carbon, measured on the converted samples is somewhat lower than on the unconverted sample. A correction for this also results in a slightly lower chlorine-to-carbon yield ratio at higher temperatures. Before these corrections can be applied, more accurate measurements of the chlorine and carbon loss with ion dose are required.

The  $\mu$ PIXE experiment clearly shows a relation between the chlorine-to-carbon yield ratio (Fig. 4.7) and the charge-carrier mobility (Fig. 4.3) measured in an operational device. Incomplete precursor conversion and incomplete elimination of tetrachlorobenzene leaving groups hinder the crystalline packing of the oligomers and limit the through-conjugation along the oligomer. The degree of ordering and conjugation within the pentacene layer thus is not optimal which apparently affects charge-carrier mobility.

## 4.4 Organic electroluminescent diodes

The electroluminescent properties of conjugated polymers, in addition to their semiconducting properties, have led to the development of organic light-emitting diodes (LEDs) [2,4]. Electroluminescence occurs if electrons and holes, injected via electrodes, recombine and subsequently decay radiatively [2].

In Fig. 4.8, the structure of a polymer electroluminescent diode is depicted. Glass coated with a thin (~150 nm) optically transparent and electrically conducting layer of indium-tin oxide (ITO) is used as substrate and hole-injecting electrode. The semiconducting active layer of poly(*p*-phenylene vinylene), PPV, is processed onto the ITO electrode from a solution.

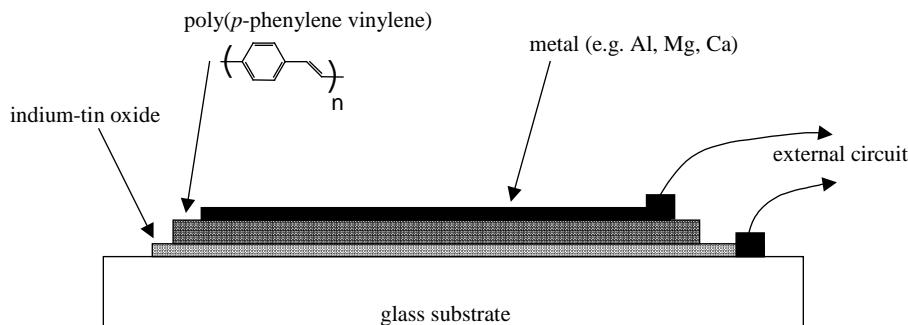


Fig. 4.8: Structure of a polymer electroluminescent diode.

Since PPV itself is insoluble, two strategies are widely used to resolve this [12]. One way is to use a soluble precursor polymer of PPV, that can be spin-coated from the solution into a thin film ( $\sim 100$  nm) and, via a subsequent (thermal) treatment, converted into the fully conjugated PPV. Alternatively, alkoxy side-groups can be attached to the PPV polymer chain, which makes it directly processable from the solution. These side-groups can be used also to tune the optical and semiconducting properties of the polymer.

A metal with a low work function (*e.g.* aluminum, magnesium, or calcium) is then thermally evaporated onto the organic layer to form the electron-injecting top-electrode.

Requirements for an organic LED to become (commercially) attractive are a high light-output at low-voltage operation combined with a long lifetime. The present electroluminescence efficiency of a few percent has to be increased further, which requires optimization of the charge-injection at the electrode/polymer interface and the charge transport within the polymer. It is not only the proper choice of electrode and polymer that is important, but also the control of possible interface degradation and oxidation of the polymer during device operation.

Electrode corrosion during LED operation can result in unintentional chemical doping of the polymer and may cause barriers to charge-carrier injection. These processes, however, can also occur already during device preparation, as shown in this work.

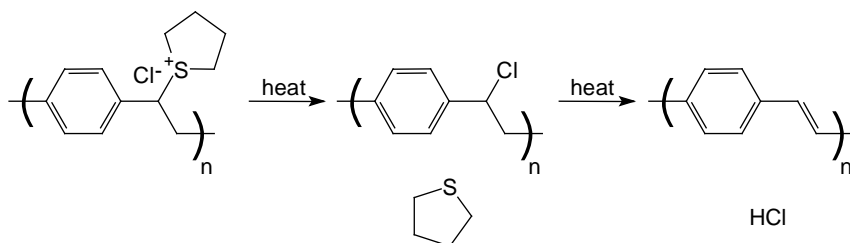


Fig. 4.9: Chloride sulfonium salt precursor polymer converts to PPV by heat treatment. Tetrahydrothiophene and hydrochloric acid are to be eliminated [12].



A commonly used precursor route to PPV is shown in Fig. 4.9. [12]. A sulfonium salt precursor polymer with a chlorine counter-ion is converted by thermal heating ( $\sim 200$  °C,  $\sim 10$  hours) under vacuum or nitrogen. During conversion, the tetrahydrothiophene (THT) leaving group is released. In addition, hydrochloric acid is released, either via an intermediate substitution of the sulfonium group by the chlorine ion, or simultaneously with the THT.

Alternatively, the sulfonium leaving group can be replaced by a methoxy leaving group. The resulting methoxy-substituted precursor polymer is more stable than the sulfonium salt precursor polymer, and it can be converted into the fully converted PPV by heating under acid catalysis, for which often an hydrochloric acid atmosphere is used.

It has been reported [13] that this hydrochloric acid, either released as a conversion product or used as an acid catalyst, can cause corrosion of the ITO electrode and formation of indium chloride, which can dope the PPV. In section 4.5,  $\mu$ PIXE measurements on PPV/ITO samples, exposed to a hydrochloric acid atmosphere, will be presented, that show the formation of  $\text{InCl}_3$  islands with a diameter of about  $50\text{ }\mu\text{m}$  across the film.

## 4.5 $\text{InCl}_3$ formation in ITO/PPV structures

Structures of an ITO coated glass substrate, covered with a spin-coated layer of PPV, were obtained from Philips Research. Instead of a precursor-route PPV, a soluble PPV derivative with alkoxy side-groups was used, that does not require a conversion treatment. The samples were exposed to an acid atmosphere, by leading an argon flow through a solution of hydrochloric acid and subsequently over the samples, at room temperature. This was done for 90 h, 10 minutes and  $\sim 1$  minute, for the respective samples. One sample was left untreated.

Next, using a 3M Scotch tape, containing carbon and hydrogen only, the PPV layers were peeled off the ITO coated substrate. The tape films, with the PPV layer stuck to it, were mounted in the scanning ion microprobe set-up.

A 3 MeV proton beam was focussed to a beam spot of about  $5 \times 4\text{ }\mu\text{m}^2$ . The beam current was about 25 pA. The beam spot was scanned across the sample in a square area of  $360 \times 360\text{ }\mu\text{m}^2$ . A Si(Li) X-ray detector with an additional absorber consisting of  $100\text{ }\mu\text{m}$  beryllium and  $8\text{ }\mu\text{m}$  aluminum (see Fig. 4.4) was used for PIXE analysis. Simultaneously, a charged-particle detector was used for NBS analysis.

For the PPV/tape sample that was not treated with HCl, no traces of elements other than hydrogen, carbon, and oxygen could be detected in an extensive PIXE measurement. From the latter experiment it can be concluded that both the PPV and the tape are very clean, with trace-element contamination below the detection limit ( $<10^{15}\text{ at/cm}^2$ ) of this and subsequent measurements. Apparently, the peeling method using the tape does not remove indium or tin from the ITO layer.

For the PPV/tape sample that was exposed to HCl for 90h, significant amounts of chlorine and indium were measured.

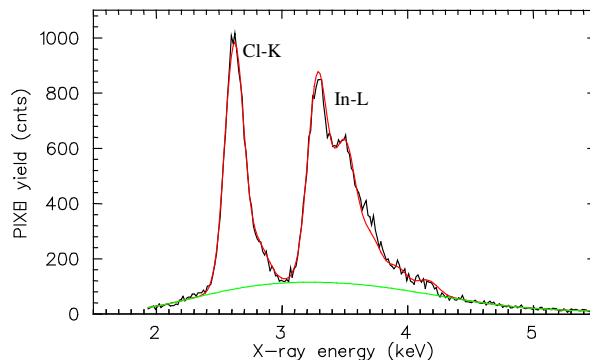


Fig 4.9: PIXE energy histogram of the PPV/tape sample, after 90h HCl treatment of the ITO/PPV structure. The peak+background fit for the Cl-K and the In-L X-rays is included.

In Fig. 4.9, the PIXE energy histogram of this measurement is plotted. From a peak+background fit, the peak content of the chlorine K-X-rays and the indium L-X-rays can be determined. Using the corresponding X-ray production cross-sections and the absorber+detector efficiency, a chlorine-to-indium atomic ratio of  $(3.2 \pm 0.5)$  is found. This indicates the presence of  $\text{InCl}_3$  in the PPV/tape sample. This is confirmed by a measurement on a reference sample of  $\text{InCl}_3$  salt, which also yielded a chlorine-to-indium ratio of about three, both with and without the absorber, as expected.

Fig. 4.10 shows the distribution of the chlorine and indium yield across the sample. From these distributions, a strong correlation between the presence of chlorine and indium is found. Furthermore, the indium chloride is confined to small islands with a diameter of about  $50 \mu\text{m}$ . For the sample that was given a less excessive treatment ( $\sim 10$  minutes) with HCl, again  $\text{InCl}_3$  islands were observed. After an HCl exposure of just 1 minute, no indium or chlorine was observed.

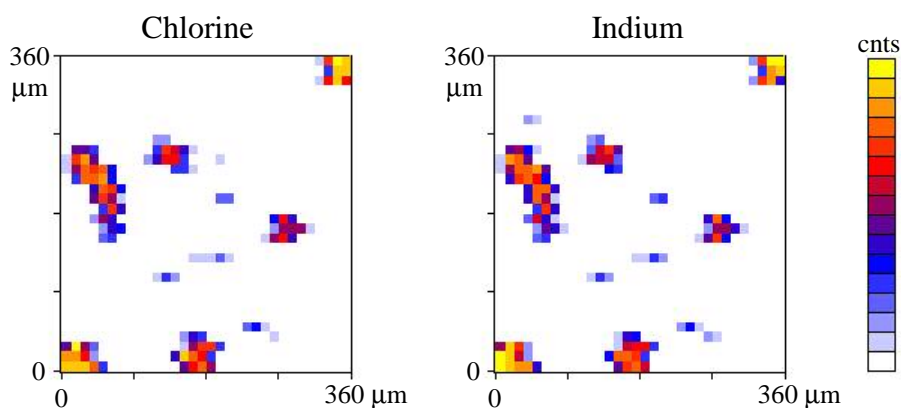


Fig 4.10: PIXE yield distribution for chlorine and indium.

Although the treatment of ITO/PPV samples with hydrochloric acid may seem excessive, precursor-route PPV layers are converted at  $\sim 200$  °C during 10 hours or more, sometimes in an acid atmosphere. In this work, these conditions have been simulated, by exposing the devices to HCl at room temperature. Both after 90 hours and just 10 minutes of exposure, the formation of indium chloride islands was observed. The chemical structure is  $\text{InCl}_3$  and the typical dimension of the islands is 50  $\mu\text{m}$ . This is consistent with reported secondary ion mass spectrometry [14] and scanning electron microscopy [13] measurements.

Apparently, electrode degradation occurs through the etching of the ITO by HCl. From these  $\mu$ PIXE measurements it is not clear whether the indium-chloride resides at the surface of the peeled PPV layer or has migrated into the PPV layer. The latter may result in unintentional chemical doping of the polymer and in barriers to charge-carrier injection, which worsens device performance [13,14]. RBS measurements at our laboratory [15] on similar devices have revealed a homogeneous indium-distribution throughout the PPV layer. This suggests that migration of indium from the ITO into the PPV layer can occur.

## 4.6 Conclusions

The  $\mu$ PIXE technique has been applied in two organic semiconductor device-related studies in which both a sensitivity to minor and trace elements and a lateral position resolution at micrometer scale are required.

First, for precursor-route pentacene field-effect transistors, the residual amount of chlorine was measured as a function of conversion temperature, relative to the amount of chlorine in an unconverted device. From this, the efficiency of precursor conversion and leaving-group elimination is estimated. These measurements were performed *in-situ* on the source-drain structures of the FET devices, which allows for a direct comparison of the electrical device characterization and the  $\mu$ PIXE measurement results. A decrease in the amount of chlorine with increasing conversion temperature was found, stabilizing above 160 °C, at about 24% of the amount of chlorine in the precursor. This corresponds to an elimination of chlorine upon conversion of roughly  $(76 \pm 4)\%$ . The error in this result is largely determined by the inaccuracy of the film thickness measurement. Due to the chlorine loss during ion beam irradiation, which could only be estimated, the result is underestimated.

Nevertheless, it can be concluded from these measurements that the charge-carrier mobility is related to the efficiency of precursor conversion and leaving-group elimination. In case of incomplete elimination of the leaving groups, the corresponding residual side chains can hinder the crystalline packing of the oligomers. Also the conjugation path along the oligomer remains broken in case of incomplete conversion. The degree of ordering and conjugation within the pentacene layer is not optimal in that case, which apparently affects the charge-carrier mobility.

Second, for polymer electroluminescent diode structures, degradation of the ITO electrode by hydrochloric acid, which is both released as a conversion product and used as an acid catalyst,

during precursor conversion, has been demonstrated. For PPV/ITO samples, which were exposed to an hydrochloric atmosphere at room temperature, to simulate actual precursor-PPV conversion conditions, the formation of indium-chloride islands across the polymer layer was measured using  $\mu$ PIXE. This was observed after 90 hours of HCl exposure, but also already after 10 minutes. Furthermore, the chemical structure of the indium-chloride was found to be  $\text{InCl}_3$ , and the typical lateral dimension of the regions is 50  $\mu\text{m}$ .

Apparently, electrode degradation occurs through the etching of the ITO by HCl. From these  $\mu$ PIXE measurements it is not clear whether the indium-chloride resides at the surface of the peeled PPV layer or has migrated into the PPV layer. The latter may result in unintentional chemical doping of the polymer and in barriers to charge-carrier injection, which worsens device performance [13,14]. RBS measurements at our laboratory [15] on similar devices have revealed a homogeneous indium-distribution throughout the PPV layer. This suggests that migration of indium from the ITO into the PPV layer can occur.

In conclusion, in this work it is demonstrated that the  $\mu$ PIXE technique can be successful in the study of organic semiconductor device-related effects.

## References

- [1] C.K. Chiang *et al.*, Phys. Rev. Lett. 39 (1977) 1098.
- [2] Handbook of conducting polymers, (M. Dekker Inc., New York, 1998), Ch. 13, 19.
- [3] D.M. de Leeuw, E.J. Lous, Synth. Metals 65 (1994) 45-53.
- [4] J.H. Burroughes, D.D.C. Bradley, A.R. Brown, R.N Marks, K. Mackay, R.H. Friend, P.L. Burn, A.B. Holmes, Nature 347 (1990) 539.
- [5] A.R. Brown, C.P. Jarrett, D.M de Leeuw, M. Matters, Synth. Metals, 88 (1997) 37.
- [6] H. Fuchigami, A. Tsumura, and H. Koezuka, Appl. Phys. Lett. 63 (1993) 1372-1374.
- [7] J.J.M. Halls, C.A. Walsh, N.C. Greenham, E.A. Marseglia, R.H. Friend, S.C. Moratti, A.B. Holmes, Nature 376 (1995) 498.
- [8] Philips Research, press release 97005e.
- [9] A.R. Brown, D.M. de Leeuw, E.E. Havinga, A. Pomp, Synth. Metals, 68 (1994) 65.
- [10] P. Herwig, (Dissertation, University of Mainz, 1993).
- [11] A.R. Brown, private communication.
- [12] P.L. Burn *et al.*, J. of the Am. Chem. Soc. 115 (1993) 10117-24.
- [13] M. Herold, J. Gmeiner, C. Drummer, M. Schwoerer, J. of Mat. Sci. 32 (1997) 5709-5915.
- [14] G. Sauer *et al.*, J. Anal. Chem. 353 (1995) 642.
- [15] M.P. de Jong, D.P.L. Simons, M.A. Reijme, L.J. van IJzendoorn, A.W. Denier van der Gon, M.J.A. de Voigt, H.H. Brongersma, R.W. Gymer, submitted to Synth. Metals.
- [16] F. Munnik, Accuracy Evaluation of Absolute Calibration in Thick-Target PIXE, (Ph.D. Dissertation, Eindhoven University of Technology, 1994).

## Chapter 5

# $\mu$ PIXE study of diffusion processes during patterned photo-polymerization

*The lithographic and holographic illumination of an isotropic mono-acrylate and a liquid-crystalline di-acrylate blend is known to give polymer films with a lateral modulation [1] in refractive index, which is of interest for use in optical systems.*

*In this chapter, it is demonstrated that the  $\mu$ PIXE technique provides the means to quantitatively study lateral diffusion processes in such mixtures of monomers during patterned photo-polymerization. By labeling of one of the acrylate monomers with an element that can be detected with PIXE, the final monomer distribution in the films can be revealed. Chemical composition modulations across the film are found and the alleged two-way monomer diffusion [1] is confirmed. Furthermore, measurements are presented on a new, dual-labeled monomer system, which allows for detection of both monomers and full quantification of the monomer distribution.*

This work was done in collaboration with Dirk Broer and René van Nostrum, affiliated to Philips Research Laboratories and to the department of chemistry at Eindhoven University of Technology.

## 5.1 Introduction

Organic, polymeric materials have received enormous interest for their use in optical systems for data transport, storage, and display [2]. A lot of effort is put into the development of *specialty* polymers, to improve the performance of these optical systems. The molecular structure is carefully designed, together with the molecular ordering, since these two determine the interaction of the resulting optical system with the incoming light. The ordering of the molecular structure can be controlled via both the monomer type and via the polymerization process.

Self-ordering of the molecular structure can be obtained if a monomer is selected with, for example, liquid-crystalline properties or with a cholesteric component. The molecules can then be aligned in a parallel (nematic) way or in a helical shape. These systems can be used as reflective filters that are polarization-selective and/or wavelength-selective [2].

Ordering of the molecular structure can also be induced via the polymerization process. In a typical photo-polymerization, the liquid mixture of monomers and a photo-initiator are irradiated with UV-light, which dissociates the photo-initiator molecules into radicals. These radicals subsequently initiate chain-addition polymerization reactions of the monomers, which are (cross-)linked into a polymer structure. Ordering of the molecules in this structure can, amongst others, be obtained via diffusion processes during the photo-polymerization. Diffusion of monomers can be induced by varying the UV-light intensity (either across the film in a pattern by lithography or holography, or throughout the film by UV absorption) [6]. Since the monomer depletion is related to the UV intensity, monomer-concentration gradients will arise, which induce monomer diffusion to the illuminated areas. In this way, modulations in density and refractive index can be obtained [6].

If two types of monomer with a different photo-reactivity are used, two-way diffusion may occur, where the monomers diffuse in opposite directions. In that case, in addition to a density modulation, a modulation in the chemical composition can be obtained [7] and hence a modulation in, for example, phase (isotropic or ordered) or chirality. The scale at which ordering is induced may vary from the micrometer-scale down to the nanometer-scale. By combining self-ordering and induced-ordering effects, polarizing holographic and lithographic polarizing gratings [1] and broad-band reflective polarizers [2,3] have been produced.

In this work, it is shown that ion-beam analysis techniques, and more specifically the particle induced X-ray emission (PIXE) technique applied in a scanning ion microprobe, provide the opportunity to quantitatively study the density and chemical composition modulations in these organic optical systems. In collaboration with D.J. Broer and C.F. van Nostrum, their system of polarizing gratings [1], which is described in more detail in section 5.2, has been investigated. The objective is to quantify the supposed two-way diffusion processes during the patterned photo-polymerization of the monomer mixture. This mixture consists of both a liquid-crystalline and an isotropic monomer type, with different photo-reactivities. After labeling one of the monomer types with an element that can be detected with PIXE, in this case silicon, the final distribution of monomers, and hence the modulation in chemical

composition, can be measured. The experimental details and results are presented in section 5.3. In order to enable a more extensive study of the diffusion processes as a function of, *e.g.* temperature, light intensity, and dose, a new system with two photo-reactive monomers, one labeled with silicon and the other with chlorine, was used to prepare new films. The results of measurements on this new system, described in section 5.4, show that this system allows to discriminate between diffusion of both types of monomers. General conclusions and recommendations are given in section 5.6.

## 5.2 Photo-induced diffusion processes

Two-way diffusion effects, induced by patterned photo-polymerization in mixtures of monomers with different photo-reactivities, were first reported by Tomlinson *et al.* [7]. Van Nostrum *et al.* [1] showed the manufacturing of polarizing gratings using the patterned (lithographic or holographic) photo-polymerization of a mixture that consists of an isotropic monomer and a liquid-crystalline monomer. These gratings consist of alternating isotropic areas, with a low refractive index  $n_i$ , and optically oriented, nematic areas. The latter areas are bi-refringent and, if their low refractive index  $n_{0,low}$  is matched to  $n_i$ , diffraction will only occur for the incident light that is polarized parallel to the polymer orientation of the nematic areas.

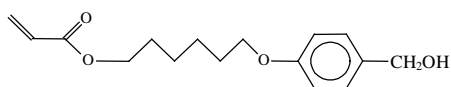


Fig. 5.1a: The isotropic monofunctional acrylate monomer  
(**mMA**, 6-[4-(hydroxymethyl)phenoxy]hexyl acrylate,  
 $H_{22}C_{16}O_4$ ,  $M=278$ ).

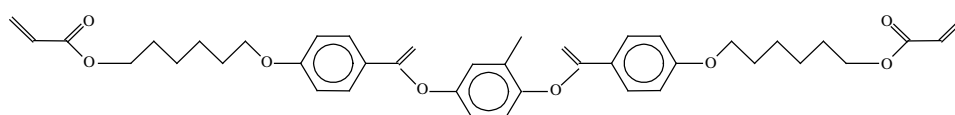


Fig. 5.1b: The liquid-crystalline difunctional acrylate monomer  
(**mDA**, 2-methyl-1,4-bis[4-[6-(acryloyloxy)hexyloxy]benzoyloxy]benzene,  
 $H_{44}C_{39}O_{10}$ ,  $M=672$ ).

The isotropic mono-acrylate monomer (**mMA**) and the liquid-crystalline di-acrylate monomer (**mDA**) are schematically shown in Fig. 5.1. The **mDA** has a higher photo-reactivity than the **mMA**, partially because of the double number of functional (acrylate) groups and partially because of the Trommsdorf effect (auto-acceleration, or gel effect) [5] which is common for cross-linking monomers.

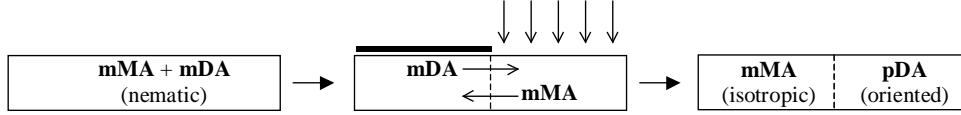


Fig. 5.2: The diffusion process during patterned photo-polymerization of a mixture of monofunctional acrylate monomer (**mMA**) and difunctional acrylate monomer (**mDA**) into the polymers **pMA** and **pDA**.

The gratings have been produced in a thin film between two closely-spaced glass plates consisting of a mixture of **mMA** and **mDA**. The ratio **mMA**:**mDA** is 30:70, such that the blend is in its nematic phase. A schematic representation of the supposed polymerization and diffusion process is shown in Fig. 5.2.

In the illuminated areas, the **mDA** is depleted faster than the **mMA**, and concentration gradients are induced. As a result, the **mDA** diffuses to the illuminated areas, and the **mMA** diffuses oppositely to the dark areas. The enrichment of isotropic **mMA** can enforce a phase transition in the dark areas from the nematic to the isotropic phase. The patterned film can be fixed with a uniform illumination, such that a thin film grating is obtained with alternating oriented and isotropic areas.

Van Nostrum *et al.* [1] report on fluorescent labeling microscopy experiments on these films. It was found that the amount of MA, as measured via the fluorescence intensity, was higher in the dark areas than in the surrounding illuminated areas. This is a strong indication for the occurrence of two-way diffusion of **mMA** and **mDA**, as described above.

Furthermore, van Nostrum *et al.* [1] have described this process by an elementary model, in which the diffusion rates are high compared to the polymerization rates. In this model it is assumed that no net material transport occurs across the film, *i.e.* that the number of monomer units (free or in polymerized form) per volume unit is constant across the grating. Furthermore, it is assumed that only the free monomers can diffuse, and that they are not hindered by the surrounding polymer that is being formed. Also, the polymerization rates are assumed independent of the light intensity.

The model of van Nostrum was used (Fig. 5.3) to calculate the two-way diffusion processes with a rectangular intensity profile, to simulate lithography using a grating mask, and with a sinusoidal intensity profile, to simulate holography using a split laser-beam interferometer. The calculation is stopped at 98% conversion. The **mDA** polymerization rate is taken twice as high as that of **mMA**. For the rectangular intensity profile, a rectangular concentration profile results for the total MA-fraction ( $=\text{mMA}+\text{pMA}$ ). Compared to its initial value (30 mol%), the MA-fraction has decreased in the illuminated areas to ~20 mol% and increased in the dark areas to ~40 mol%. The opposite result is obtained for the DA-fraction. For the sinusoidal intensity profile, an asymmetric concentration profile results for the total MA-fraction, with an increase of MA in the dark areas that is higher and narrower than the decrease of MA in the illuminated areas.



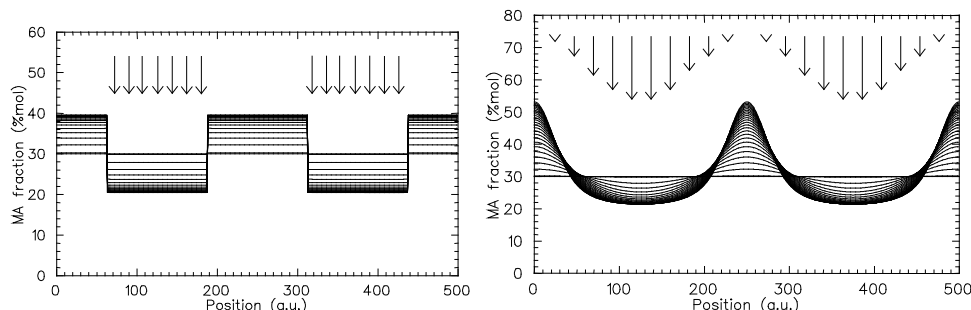


Fig. 5.3: Simulation of the diffusion process during lithographic (left) and holographic (right) photo-polymerization, as a function of illumination time, using the van Nostrum model.

See text for details.

The objective of this work is to confirm the presumed two-way diffusion processes, with the Particle Induced X-ray Emission technique in a scanning ion microprobe ( $\mu$ PIXE). This is done by labeling of the mono-acrylate monomers with a silicon-containing end-group that can be detected by PIXE. Also, with  $\mu$ PIXE it is possible to test the quantitative characteristics of the diffusion model proposed by van Nostrum.

### 5.3 $\mu$ PIXE analysis of photo-induced diffusion

#### 5.3.1 Sample preparation

The films required for PIXE analysis were polymerized from a monomer mixture consisting of 70 mol% of **mDA**, as shown in Fig. 5.1b and of 30 mol% of **mSiMA**, which is shown in Fig. 5.4. The experimental conditions were chosen similar to those in [1] assuming a similarity of the diffusion properties as well as the photo-reactivities of the labeled **mSiMA** and the unlabeled **mMA**.

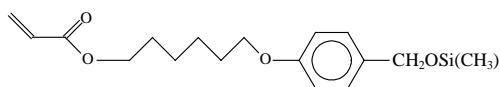


Fig. 5.4: The modified, silicon-labeled monofunctional acrylate monomer (**mSiMA**, 6-[4-(trimethylsiloxymethyl)phenyloxy]hexyl acrylate,  $H_{30}C_{19}O_4Si$ ,  $M=350$ )

Sample cells, formed by two glass plates separated by 6  $\mu$ m silica spheres, were filled by capillary suction with the initial liquid, low-viscosity monomer mixture. Films were prepared by van Nostrum via holographic photo-polymerization using an interference pattern of his split laserbeam interferometer with a 10  $\mu$ m grating constant. Holographic illumination was carried out with an Ar laser (351 nm, 1.1 mW/cm<sup>2</sup>), at various temperatures (55-80 °C), for a duration of 5 min.

### 5.3.2 $\mu$ PIXE experiments

After removal of the glass plates, a few of the thin, brittle, and free-standing films were successfully mounted in the target wheel of the Eindhoven scanning ion microprobe set-up. A 3 MeV proton beam (current of 40 pA) was focussed into a spot with a diameter of about  $4 \times 4 \mu\text{m}^2$  FWHM (Full Width at Half Maximum). This beam spot was scanned across the sample in a square pattern of  $32 \times 32$  points, each  $1.4 \mu\text{m}$  apart. The total scanned area therefore measures about  $45 \times 45 \mu\text{m}^2$ . The protons hit the sample perpendicularly.

$\mu$ PIXE analyses were performed using our Si(Li) X-ray detector, at a backward angle of 135 degrees, without an additional absorber (detector solid angle =  $40.9 \pm 0.4$  msr). Simultaneously, nuclear (non-Rutherford) forward and backscattering spectrometry (NFS/NBS) was applied to detect bulk elements, like hydrogen, carbon, and oxygen, using charged-particle detectors at a forward angle (45 degrees,  $8.3 \pm 0.3$  msr) and a backward angle (147 degrees,  $9 \pm 2$  msr). A total ion dose of 530 nC was applied, equally distributed over all irradiated points.

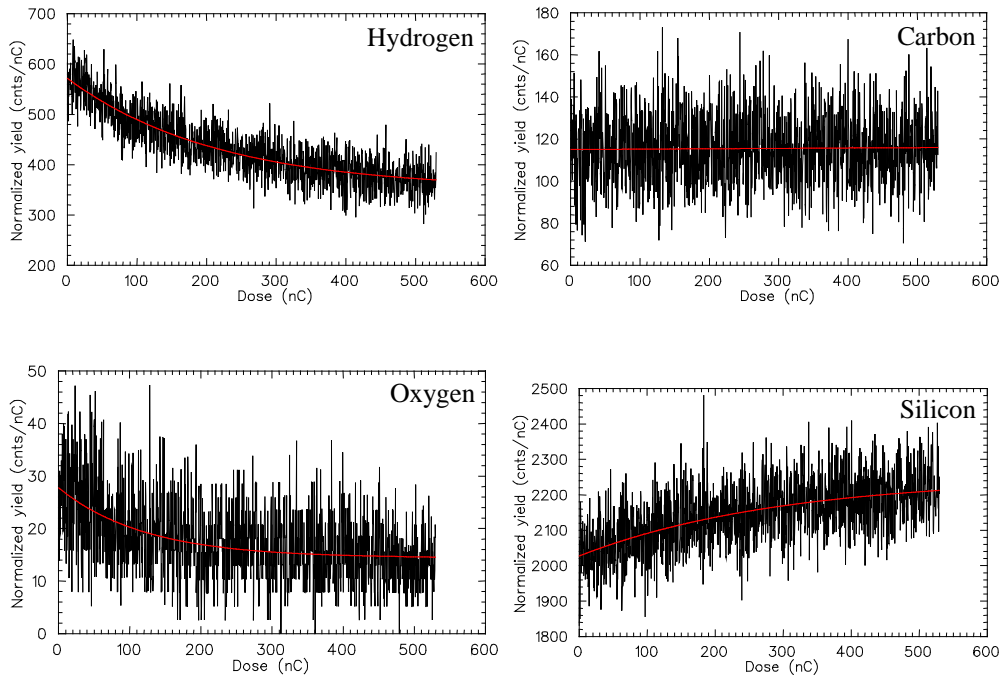


*Fig. 5.5: The NBS/NFS normalized yield for hydrogen, carbon, and oxygen, and the PIXE normalized yield for silicon, as a function of ion dose, summed over all 1024 scan positions. From an exponential fit, it is found that the hydrogen signal decreases by 35% and that the oxygen signal decreases by 48%. The carbon signal shows no change. The silicon signal increases by 9%.*

Fig. 5.5 shows the measured NBS/NFS normalized yield for hydrogen, carbon, and oxygen, as a function of ion dose, summed over all irradiated positions. It is found that, due to radiation damage, the hydrogen and oxygen signals decrease. Exponential fits have been applied to determine the amount of element loss.

The areal densities of the hydrogen, carbon, and oxygen signal do not show any variations over the scanned area of  $45 \times 45 \mu\text{m}^2$ , except for statistical fluctuations of about 10%. This is confirmed by subsequent Scanning Transmission Ion Microscopy (STIM) measurements on the same sample, which show that variations in bulk areal density (H+C+O) are less than 5%. This is also in agreement with the AFM measurements of van Nostrum [1]. Therefore, the sample is treated as a homogeneous film, and the loss of hydrogen and oxygen was assumed to be similar for each irradiated point.

The exponential fits from Fig. 5.5 have been used to correct the integrated hydrogen and oxygen yield of each measured point for radiation damage and to determine the zero-dose bulk (H+C+O) composition of the sample. An atomic ratio of H:C:O  $\approx$  4:4:1 was found, which is not in full accordance with the ratio of H:C:O = 4.8:4:1 as calculated from the **mDA** and **mSiMA** chemical structure and the mixing ratio. A bulk areal density of  $(0.76 \pm 0.09) \text{ mg/cm}^2$  was found. For a typical density of  $1 \text{ g/cm}^3$  this corresponds to a film thickness of 7-8  $\mu\text{m}$ . After a dose of 530 nC, the bulk areal density has decreased to  $(0.66 \pm 0.09) \text{ mg/cm}^2$ .

Fig. 5.5 also shows the PIXE normalized yield for silicon as a function of ion dose, summed over all irradiated positions. It can be seen that the normalized silicon yield increases by about 9%. This measured increase can have two causes. First, the absorption of silicon X-rays within the sample decreases with ion dose, because of the decrease in areal density of hydrogen and oxygen. Second, the areal density of silicon may increase if the sample shrinks during irradiation with the ion beam.

The coefficient required to correct for the absorption of X-rays, the Matrix Correction Factor, or MCF, has been calculated using both the measured areal densities of hydrogen, carbon and oxygen and the X-ray absorption coefficients  $\mu$  for silicon X-rays in hydrogen, carbon, and oxygen. The X-ray absorption coefficients are listed in Table 5.1. The chlorine data is included for use in the next sections.

*Table 5.1: The absorption coefficients  $\mu$  for the silicon and chlorine X-rays in hydrogen, carbon, oxygen, silicon, and chlorine. Taken from the PANEUT [4] data-base.*

	$\mu_{\text{Si}} (\text{cm}^2/\text{g})$	$\mu_{\text{Cl}} (\text{cm}^2/\text{g})$
	$E_{\text{X-ray}} = 1.740 \text{ keV}$	$E_{\text{X-ray}} = 2.622 \text{ keV}$
H	5.317	1.845
C	470.4	127.7
O	990.1	304.9
Si	325.2	1314
Cl	635.9	197.9

From the measured bulk areal densities and the H:C:O ratio, the absorption coefficient  $\mu_{Si}$  for silicon X-rays in the film can be calculated. It is assumed that the contribution of the silicon atoms to  $\mu_{Si}$  can be neglected, since these atoms make up only 1-2 wt% of the film. For the initial, zero-dose atomic ratio of H:C:O $\approx$ 4:4:1 it is calculated that  $\mu_{Si} \approx 565 \text{ cm}^2/\text{g}$ .

Since the energy loss of the protons through stopping in these thin films can be neglected, Eq. 5.1 can be used to calculate the MCF, which is defined as the ratio of the X-ray yield without and with absorption of the X-rays in the sample:

$$MCF = \frac{\int_0^t dx}{\int_0^t e^{-\frac{\mu \rho x}{\cos(\theta)}} dx} = \frac{\frac{\mu \cdot \rho t}{\cos(\theta)}}{1 - \exp\left(-\frac{\mu \cdot \rho t}{\cos(\theta)}\right)} \quad (5.1)$$

The film thickness (cm) is represented by  $t$ , the bulk areal density ( $\text{g}/\text{cm}^2$ ) by  $\rho t$  and the angle at which the X-ray detector is positioned by  $\theta$  ( $=135$  degrees).

For the zero-dose bulk areal density of  $0.76 \text{ mg}/\text{cm}^2$ , it is found that the  $MCF_{Si} = 1.33$ . The MCF was also calculated as a function of dose, based on the bulk areal densities and H+C+O ratios from the fit results in Fig. 5.5. The MCF was taken to be the same for each irradiated position on the sample. After 530 nC, the  $MCF_{Si}$  has decreased to 1.27. Using the  $MCF_{Si}$  as a function of dose, the silicon normalized yield (Fig. 5.5) was corrected for X-ray absorption effects. Accordingly, the normalized yield, averaged over dose, increased by a factor 1.28. However, it was found that the normalized silicon yield still slightly increased with dose.

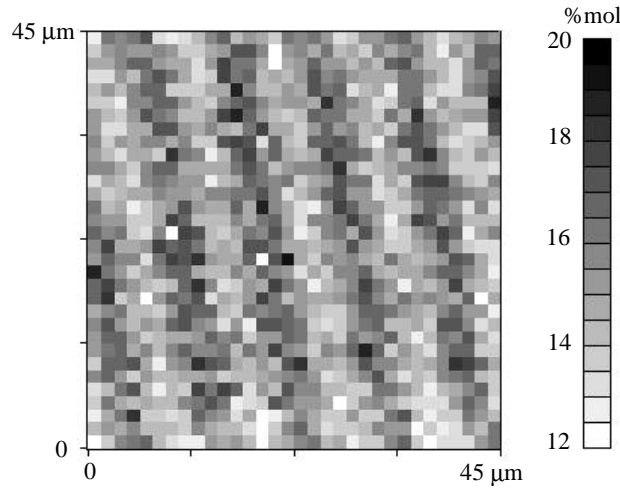


Fig. 5.6: The MA mol% distribution, as calculated from the measured silicon distribution, within the area scan across the sample.

Apart from an inaccuracy in the determination of the  $MCF_{Si}$ , this can be explained by sample contraction during the ion beam irradiation. Averaged over dose, a normalized yield was measured that is 1.5% higher than the zero-dose normalized yield. Therefore, a damage correction factor, defined as the ratio of the normalized yield in absence of degradation and the measured normalized yield integrated over dose, of 1/1.015 was applied.

Averaged over all scan positions, the silicon areal density is found to be  $1.2 \cdot 10^{17}$  at/cm<sup>2</sup>, or 0.2 at% Si, which is less than calculated from the structure formulas and monomer ratios. Assuming that each Si atom corresponds to one **mMA**, it can be calculated that the average Si concentration corresponds to a MA-fraction of about 17 mol%. The Si concentration has also been calculated for each individual scan position. The result is shown in Fig. 5.6. A distinct line pattern can be seen across the film, with a grating constant of 10  $\mu$ m that corresponds to that of the holographic interference pattern.

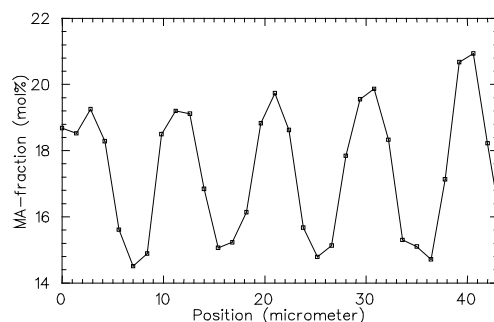


Fig. 5.7: The MA mol% distribution, as calculated from the measured silicon distribution along a line scan across the sample.

To improve statistics, a line-scan was made alongside the square scan area. From the NBS/NFS measurement of hydrogen, carbon, and oxygen, it appears that the bulk areal density of the sample is a 1-3% higher in the illuminated areas (where less silicon is measured) than in the dark areas. These density changes are induced by the patterned photo-polymerization, as will be discussed further in section 5.5.

PIXE analysis of the line-scan data, similar to the area-scan data above, gives the MA-fraction across the sample, as shown in Fig. 5.7. The variations in the silicon signal, and hence in the MA-fraction, are significantly larger than the variations in the bulk areal density. Variations in the MA-fraction of over 10 % are measured, compared to variations in the areal density of only 1-3 %. Since the increase of the MA-fraction was measured in the dark, non-illuminated areas, this measurement clearly confirms the supposed diffusion of **mMA** opposite to that of **mDA**.

Line-scan measurements that were performed on areas of the sample that were polymerized at other temperatures, showed similar MA-fraction profiles. No significant differences in shape and amplitude between these profiles were found.

### 5.3.3 Interpretation of the results

Fig. 5.7 showed a rather symmetric MA-fraction profile, with an average MA-fraction of 17.5 mol%. Fig. 5.8 shows the result of the simulation using the van Nostrum model, using an initial MA-fraction of 17.5 mol%, a reactivity ratio  $r_{DA}:r_{MA}$  of 2, and a sinusoidal intensity profile with a grating constant slightly below 10  $\mu\text{m}$ . Again an asymmetric profile is found (height of peaks > depth of valleys). However, before this profile can be compared to the measured profile, which is also plotted in Fig. 5.8, it has to be corrected for smearing out due to the finite beam spot-size of the microprobe. A convolution of the simulated profile with the beam-spot intensity profile, which can very well be approximated by a Gaussian-shaped profile (4  $\mu\text{m}$  FWHM), is also plotted in Fig 5.8.

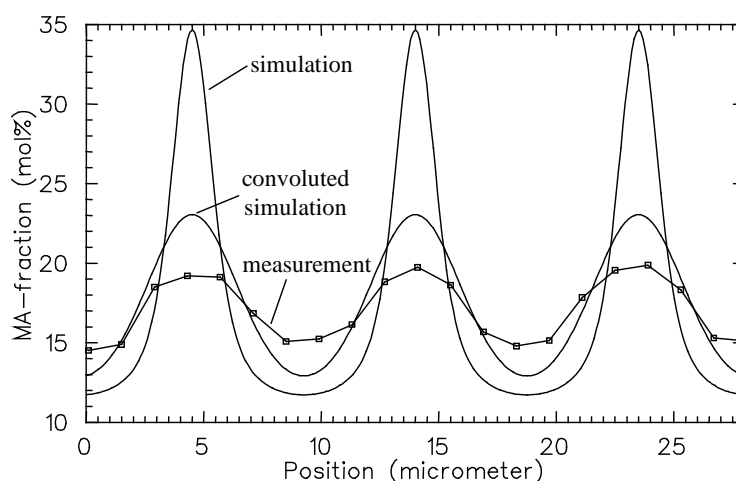


Fig. 5.8: The MA-fraction profile from measurement, simulation, and simulation convoluted with the beam-spot intensity profile. See text for details.

From Fig. 5.8 it can be seen that the convoluted simulation shows a nearly symmetric shape, comparable to the measured profile. However, there is still a discrepancy between the measured and the convoluted simulation. In the model, full conversion is assumed, together with a reactivity ratio of exactly 2, a perfectly sinusoidal intensity profile, reaction rates proportional to the light intensity, and unhindered mobility of the monomers during polymerization. A decreasing monomer mobility with polymerization, a light intensity profile with a non-zero intensity in the ‘dark’ areas, or a lower  $r_{DA}:r_{MA}$  ratio may explain the difference in amplitude and consequently in the amount of opposite diffusion. Incorporation of a monomer mobility, dependent on polymerization and phase, is not straightforward. However, by choosing a  $r_{DA}:r_{MA}$  ratio of 1.5, the agreement between the measurement and the convoluted simulation was found to improve significantly.

The quantitative  $\mu\text{PIXE}$  analysis thus provides the opportunity to study the reaction and diffusion properties of **mMA** and **mDA** mixtures.

## 5.4 $\mu$ PIXE analysis of dual-labeled lithographic gratings

### 5.4.1 Description of the dual-labeled system

The PIXE technique offers the interesting possibility to study both monomer types individually, when a dual-labeled monomer mixture is used. In that case, the diffusion of both monomer components can be measured, excluding contributions of density variations. Possible differences in mobility between the mono-functional and the bi-functional monomer may be studied. Therefore, a system of two monomer types was chosen, that each contain an element that can be detected with PIXE. The monomers should be able to form a homogeneous mixture and (ideally) have similar polymerization and diffusion properties as the **mMA** and **mDA** in the original system. The selected monomers are schematically shown in Fig. 5.9. Notice that now the difunctional acrylate monomer, which in fact is a methacrylate, is labeled with silicon (**mSiDA**), in contrast to the system considered in the previous section. The monofunctional acrylate is labeled with chlorine (**mCIMA**). The two selected monomers do not show liquid-crystalline properties, which excludes phase-dependent effects that may affect diffusion.

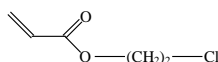


Fig. 5.9a: The chlorine-labeled monofunctional acrylate monomer (**mCIMA**, 2-chloroethyl acrylate,  $H_7C_5O_2Cl$ ,  $M=134.7$ , 0.95 g/ml)

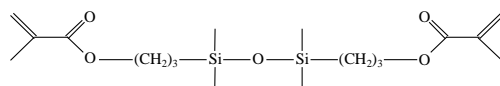


Fig. 5.9b: The silicon-labeled di-methacrylate monomer (**mSiDA**, bis(3-methacryloxypropyl)-tetramethyldisiloxane,  $H_{34}C_{18}O_5Si_2$ ,  $M=386$ , 0.83 g/ml, from Petrarch)

### 5.4.2 Sample preparation

At Eindhoven University of Technology, a mixture was prepared containing a molecular ratio of **mCIMA**:**mSiDA** = 1:1. After adding about 0.1 wt% of photo-initiator (Irgacure 651), a transparent blend with a density of 0.92 g/ml was obtained.

Photo-masks of soda-lime glass plates (Hoya SLW, 40×40 mm<sup>2</sup>, 1.5 mm thick) with a chromium-patterned layer were fabricated, each containing eight 10×10 mm<sup>2</sup> areas with a grating pattern of parallel lines. The grating constant of these areas ranges from a few micrometer up to a millimeter.

The lithographic grating film was made using a photo-mask and an additional 40×40 mm<sup>2</sup> glass slide (1 mm thick), which were cleaned with both ethanol and distilled water. A thin

layer of a 1% N-diethylmethylsilylamine solution in a 1:1 mixture of propanol and distilled water was spun both on the chromium-side of the photo-masks and on one side of the glass slide, to prevent strong adhesion of the films to the glass surface after polymerization. Subsequently, 6  $\mu\text{m}$  glass particles in ethanol were deposited on the coated glass slide. By pressing the photo-mask to the glass slide with the glass particles in between, cells were obtained which were filled with the liquid, low-viscosity monomer mixture by capillary suction. The chromium side of the photo-mask is in direct contact with the monomer mixture, to avoid diffraction effects during subsequent photo-polymerization with UV-light.

A Philips PLS-9W/10 Black Light (350-390 nm, 2.2W) was placed 15 cm above a filled sample cell. The transmission of the UV-light through the photo-mask-glass is larger than 80%. The UV-light intensity on the monomer mixture is estimated to be in the order of 0.1 mW/cm<sup>2</sup>. With a heating plate, the filled sample cell was heated to about 70 °C, before and during polymerization.

First, the sample was illuminated for 3 minutes through the photo-mask to perform patterned photo-polymerization. Next, to fix the complete film, the sample cell was turned over and uniformly polymerized for about half an hour. Finally, the glass plates were separated and several sections of the thin, newly polymerized film were successfully peeled off. Against the light, a line-structure could be seen across the film. Using a laser pointer, diffraction of the laser beam by the film was observed.

#### 5.4.3 $\mu\text{PIXE}$ analysis of the dual-labeled grating film

The free-standing polymer film was mounted in the microprobe set-up. A 3 MeV proton beam, with a beam current of 25 pA, was focussed into a beam spot with a diameter of about  $3 \times 3 \mu\text{m}^2$ . An area of the sample, that had been illuminated with the photo-mask with 50  $\mu\text{m}$  grating constant, was placed in front of the ion beam.

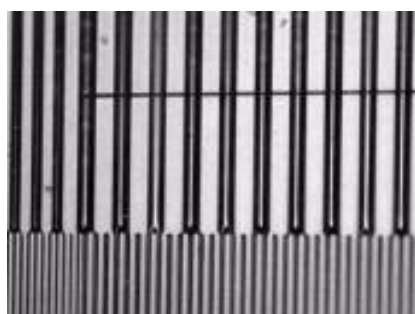


*Fig. 5.10: A (front-lit) optical microscopy image of the polymer film after the measurement. Clearly visible are the (vertical) line structures in the film and the (horizontal) line along which the ion beam was scanned. The vertical dark areas correspond to the areas that were masked by the chromium photo-mask and hence are non-illuminated.*



Similar to the experiments on the holographic gratings (section 5.3), a simultaneous PIXE, NBS, and NFS measurement was performed, while the beam spot was scanned across the sample in a line. Equally distributed over all 1024 points, a dose of 85 nC was accumulated.

Fig. 5.10 shows an optical microscopy image of the sample after this measurement. Clearly visible are the (vertical) line structures in the polymer film, with four regions of the grating, and the (horizontal) line along which the ion beam was scanned.

From the NBS and NFS data, ion beam induced degradation was observed by a decrease of the hydrogen normalized yield. For oxygen and carbon, no measurable decrease was found. Assuming a similar hydrogen loss for all positions, a fit of the hydrogen loss curve was made, using the data summed over all positions. A damage correction factor of 1.125 for hydrogen was obtained. Next, for each measured position, the bulk areal density was determined from the H+C+O normalized yield and the hydrogen damage correction factor. This is shown in Fig. 5.11, together with the independent results of the subsequent STIM measurement. For the latter, the measured energy loss was converted into an areal density using a stopping power of 120 keV/(mg/cm<sup>2</sup>). An excellent agreement between the two measurements is observed.

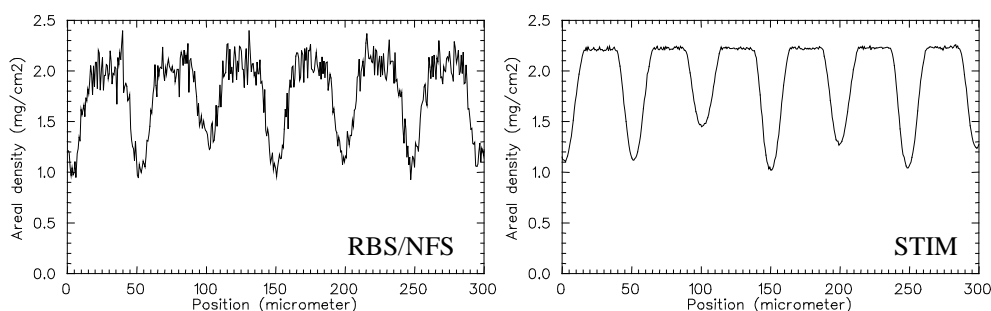


*Fig. 5.11: Areal density of the film, as measured using NBS/NFS and STIM. The independent measurements show excellent agreement, but more important, large variations in areal density.*

Surprisingly, large areal density variations exist across the film. The film thickness, which is estimated to vary between 10 and 20  $\mu$ m, exceeds the 6  $\mu$ m diameter of the glass micro-particles spacing the glass plates. This is confirmed by alpha-stepper measurements, which show a surface relief of about 10  $\mu$ m, mainly on one side of the film. It can also be seen (from the STIM measurement) that the thick areas are flat and similar in areal density. The thin areas, on the other hand, vary in areal density.

Apparently, a net mass transport to the illuminated areas has occurred, causing an increase in areal density in these areas resulting in swelling and a surface relief. Obviously, two-way diffusion, if any, is not sufficient to keep a homogeneous film. The material is pressed against the glass plates, which explains the flat tops. From the dark areas in between, material is sucked away and voids are beginning to form. It is not clear whether the swelling of the polymer occurs during illumination or after removal of the glass plates.

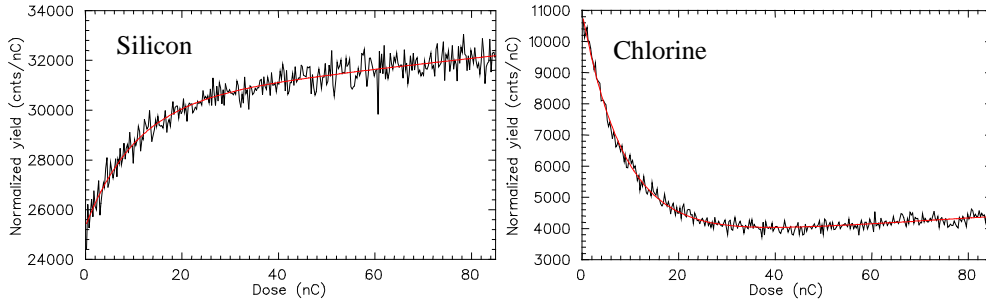


*Fig 5.12: Normalized PIXE yield for silicon and chlorine, summed over all positions. See text for details.*

It is important to note that contrary to the experiment in section 5.3, where the glass plates are mechanically fixed by an epoxy glue, in this experiment the glass plates are freely floating on the glass spacers.

From the PIXE data, the silicon and chlorine signals were extracted. Fig. 5.12 shows the normalized yield as a function of dose for silicon and chlorine, summed over all positions. For silicon, an overall exponential increase is measured, up to 30%. For chlorine, initially a large exponential decrease of over 60% is observed, together with an overall almost linear and much smaller increase. The PIXE data has to be corrected for both material loss and changes in self-absorption as a function of dose. It is, however, unlikely that the increase for silicon (and chlorine) may fully be explained by the decreasing absorption for X-rays resulting from the decrease in the hydrogen and chlorine areal density, since only a few wt% hydrogen and chlorine is present in the films. A large contribution must be attributed to sample contraction during irradiation.

The integrated normalized yield for silicon and chlorine is plotted in Fig. 5.13, as a function of position on the sample. The data in Fig. 5.13 has not been corrected for material loss or changes in X-ray absorption as a function of dose. These curves roughly follow the bulk areal density. However, distinct features are observed for the silicon and chlorine curves.

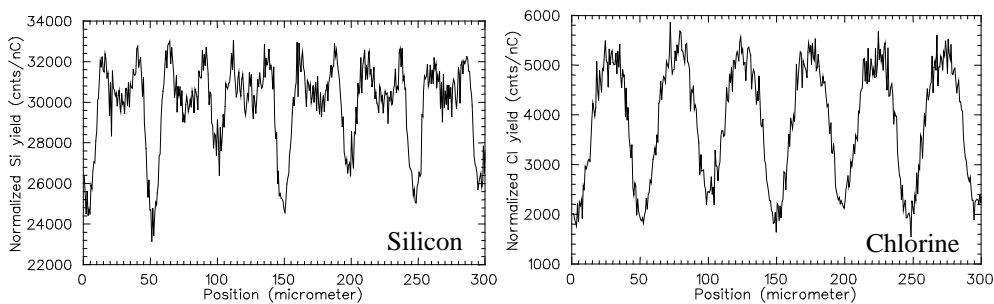


*Fig. 5.13: Normalized PIXE yield for silicon and chlorine, summed over all dose. See text for details.*

The difference between the bulk areal density distribution and the elemental yield curves may be caused by a position dependence of the MCF, which corrects for X-ray absorption, or by a position dependence of the material loss with dose. Additionally, a modulation in the silicon and chlorine concentration as a function of position is found, with a higher Cl:Si ratio in the illuminated areas than in the dark areas. It can therefore be concluded that, in addition to a dose-dependent damage correction, also position-dependent corrections of the PIXE normalized yields are required.

Since the yield for each position and dose interval shows too much statistical variation for individual correction factors, the PIXE, NBS and NFS list-mode data were divided and binned into several areal density and ion dose intervals. Using the bulk areal density as a function of position (Fig. 5.11), the data was divided into five intervals: *a*) 0.7-1.2 mg/cm<sup>2</sup>, *b*) 1.2-1.5 mg/cm<sup>2</sup>, *c*) 1.5-1.8 mg/cm<sup>2</sup>, *d*) 1.8-2.1 mg/cm<sup>2</sup>, and *e*) 2.1-2.5 mg/cm<sup>2</sup>. This data was further divided and binned into eleven dose intervals, each with an integrated dose of about 7.7 nC.

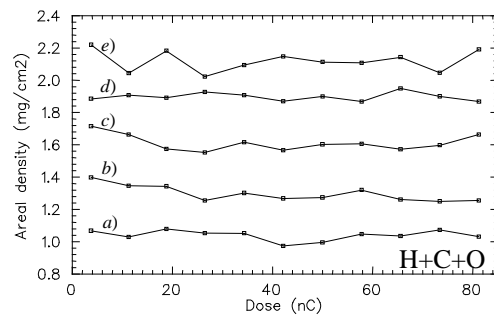


Fig. 5.14: The bulk areal density as a function of irradiation dose, for each of the five areal density intervals. See text for details.

Fig. 5.14 displays the bulk areal density for each of the five areal density intervals, as a function of dose interval. Relative errors are introduced by the ion-dose measurement and by the counting statistical accuracy (< few %). Absolute errors are introduced by the solid-angle calibration, scattering cross-section values from literature, and the ion-dose measurement. Although hydrogen loss with dose is observed and corrected for, the bulk areal density (H+C+O) decreases by less than 2% and, in essence, shows no dependence on dose.

Fig. 5.15 shows the measured normalized PIXE yield for silicon and chlorine as a function of irradiation dose, but now separately for each of the bulk areal density intervals. To correct for X-ray absorption, the MCF for silicon and chlorine X-rays must be determined from the bulk areal density. The MCF is also partially determined by the silicon and chlorine areal densities themselves. Therefore, the  $MCF_{Si}$  and the  $MCF_{Cl}$  were determined iteratively using the H+C+O+Si+Cl areal density for each of the intervals, using the absorption coefficients given in Table 5.1. The variation in MCF for each interval is directly caused by the variations of the bulk areal density. A further error may be introduced by systematic errors in the absorption coefficient  $\mu$ , obtained from the database [4].

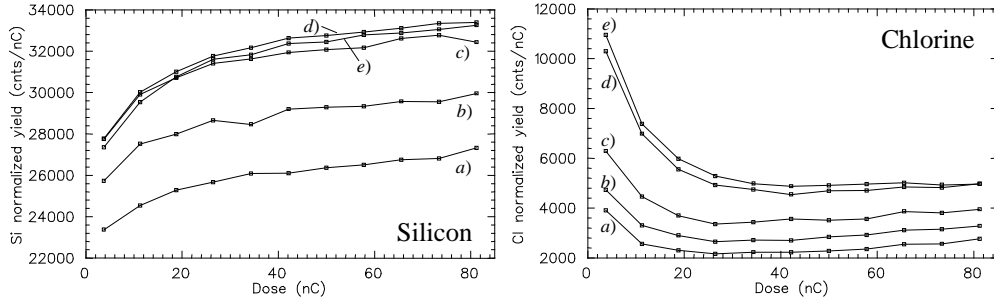


Fig. 5.15: The normalized PIXE yield for silicon and chlorine as a function of irradiation dose, for each of the five areal density intervals.

Fig. 5.16 shows the resulting MCF for silicon and chlorine. Both these MCFs are largely determined by the bulk areal density. As mentioned earlier, variations in the chlorine and silicon areal density with dose are too small to have a noticeable effect on the MCFs and they are nearly independent of irradiation dose. Apparently, the increase of about 30% in the normalized silicon yield (Fig. 5.12 and Fig. 5.15) is not compensated by a decrease of the  $MCF_{Si}$ .

In Fig. 5.17, the MCFs for silicon and chlorine are plotted as a function of bulk areal density. An almost linear relation between the MCFs and the bulk areal density is found, and the data in Fig. 5.15 can be corrected for X-ray absorption effects. The result is shown in Fig. 5.18. Now, a monotone increase of the areal densities of silicon and chlorine with the bulk areal density is obtained and both the silicon and the chlorine signal still show an overall increase with dose (after the initial decrease of chlorine with dose).

The silicon areal density increases similarly for all bulk areal density intervals, and a damage correction factor of 0.9 is calculated. For the chlorine, the damage correction factor increases almost linearly from 2.0 at  $1.0 \text{ mg/cm}^2$  to 2.5 at  $2.2 \text{ mg/cm}^2$ . The increase of silicon and chlorine, in addition to a decrease due to element loss, is probably caused by sample contraction under the influence of the ion beam irradiation.

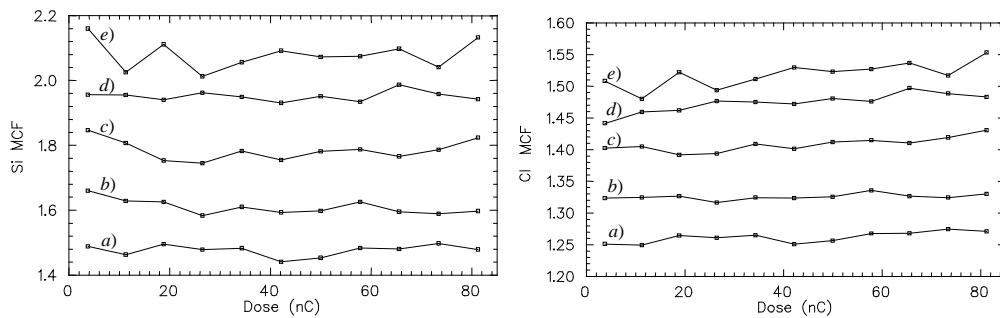


Fig. 5.16: The MCF for silicon and chlorine as a function of irradiation dose, for each of the five bulk areal density intervals. See text for details.

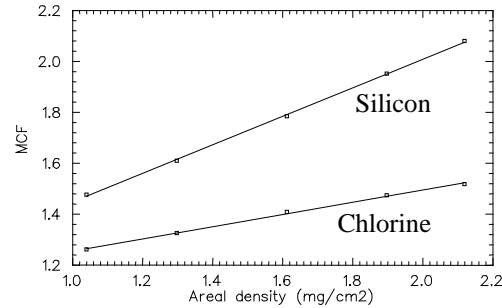


Fig. 5.17: The MCF for silicon and chlorine as a function of bulk areal density. Variations with dose were not measured. (see Fig. 5.16). A nearly linear variation is found.

Using the variation of MCF with bulk areal density (Fig. 5.17) and the damage correction factors as a function of bulk areal density (from Fig. 5.18), the PIXE normalized yield for each of the 1024 scan-positions, summed over the whole dose, can be corrected and converted into an areal density. The result is shown in Fig. 5.19a, for both silicon and chlorine. In Fig. 5.19b, the silicon and chlorine concentration (weight fraction) is plotted as a function of position. It appears that, in contrast to Fig. 5.13, now the areal densities of silicon and chlorine also show nearly flat-topped peaks and steep valleys, similar to the bulk areal density (Fig. 5.11). However, looking at the silicon and chlorine concentration profile (Fig. 5.19b), it is seen that a modulation in the silicon and chlorine concentrations is measured, and thus also a modulation in the chemical composition of the film. Apparently, this chemical composition modulation is superimposed on the observed bulk areal density modulation!

Additionally, a measurement was performed on an area of the film that was homogeneously illuminated during polymerization. Similar loss curves for H and Cl were measured, and a similar increase in the yield of Si, over a dose of 24 nC. As expected, a homogeneous bulk areal density distribution was found. Furthermore, no structure in the silicon and chlorine areal densities was observed.

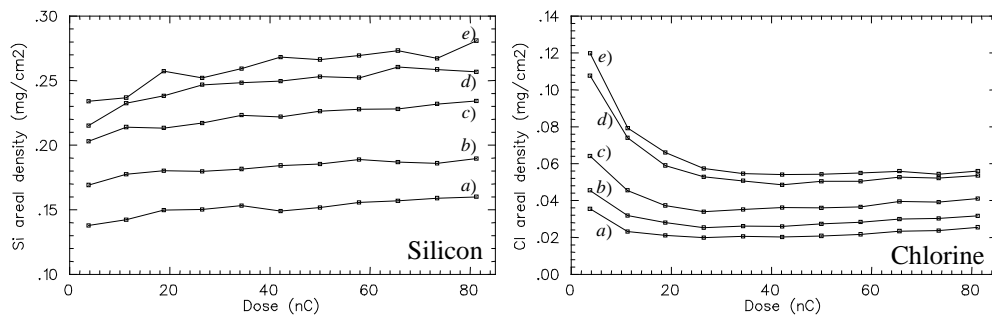


Fig. 5.18: The silicon and chlorine areal density as a function of dose, for each of the five bulk areal density intervals. Corrections for X-ray absorption have been applied. From these curves, the damage correction factors can be determined.

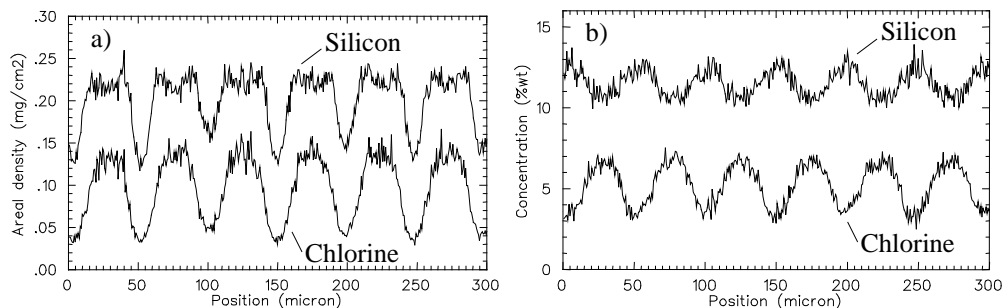


Fig. 5.19: The measured and corrected areal density distribution (a) and concentration profile (b) of silicon and chlorine across the film.

Summing over all positions, and correcting for hydrogen loss, a bulk areal density of  $1.5 \text{ mg}/\text{cm}^2$  was found. After correcting for X-ray absorption and dose-dependencies, a zero-dose silicon areal density of  $0.16 \text{ mg}/\text{cm}^2$  was found and a chlorine areal density of  $0.10 \text{ mg}/\text{cm}^2$ . These values agree with the values calculated from the initial monomer ratio. They are also comparable to the average values measured in the grating film, which confirms that only mass transport and no mass loss occurs during patterned photo-polymerization.

#### 5.4.4 Interpretation of the results

Two effects have been measured. First, a modulation in the bulk areal density was measured. A net mass transport to the illuminated areas has occurred. Second, a modulation in the chemical composition was measured. Surprisingly, the illuminated, thick areas contain a high concentration of chlorine, that is attached to the mono-functional acrylate monomer. Also, the dark, thin areas contain a high concentration of silicon, that is attached to the bi-functional methacrylate monomer.

From the observed modulation in the bulk areal density, it might be concluded that the two monomer types have comparable reactivities, since both monomers diffuse to the illuminated areas. A somewhat higher mobility of the mono-functional acrylate monomers compared to the bi-functional methacrylate monomers may then explain the observed modulation in the chemical composition. However, the observed modulation in chemical composition might also be caused by a (slightly) higher reactivity of the mono-functional acrylate monomers compared to that of the bi-functional methacrylate monomers. This may be caused by the screening-effect of the extra methyl side-group in the methacrylate. Apparently, the two reactive groups on the bi-functional monomer do not outweigh the difference in reactivity of the acrylate and methacrylate functional groups.

In order to investigate the surprising areal density variations in the sample, additional films were prepared, from the same monomer mixture, but in this case the two glass plates were firmly clamped together. This was done to prevent separation of the glass plates due to swelling and relaxation of the polymer in the illuminated areas during patterned illumination and fixation. In this way, films were obtained with a homogeneous bulk areal density. From

STIM measurements, it was found that the variations in bulk areal density were less than 0.5%. Furthermore, no modulation in the areal density of silicon and chlorine could be detected. Hence, during fixation of the cells almost no mass transport takes place, and no two-way diffusion is observed. This is in agreement with the previous hypothesis that the reactivity of both monomer types is comparable.

## 5.5 Conclusions and recommendations

In this chapter, it is demonstrated that the  $\mu$ PIXE technique provides the means to quantitatively study lateral diffusion processes of monomers during patterned photo-polymerization. By labeling the monomers with a PIXE-detectable element, such as silicon or chlorine, the final monomer distribution in the films can be determined.

First, measurements on the silicon-labeled van Nostrum system [1] have been performed. A modulation in the monomer fraction of labeled mono-acrylate (MA-fraction) was found across the homogeneous film. The observed increase in MA-fraction in the dark, non-illuminated areas confirms that the supposed two-way diffusion of the mono- and di-acrylate monomers has occurred.

Simulation of the modulation in the MA-fraction, using the van Nostrum model [1], convoluted with the ion beam intensity profile, displays a similar sinusoidal profile as the measured modulation in the MA-fraction. The measured contrast in the MA-fraction between dark and illuminated areas is lower than the simulated contrast. Several factors, not included in the model may account for this difference, such as decreasing monomer mobility with polymerization, and reaction rate dependence on light intensity and polymerization.

Second, films have been produced, using a dual-labeled monomer blend. Labeling of both monomers, each with a different element, enables the direct determination of the monomer ratios and hence chemical composition, independent of the bulk areal density.

Modulations in both the bulk areal density and the chemical composition were measured across these films. From the increased thickness in the illuminated areas, it is concluded that a net mass transport to the illuminated areas has occurred. Future measurements on samples prepared using illumination along a mask edge (step illumination) may reveal the distance over which mass transport can take place.

The measured modulation in the chemical composition shows that, in contrast to the first system where the di-acrylate preferably moved to the illuminated areas, now the mono-acrylate displays a higher concentration in the illuminated areas. The chemical composition modulation is most likely explained by a higher mobility of the monoacrylate monomers compared to the diacrylate monomers. Experiments with fixed glass plates showed no chemical composition modulation, which presumably implies that both monomers have a

comparable reactivity. Differential Scanning Calorimetry (DSC) measurements could be used to verify this.

For future studies of two-way diffusion, it is recommended to select a mixture of a mono-functional and a bi-functional monomer, having identical functional end-groups and thereby a different reactivity. Furthermore, to reduce complications due to beam-induced element loss in  $\mu$ PIXE analyses, labeling with elements less volatile than chlorine is preferable. Labeling, however, should not affect film transparency.

In addition to studies of lateral modulations in chemical composition and areal density, using a scanning ion microprobe, it may also be interesting to study chemical composition as a function of depth [3]. In this case, depth profiling with ion scattering techniques may be feasible, in view of their depth resolution.

## References

- [1] C.F. van Nostrum, R.J.M. Nolte, D.J. Broer, T. Fuhrman, J.H. Wendorff, *Chem. Mater.* 10 (1998) 135-145.
- [2] D.J. Broer, *Chemisch Magazine*, April 1998, 144-147.
- [3] D.J. Broer, J. Lub, G.N. Mol, *Nature* 378 (1995) 467-469.
- [4] F. Munnik, *Accuracy Evaluation of Absolute Calibration in Thick-Target PIXE*, (Ph.D. Dissertation, Eindhoven University of Technology, 1994).
- [5] G. Odian, *Principles of Polymerization*, McGraw-Hill, New York (1970).
- [6] V.V. Krongauz and A.D. Trifunac, *Processes in Photoreactive Polymers*, (Chapman & Hall, New York, 1995), Chapters II-5 and III-1.
- [7] W.J. Tomlinson, E.A. Chandross, H.P. Weber and G.D. Aumiller, *Appl. Optics* 15 (1976) 534-541.



## Chapter 6

# Verification of a uranium micromass standard using an ion microprobe

*Analysis of dust samples from uranium enrichment facilities is focused on the detection and analysis of uranium containing particles. Notably the  $^{235}\text{U}$ -abundance is of interest, since  $^{235}\text{U}$  is used both as nuclear fuel in power reactors and as an explosive in nuclear weapons. The chemical and isotopic analysis of such individual particles is thought to be an effective analytical tool to check the absence of nuclear-weapons production-activities. This is justified by the assumption that the compositions of collected individual particles match the range of compositions of present nuclear source materials.*

*Techniques applied by laboratories to perform single particle (isotopic) analysis include both neutron induced fission track analysis, in combination with thermal ionization mass spectrometry (TIMS) [1], and secondary ion mass spectrometry (SIMS) [2,3]. The reported analytical performances of different techniques and individual laboratories will have to be verified with respect to the uncertainties in the final outcome and limits of detection. This requires a uranium micromass standard: a set of micrometer-sized particles with a well defined, monodisperse mass distribution and a certified uranium isotopic composition.*

*Previously, a set-up to produce monodisperse sets of uranium-oxide microparticles from certified uranium solutions has been developed [4]. An accurate determination of the uranium mass distribution of such a set is required, before it can be validated as a micromass standard. Only a few analytical techniques are, however, suitable to accurately determine the uranium mass of individual microparticles.*

*In this work, the Eindhoven scanning ion microprobe is successfully applied to determine the relative uranium mass distribution of a set of  $\text{U}_3\text{O}_8$  microparticles. Simultaneous use is made of the PIXE, RBS, and NFS techniques. Individual microparticles, 4  $\mu\text{m}$  in size and embedded in a Formvar foil, are located by a short, fine-grid scan. Next, a stationary beam is used to measure the uranium yield of individual particles. A relatively large beam-spot is used to ensure uniform particle irradiation.*

*A population of 23 particles was measured, for which a relative uranium mass distribution with a standard deviation of 16% was found. A discussion of the measurement accuracy and of the uranium micromass standard verification is given.*

This work was done in collaboration with André Lagerwaard, affiliated to the Interfaculty Reactor Institute at Delft University of Technology.

## 6.1 Introduction

Chemical and isotopic analysis of single, small particles is of interest in a wide field of applications. One of these is the detection and analysis of uranium containing particles from dust samples taken in uranium enrichment facilities. Enriched uranium, with an increased  $^{235}\text{U}$  abundance, can be used both as nuclear fuel in power reactors and, if highly enriched, as an explosive in nuclear weapons. The determination of the  $^{235}\text{U}$  abundance in the particles is used to reveal undeclared enrichment activities besides the nuclear fuel production, and thus to check the absence of nuclear-weapons production activities. This method is justified by the assumption [9] that the measured composition of the individual particles from dust samples is equivalent to the range of compositions of nuclear source materials that is present in the facility where the dust samples were taken.

Techniques applied by laboratories around the world for single particle (isotopic) analysis include both neutron induced fission track analysis, in combination with thermal ionization mass spectrometry [1], and secondary ion mass spectrometry [2,3]. The reported analytical performances of different techniques and individual laboratories, however, have to be verified with respect to the uncertainties in the final outcome and limits of detection. For calibration purposes, a uranium micromass standard is required: a monodisperse set of micrometer-sized particles with a well-defined mass distribution and a certified uranium isotopic composition. A set is defined to be monodisperse [8] in its mass if its mass distribution is log-normal with a geometrical standard deviation (GSD) smaller than 1.25. The GSD corresponds to the inverse-log of the standard deviation of the log-transformed distribution.

Lagerwaard [4] has developed a set-up to produce monodisperse sets of uranium-containing micrometer-sized particles from certified uranium solutions using spray pyrolysis. From the uranium solution, a spray of droplets with a well-controlled size is created. A carrier gas then drives these droplets through several ovens, where the solvent evaporates. Finally, the formed solid particles are collected in a filter unit. An accurate determination of the uranium mass distribution of such a set of particles is required, before it can be validated as a micromass standard.

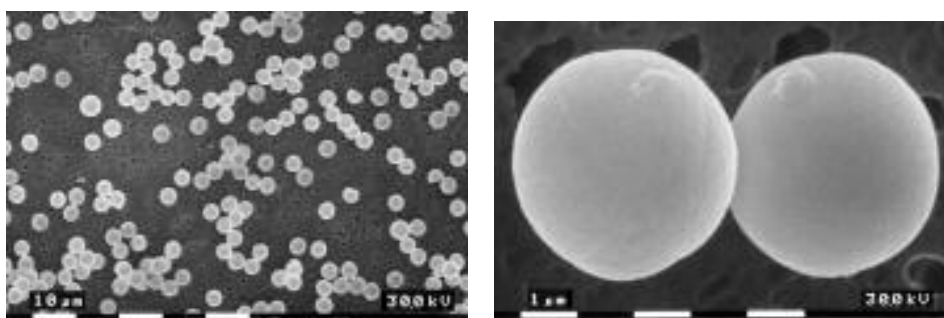


*Fig. 6.1: Scanning electron microscope (SEM) images of the 4  $\mu\text{m}$  sized  $\text{U}_3\text{O}_8$  microspheres, collected on a polycarbonate membrane filter.*

From X-ray diffraction measurements [4], the chemical structure of the particles appeared to be uranium-oxide ( $\text{U}_3\text{O}_8$ ). Using scanning electron microscopy, the morphology of the particles was found to be spherical, as can be seen in Fig. 6.1. The diameter of the particles is about 4  $\mu\text{m}$ .

Only very few analytical techniques, however, are suitable to directly and accurately determine the uranium mass of individual micrometer-sized particles. Isotope dilution mass spectrometry [10], combined with either thermal ionization mass spectrometry [1] or inductively coupled plasma mass spectrometry, is used to give the certified, absolute uranium mass content of single micrometer-sized particles. However, the measurement of a single particle may take as long as one week. Indirect methods may be less time-consuming but are not very accurate. Measurement of the particle diameter and density [6], for example, introduces uncertainties in the resulting particle mass of about 30%.

In this work, a scanning ion microprobe is successfully applied to determine the relative uranium mass distribution of a set of  $\text{U}_3\text{O}_8$  microparticles. Simultaneous use is made of the particle induced X-ray emission (PIXE) technique, and (non-)Rutherford backscattering and forward scattering spectrometry (RBS/NFS). Individual microparticles, embedded in a Formvar foil, are located by a short, fine-grid scan. Next, a stationary beam is used to measure the uranium yield of the individual particles. In contrast to other microprobe single-particle analyses [5], where a very small beam spot is used, in this work a relatively large beam-spot is used, to ensure uniform particle irradiation in order to measure the total uranium content.

Experimental details on sample preparation and ion-beam analysis techniques are given in section 6.2. Results for the relative uranium mass distribution are presented in section 6.3, together with a discussion of the measurement accuracy. Conclusions and recommendations can be found in section 6.4.

## 6.2 Experimental

### 6.2.1 Sample preparation

In the preparation procedure, the uranium-oxide particles are collected on a polycarbonate filter. Initial measurements showed that a Formvar or carbon coating was required to fix the particles onto the filter and to prevent their movement under the influence of ion beam irradiation. As can be seen from the electron microscopy image in Fig. 6.1, only a few individually situated particles can be found for single-particle analysis, due to the high particle density on the filter.

Therefore, the particles were separated from the polycarbonate filter by ultrasonic vibration and subsequent centrifugation in ethanol. After removal of the filter and superfluous ethanol, the precipitate of uranium-oxide particles was added to a 2 wt% solution of Formvar in chloroform. A 10  $\mu\text{l}$  droplet of this suspension was pipetted onto the surface of distilled water, forming a thin film with a diameter of a few cm and a thickness in the order of 100 nm.

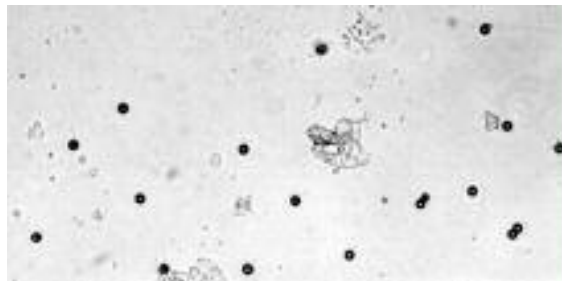


*Fig. 6.2: Optical microscope image of the uranium-oxide microparticles embedded in the Formvar foil (magnification: ~300 times).*

The film was lifted from the surface using a perforated overhead sheet as support frame. In this way, a free-standing Formvar film was obtained, in which the uranium-oxide particles are embedded. Fig. 6.2 shows an optical microscopy image of this sample. It can be seen that most particles lie about 20  $\mu\text{m}$  or more apart, making single-particle analysis possible.

### 6.2.2 Ion microprobe measurements

The prepared sample is mounted in the scanning ion microprobe set-up. A 3 MeV proton beam is focussed into a beam spot with a relatively large size compared to the diameter of the uranium-oxide particles. This is done to ensure homogeneous and complete irradiation of the particles and thus determination of their total uranium content. Note that in this way it is not possible to determine the absolute uranium mass of each measured particle. Only the uranium mass content relative to other particles can be determined, which, however, is sufficient for determining the relative uranium mass distribution.

The beam spot-size was measured both at the beginning and at the end of the measurement series, and was found to be  $(14.4 \pm 0.5) \times (11.4 \pm 0.5) \mu\text{m}^2$ . The initial beam current of about 1 nA slowly decreased during the day down to 300 pA. For PIXE analysis, a Si(Li) X-ray detector at a backward angle of 135 degrees was used, with an additional beryllium absorber ( $8.9 \text{ mg/cm}^2$ ,  $\sim 50 \mu\text{m}$ ) to prevent back-scattered protons from entering the detector. For RBS and NFS analysis, charged-particle detectors were used at 147 degrees and 45 degrees, respectively.

First, the position of the individual particles within the sample has to be determined. Hence, a fine-grid scan of  $256 \times 256$  points,  $1.4 \mu\text{m}$  apart, is made. Fig. 6.3 shows the distribution of the yield in the uranium M-line peaks in the PIXE histogram (PIXE U-M, see below), measured in less than 30 mins. A similar distribution can be obtained from the uranium yield in the NFS histogram (NFS U), from the uranium L-line yield in the PIXE histogram (PIXE U-L), and from the uranium yield in the RBS histogram (RBS U), with decreasing statistics. From these distributions, using the mouse pointer within the COLUMBUS data-acquisition software, the location of individual, free-lying particles can be selected with an accuracy of better than 2  $\mu\text{m}$  in both directions.

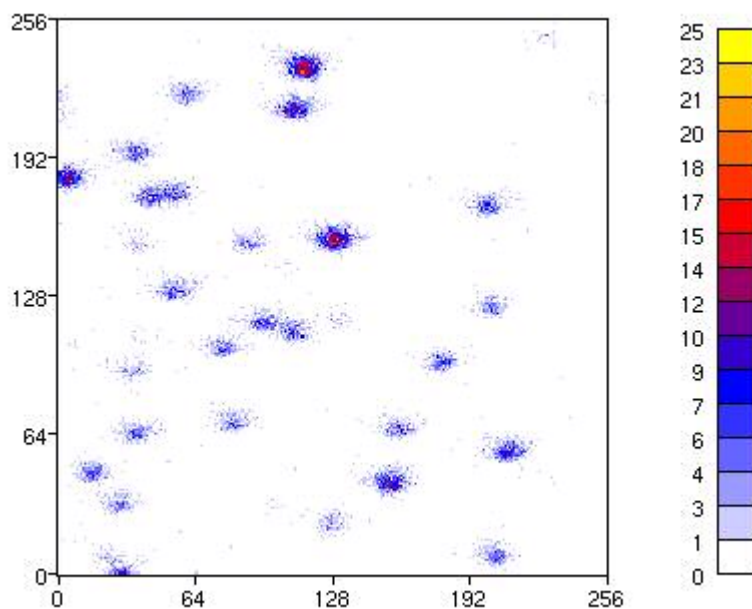


Fig. 6.3: Distribution of the PIXE Uranium M-line yield vs. position. The scanned area measures about  $360\ \mu\text{m} \times 360\ \mu\text{m}$ . See text for details.

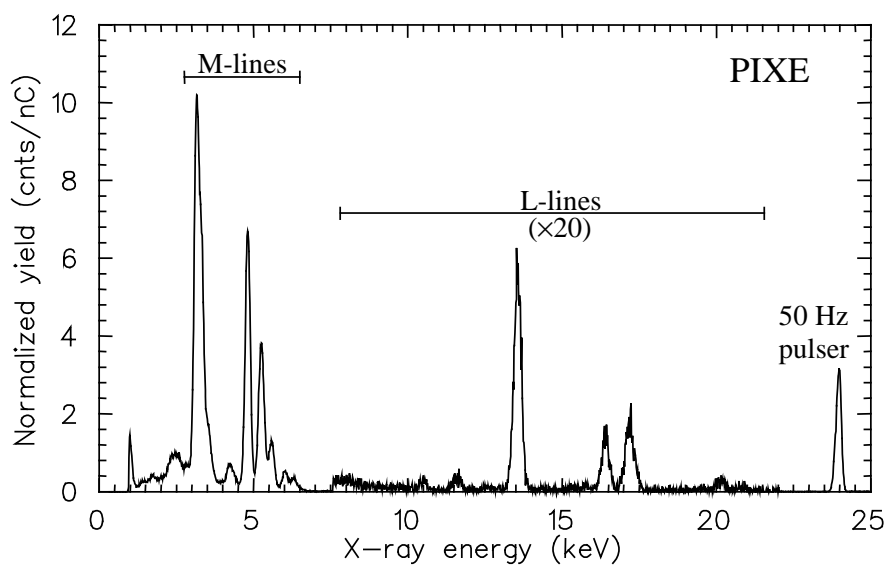
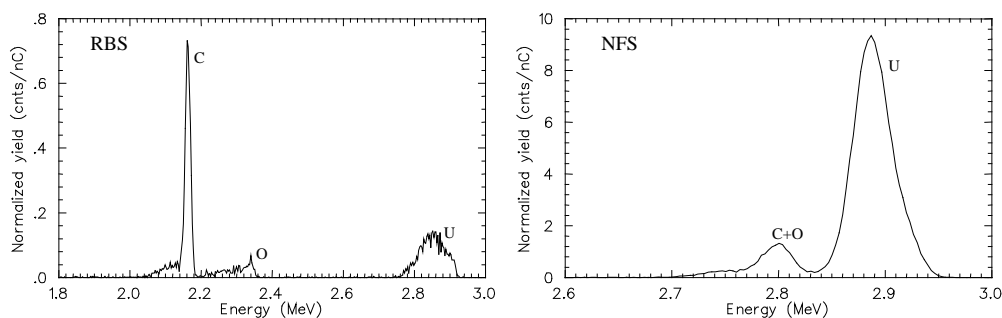


Fig 6.4: PIXE histogram of a measurement on a single uranium-oxide particle. The uranium M-lines give a higher yield than their L-lines. The yield of the latter is multiplied by a factor of 20 for clarity. A 50 Hz pulser peak is also visible.

The analysis of individual particles is done using a stationary beam. The measurement of one particle takes about 10 minutes, during which an ion dose of 300-600 nC is applied. The latter is measured using a Keithley programmable electrometer connected to the Faraday cup.

In Fig. 6.4, the PIXE histogram of such a measurement is plotted. Both the uranium L-X-ray lines and the M-X-ray lines can be seen, the first being background free and the latter having a yield that is about 15 times higher. In Fig. 6.5, the NFS and RBS histograms are plotted, showing full mass separation for the RBS uranium peak and sufficient mass separation for the NFS uranium peak in relation to the oxygen and carbon contributions.

Typical yields in the uranium peaks, at the given ion dose, are  $10^5$  counts for PIXE U-M,  $5 \cdot 10^4$  counts for NFS U,  $3 \cdot 10^3$  counts for PIXE U-L, and  $1.6 \cdot 10^3$  counts for U-RBS. The PIXE yields are determined from peak/background fitting using the PIXE analysis package AXIL [7]. The NFS and RBS yields are determined from elementary yield integration over a channel interval.



*Fig 6.5: RBS and NFS histogram of a measurement on a single uranium-oxide particle. The oxygen signal arises from both the oxide in the particle and the Formvar foil in which the particles are embedded. The large carbon signal (observed in RBS) is due to an increased thickness of the Formvar foil around the uranium-oxide particle.*

Unfortunately, in the course of the day, deformation of the sample and/or drift in the ion beam causes a misalignment of several micrometers between the beam-spot and the particle under analysis. Hence, it is not sufficient to make just one fine-grid area scan to locate the uranium-oxide particles, at the beginning of the measurement series. Therefore, after each measurement of two to three single particles, a new area scan of about 10 minutes is made to check and correct for misalignment between the beam-spot and the particles.

Fig. 6.6 shows optical microscopy images of the sample after the measurement of a series of uranium-oxide particles. Since the black halo resulting from carbonization of the Formvar foil by the ion beam is centered on each of the irradiated particles, it is concluded that the procedure described above has been applied successfully.

Furthermore, from these optical microscopy images, it is found that most of the irradiated spots correspond to measurements of single particles. For about 10 percent of the spots, a cluster of two particles was measured, which was included in the normalization.

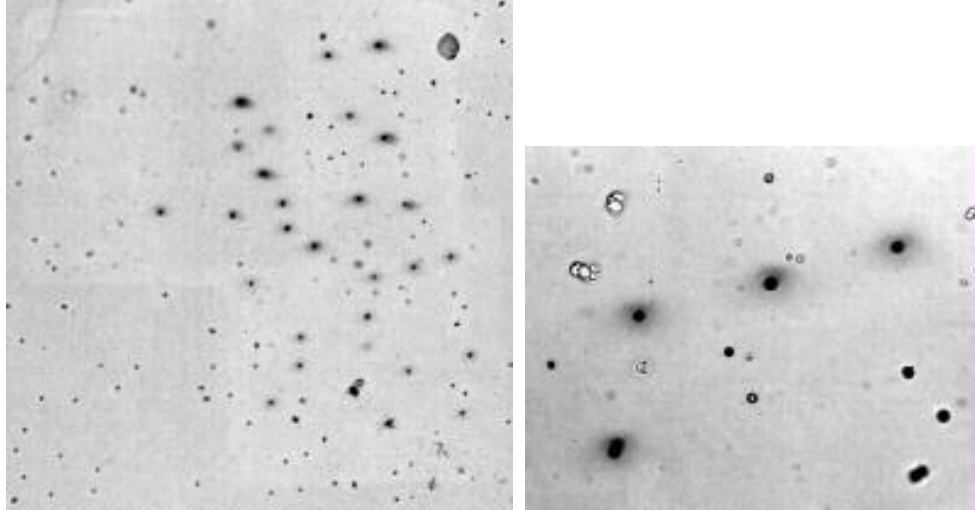


*Fig. 6.6: Optical microscopy images of the uranium-oxide particles embedded in Formvar foil, after the microprobe measurement (magnification: left  $\sim 90\times$ , and right  $\sim 300\times$ ). The (clusters of) individual particles can clearly be seen. In addition, a black halo can be seen around the particles that have been irradiated with the microprobe, resulting from carbonization of the Formvar.*

### 6.3 Results and discussion

For a population of 23 uranium-oxide particles, the normalized uranium yield was determined from the PIXE U-M, PIXE U-L, RBS U, and NFS U data. The results are visualized in Fig. 6.7, sorted according to normalized uranium yield. In each of the data sets, a standard deviation of the normalized uranium yield distribution of  $\pm 16\%$  is found. No correlation of the normalized uranium yield with measurement number was found, as expected. Due to the high inaccuracy in the determination of the particle diameters from optical microscopy, unfortunately relation between the normalized uranium yield and the particle diameter could be found.

Before drawing conclusions about the standard deviation of the relative uranium mass distribution, the measurement accuracy and conditions are discussed. First, the standard deviation of the measured uranium yield, which scales inversely with the square root of the number of events, is  $\sim 2\%$  for PIXE U-L and RBS U, and  $< 0.2\%$  for PIXE U-M and NFS U. Another error is introduced via the ion-dose measurement. Since the stopping of 3 MeV protons in  $\text{U}_3\text{O}_8$  is as low as  $18 \text{ keV}/\mu\text{m}$ , the total energy loss of these protons upon transmission through the uranium-oxide particles is less than 100 keV. All protons are thus transmitted, except for a negligible scattered fraction that is not measured in the Faraday cup. The relative error in the ion-dose measurement is estimated to be below 2%.

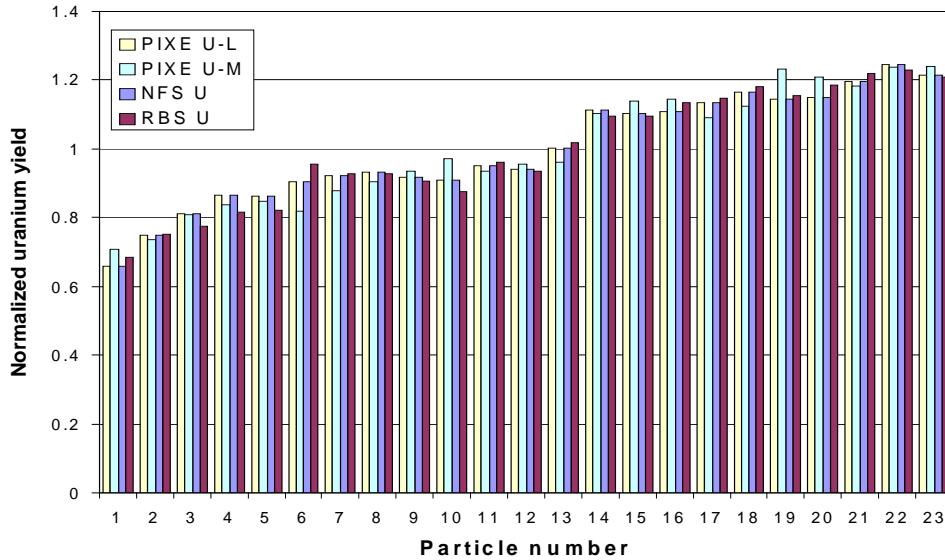


Fig. 6.7: The normalized uranium yield for all 23 uranium-oxide particles, determined from the PIXE U-L, PIXE U-M, RBS U, and NFS U data. A standard deviation of 16% in the normalized uranium yield is found.

Additional errors can be introduced by instabilities in the size, shape, and position of the beam-spot. As already indicated, from the fine-grid area scan, the location of the particles can be determined with an accuracy of better than  $2\ \mu\text{m}$ , since the scan points are  $1.4\ \mu\text{m}$  apart. As an additional check, a long ( $>1\ \text{h}$ ) measurement was performed, in which the beam was scanned in a  $2\times 2$  scan pattern, again with the scan points  $1.4\ \mu\text{m}$  apart, centered around a single uranium-oxide particle. The spread in the PIXE U-M, PIXE U-L, and NFS-U normalized uranium yield for all four scan points was found to be less than 2%.

Over this measurement period of one hour, a decrease in the normalized uranium count-rate of a few percent was observed. This is either due to a drift in the ion beam or due to sample deformation resulting from ion beam irradiation, which causes a misalignment between the center of the particle and the beam-spot. For the single-particle measurements, which take less than 10 minutes, this effect is negligible. Furthermore, after each two to three measurements, a new area scan was made to check and correct for any misalignment.

A relatively large beam spot-size was used in order to have a homogeneous irradiation of the particles, which is necessary for the normalized uranium yield to be proportional to the uranium mass. The measured beam-spot intensity profile can be approximated by a Gaussian-shaped intensity profile, with a size of  $(14.4\pm 0.5)\times(11.4\pm 0.5)\ \mu\text{m}^2$  FWHM. It was calculated that, in this case, about 28% of the beam intensity hits the  $4\ \mu\text{m}$  uranium-oxide particle and that the intensity across this particle is constant within about 2%.



In PIXE, the absorption of uranium L- and M-X-rays plays a role. It was calculated that for a spherical  $\text{U}_3\text{O}_8$  particle with a diameter of  $4\text{ }\mu\text{m}$  (density of  $4\text{ g/cm}^3$ ), about 3% of the  $\text{U-L}_\alpha$  X-rays is absorbed (Matrix Correction Factor (MCF) equals 1.03) and about 19% of the  $\text{U-M}_{\alpha+\beta+\gamma}$  X-rays is absorbed within the particle (MCF equals 1.24). However, for a variation of 30% in the particle volume (uranium mass), which corresponds to a variation of 10% in the particle diameter, a variation of only 0.3% in the  $\text{U-L}_\alpha$  MCF and of 2% in the  $\text{U-M}_{\alpha+\beta+\gamma}$  MCF results. This appears much less dramatic than expected.

In Fig. 6.8, the measured normalized NFS U yield is plotted against the normalized PIXE U-M yield. A linear relation between the two is found, from which it is concluded that the variation in X-ray absorption, within the range of the measurements, is negligible.

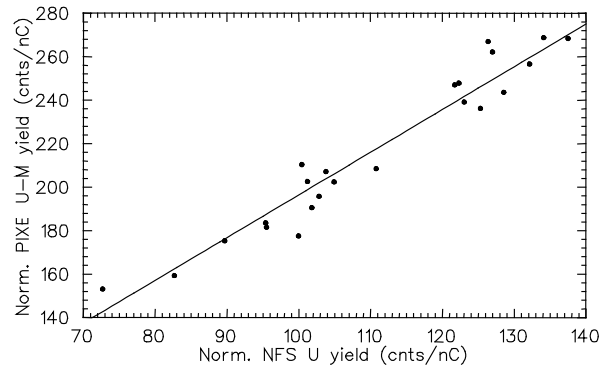


Fig 6.8: The linear relation between the normalized NFS U yield and the normalized PIXE U-M yield, showing the negligible variation in X-ray absorption.

From the above discussion it follows that the accuracy in the determination of the normalized uranium yield of a single particle is better than 5%. Since the detector solid angles and the X-ray production and scattering cross-sections are constant for all measured particles, the normalized uranium yield distribution is equal to the relative uranium mass distribution of the set. This holds for the NFS U, RBS U, PIXE U-M, and PIXE U-L, since the MCF for X-ray absorption was also found to be constant. Hence, a standard deviation of the relative uranium mass distribution of  $\pm 16\%$  is found. This corresponds to a geometrical standard deviation (GSD) of the uranium mass just below 1.2. It can therefore be concluded that the measured set of particles is monodisperse in uranium mass content, since by definition for monodispersity a GSD equal to or smaller than 1.25 is required [8].

## 6.4 Conclusions and recommendations

The Eindhoven scanning ion microprobe set-up has been successfully used to measure the relative uranium mass distribution of a population of 23 micrometer-sized  $\text{U}_3\text{O}_8$  particles. A standard deviation of the uranium mass of 16% was found. This corresponds to a geometrical

standard deviation of the uranium mass of just below 1.2, from which it is concluded that the measured set of particles is monodisperse.

Full characterization of the relative uranium mass distribution requires the measurement of a larger population of individual particles. The number of particles measured in this work was limited by the availability of the ion beam for one day only. Therefore, with the present stability of the ion beam and the sample itself, the time to perform an area scan (up to 30 min) to locate the particles, and the time to measure a single particle (~10 min.) has to be reduced.

For this, an increase of the ion beam current and/or the detector solid angles is required. Furthermore, the number of area scans between the single-particle measurements has to be reduced. Hence, the number of free-lying particles within one area scan has to be increased (less clusters and a more homogeneous distribution). More importantly, both the instability (drift) of the ion beam and the deformation of the sample due to ion beam irradiation have to be reduced further. To prevent deformation of the sample, (nylon) grids, as commonly used in electron microscopy, as a backing for the Formvar foil could be helpful.

In that case, after only one area scan to locate the individual particles, a large population of single particles can be measured. The software for automated measurement of multiple single-particles, located by a fine-grid area scan, has already been implemented.

## References

- [1] J.N.C. van Geel and A. Lagerwaard, European patent nr. 97121136.2-2204 (02.12.1997): A method for determining quantitatively the content of fissile material in small size particles.
- [2] D.S. Simons, SIMS VIII: Proceedings of the 8th International Conference on SIMS, (Wiley, Chichester, England, 1992), pp. 715-718.
- [3] J.J. Stoffels, J.K. Briant, D.S. Simons, J. Am. Soc. Mass Spectrom. 5 (1994) 852-8.
- [4] A. Lagerwaard, K.J. Volkers, D. Camelot, P.J. Kooyman and J. van Geel, Proceedings of the workshop on the status of measurement techniques for the identification of nuclear signatures, Geel, Belgium, 25-27 February 1997, ESARDA, Report EUR 17312, pp. 115-119.
- [5] A.J. Antolak, D.H. Morse, D.W. Heikkinen, M.L. Roberts, G.S. Bench, Nucl. Instr. and Meth. B130 (1997) 211-218.
- [6] André Lagerwaard, private communication.
- [7] B. Vekemans, K. Janssens, L. Vincze, F. Adams, P. Van Espen, X-ray Spectrom. 23 (1994) 278-285.
- [8] N.A. Fuchs and A.G. Sutsagin, Aerosol Science, (Academic Press, New York, 1966), Chapter 1: Generation and Use of Monodisperse Aerosols.
- [9] D. Donohue, S. Deron and E. Kuhn, IAEA Bulletin, 36 (3), (1994).
- [10] P. de Bievre, Trace Metal Analysis in Biological Samples, (Biomedical Publishers, Foster City CA, 1987).

# Summary

The research described in this dissertation concerns the scanning ion microprobe at the Cyclotron laboratory of Eindhoven University of Technology. A significant part of this work is devoted to the research and development of new data-acquisition and detection techniques for use with this microprobe set-up. Additionally, a number of analytical applications was presented, in which the scanning ion microprobe and its detection techniques are essential.

First, a new system for set-up control, multi-parameter data-acquisition, monitoring, and data analysis was developed. At present, this system is routinely used in all ion-beam analysis experiments at the Cyclotron laboratory, including the microprobe experiments described in this work.

Second, two novel detector types for use in the microprobe set-up were studied. For X-ray spectroscopy, the feasibility of a detector based on a charge-coupled device (CCD) was investigated. Normally, CCDs are used for optical imaging. In this work, a literature survey was presented, from which it was concluded that certain CCD detectors can offer an improved X-ray energy resolution and detector efficiency over a conventional Si(Li) detector. It was also concluded, however, that in that case the readout speed of such a CCD is too slow to distinguish the X-rays from each individual sample position, at the high microprobe beam-scanning rates.

For charged-particle spectroscopy, the feasibility was investigated of a one-dimensional position-sensitive detector (PSD), based on the resistive charge-dividing mechanism. Normally, these detectors are used in optical laser-tracking applications. In this work, both noise calculations and characterization measurements of the PSD and homemade pre-amplifiers were presented. It was concluded that the position resolution and linearity of this PSD system are sufficient to use it as an angle-disperse charged-particle detector in ion-scattering experiments. It was also concluded, however, that its energy resolution is not (yet) optimal for use in spectroscopic applications.

Third, radiation damage effects were studied in charged-particle detectors that are commonly used in the microprobe experiments. Through direct, localized irradiation of such a detector with ions, using the microprobe, the change in the pulse-height-to-energy calibration with ion dose and beam current was determined. Such a change, which is likely to occur in for example scanning transmission ion microscopy (STIM) experiments, can now be predicted and corrected.

In addition to these technological studies, a number of analytical problems from various fields of research were studied using the microprobe set-up and its techniques. Predominantly, use was made of the particle induced X-ray emission (PIXE) technique.

Two analytical problems from the field of organic optoelectronic devices were tackled. First, for precursor-route pentacene-based field-effect transistors, the pentacene conversion-efficiency as a function of conversion temperature was measured. This was done via the PIXE yield of chlorine, which is only present in the residual precursor. A relation to device

performance was found. Second, for precursor-route poly-(phenylene-vinylene) (PPV) based light-emitting diode structures, the effect was studied of hydrochloric acid on the degradation of the indium electrode contact. Hydrochloric acid is released or sometimes even added during the precursor conversion. The formation of  $\text{InCl}_3$  clusters, about 50  $\mu\text{m}$  in size, across the organic PPV layer was demonstrated.

Furthermore, measurements on optical gratings were performed, consisting of polymer films with a specific composition modulation. These films are created via patterned photo-polymerization of acrylate-monomer mixtures. In this study, it was shown that, using the ion microprobe, monomer distributions can be measured in the polymerized films. Insight into the process of opposite monomer diffusion during photo-polymerization was obtained.

Finally, in this work it was shown that with the ion microprobe, the relative mass distribution of a set of micrometer-sized uranium-oxide particles can be determined. Such a set may only serve as a micromass calibration standard for analytical tools for uranium detection, if the monodispersity in its uranium mass is verified. The measurement of 23 particles, presented in this dissertation, strongly suggests that this is the case for the set under study.

# Samenvatting

Het onderzoek, beschreven in dit proefschrift, is toegespitst op de scannende ionen-microbundel van het Cyclotron laboratorium aan de Technische Universiteit Eindhoven. Een belangrijk deel van dit werk betreft het onderzoek en de ontwikkeling van nieuwe data-acquisitie en detectietechnieken voor gebruik in deze microbundel-opstelling. Daarnaast wordt een aantal analytische toepassingen gepresenteerd, waarin de scannende ionen-microbundel en de bijbehorende detectietechnieken essentieel zijn.

Ten eerste is een nieuw systeem voor het besturen van de opstelling, voor acquisitie van multi-parameter data, en voor het weergeven en analyseren van deze data ontwikkeld. Momenteel wordt dit systeem dagelijks gebruikt bij alle ionenbundelanalyse-experimenten in het Cyclotron laboratorium, inclusief de experimenten met de microbundel die beschreven zijn in dit proefschrift.

Ten tweede zijn twee nieuwe types van detectoren bestudeerd, voor toepassing binnen de microbundel-opstelling. Voor spectroscopie van Röntgenstraling, is de toepasbaarheid van een detector gebaseerd op een *charge-coupled device* (CCD) onderzocht. Normaliter worden CCDs gebruikt voor optische beeldvorming. In dit werk wordt een literatuurstudie gepresenteerd, op basis waarvan wordt geconcludeerd dat bepaalde CCD detectoren een verbeterde Röntgen-energiesolutie en detector-efficiëntie kunnen leveren, in vergelijking met een conventionele Si(Li) detector. Er wordt echter ook gevonden dat de vereiste uitleessnelheid van zo'n CCD dan te laag is om de geproduceerde Röntgenstraling van iedere positie op het preparaat afzonderlijk te kunnen registreren, bij de hoge scansnelheid van de microbundel.

Voor spectroscopie van geladen deeltjes is de toepasbaarheid van een één-dimensionele plaatsgevoelige detector (PSD) bestudeerd, gebaseerd op het mechanisme van resistieve ladingsdeling. Normaliter wordt dit type detector gebruikt voor optische positiebepaling met lasers. In dit werk worden zowel ruisberekeningen als karakterisatiemetingen van de PSD en zelfgebouwde voorversterkers gepresenteerd. Op basis hiervan wordt geconcludeerd dat de positieresolutie en de lineariteit van dit PSD systeem voldoende zijn om het te gebruiken als een hoekgevoelige detector voor geladen deeltjes in verstrooiingsexperimenten. De energiesolutie blijkt echter (nog) niet optimaal te zijn voor spectroscopische toepassingen.

Ten derde zijn effecten van straling bestudeerd in geladen-deeltjesdetectoren, die veel gebruikt worden bij microbundel-experimenten. Door, met behulp van de microbundel, zo'n detector direct, lokaal te bestralen met ionen is de verandering van de pulshoogte-naar-energie calibratie als functie van ionendosis en bundelstroom bepaald. Zo'n verandering, die kan optreden tijdens bijvoorbeeld *scanning transmission ion microscopy* (STIM) experimenten, kan nu worden voorspeld en gecorrigeerd.

Naast deze technologische studies, zijn een aantal analytische problemen uit diverse onderzoeksgebieden met behulp van de microbundel-opstelling en bijbehorende technieken

bestudeerd. Met name is gebruik gemaakt van de *particle-induced X-ray emission* (PIXE) techniek.

Uit het vakgebied van de organische *opto-electronic devices* zijn twee analytische problemen aangepakt. Ten eerste is voor *precursor-route* pentacene veldeffect-transistoren, de pentacene conversie-efficiëntie als functie van de conversietemperatuur gemeten. Dit is gedaan via het PIXE signaal van chloor, dat alleen aanwezig is in de achtergebleven resten *precursor*. Een relatie met de *device performance* is gevonden. Ten tweede is voor *precursor-route* poly-(phenylene-vinylene) (PPV) licht-emitterende diestructuren het effect van chloorzuur op de degradatie van het indium electrodecontact onderzocht. Chloorzuur komt vrij, of wordt soms zelfs toegevoegd, tijdens de *precursor* conversie. De vorming van  $\text{InCl}_3$  clusters, zo'n 50  $\mu\text{m}$  in grootte, verdeeld over de organische PPV laag is aangetoond.

Daarnaast zijn metingen verricht aan optische roosters, bestaande uit polymeerfilms met een specifieke modulatie in de samenstelling. Deze films worden gemaakt via patroonsgewijze fotopolymerisatie van acrylaatmonomeer-mengsels. In dit onderzoek wordt aangetoond dat, met de ionenmicrobundel, monomeerverdelingen kunnen worden gemeten in de gepolymeriseerde films. Een inzicht in het proces van tegengestelde monomeerdifusie tijdens de fotopolymerisatie is verkregen.

Tenslotte wordt in dit werk getoond dat het met de ionenmicrobundel mogelijk is om de relatieve massaverdeling van een set uranium-oxide deeltjes, met een afmeting van een paar micrometer, te bepalen. Zo'n set kan dienen als micromassa calibratiestandaard ten behoeve van analytische technieken voor uranium detectie, maar alleen als de monodispersiteit van de uranium massa is gecontroleerd. De meting van 23 deeltjes, zoals in dit proefschrift getoond, duidt er sterk op dat dit voor de betreffende set het geval is.

# Publications

**Exploration of X-ray and charged-particle spectroscopy with CCDs and PSDs**, D.P.L. Simons, P.H.A. Mutsaers, L.J. van IJendoorn, M.J.A. de Voigt, Nucl. Instr. and Meth. B139 (1998) 273-278.

**Study of localised radiation damage to PIPS detectors by a scanning ion microprobe: Measured effects and the consequences for STIM analysis**, D.P.L. Simons, A.J.H. Maas, P.H.A. Mutsaers, M.J.A. de Voigt, Nucl. Instr. and Meth. B130 (1997) 160-165.

**A multi-parameter system for acquisition, monitoring, and analysis of scanning ion microprobe data**, P.H.A. Mutsaers and D.P.L. Simons, Nucl. Instr. and Meth. B130 (1997) 127-132.

**Recoil selection by pulse shape discrimination in elastic recoil detection analysis with  $\alpha$ -particles ( $\alpha$ -ERDA)**, A.J.H. Maas, S.S. Klein, D.P.L. Simons, M.J.A. de Voigt, Nucl. Instr. and Meth. B108 (1996) 268-273.

**Verification of a uranium micromass standard using the Eindhoven scanning ion microprobe**, D.P.L. Simons, A. Lagerwaard, P.H.A. Mutsaers and M.J.A. de Voigt, submitted for publication in Nucl. Instr. and Meth. B.

**Indium diffusion in model polymer light-emitting diodes**, M.P. de Jong, D.P.L. Simons, M.A. Reijme, L.J. van IJendoorn, A.W. Denier van der Gon, M.J.A. de Voigt, H.H. Brongersma, R.W. Gymer, submitted for publication in Synth. Metals.

**IBA on functional polymers**, M.P. de Jong, D.P.L. Simons, L.J. van IJendoorn, M.J.A. de Voigt, M. A. Reijme, A.W. Denier van der Gon, H.H. Brongersma, submitted for publication in proceedings 15th International Conference on the Application of Accelerators in Research and Industry, November 4-7th, 1998, Denton TX, USA.

**The Eindhoven multi-parameter data-acquisition system for ion beam experiments**, D.P.L. Simons, P.H.A. Mutsaers, F.C. van Nijmweegen, to be published.

# Dankwoord

Graag wil ik hier alle mensen bedanken die aan dit proefschrift hebben bijgedragen.

Mijn eerste dank gaat uit naar prof. Martien de Voigt, mijn 1<sup>e</sup> promotor. Martien, bedankt voor de mogelijkheid om mijn promotie-onderzoek, voor een groot deel naar eigen inzicht, en geheel met jouw steun, uit te voeren in jouw groep. De werkomgeving van het Cyclotron laboratorium, met z'n collegialiteit, vriendschap, gezelligheid en werklust is er een om trots op te zijn.

Prof. Klaas Kopinga van de groep Fysische Informatica wil ik bedanken voor zijn bereidheid om mijn 2<sup>e</sup> promotor te zijn. Klaas, bedankt voor je hulp in de afgelopen maanden. Samen met jou wil ik de bedrijfsgroep Laboratorium Automatisering bedanken. Zonder hun expertise was een deel van dit promotiewerk niet mogelijk.

Mijn grootste dank gaat uit naar Peter Mutsaers, mijn copromotor. Peter, vanaf mijn stage tot nu was je een fantastische begeleider en collega. Met veel plezier zal ik blijven terugdenken aan onze samenwerking en natuurlijk onze rondreis door de States.

Ook Leo van IJzendoorn heeft mij veel geholpen. Leo, bedankt voor je enthousiasme, sturing en kritische blik gedurende de hele promotietijd.

Van mijn vele collega-AIO's, wil ik er enkele persoonlijk bedanken. Jos Maas en Paul van Dijk introduceerden mij, als kersverse promovendus, in het flamboyante AIO-leven. Daarna werkten Jos en ik samen aan een reeks succesvolle experimenten. Thanks guys!

Een goede samenwerking en veel plezier, tijdens en na werktijd, had ik ook met mijn kamergenoten John Quaedackers, Niels Noordhoek en Peter Brands. Niels, John en Peter, bedankt voor de fantastische tijd.

Een vijftal studenten dank ik voor hun bijdrage aan dit proefschrift. Fulco Verheul, voor zijn onderzoek aan de plaatsgevoelige detector, Leon van der Meer, voor zijn bijdrage aan het nieuwe data-acquisitie systeem, Mark Lubberink, voor de detectorschade-metingen, Annemiek Kamp, voor de pentacene-FET experimenten, en Kevin Nolan voor het implementeren van de STIM filtermethodes.

Onmisbaar, en altijd bereid tot hulp, was de Cyclotron bedrijfsgroep: Rinus Queens, Frits van Hirtum, Jan van den Berg, Eric van den Eerden, Wim Kemper en Janus Castelijns. Bedankt voor jullie inzet.

Dankzij Wim Verseijden beschikte ik altijd over een uitstekend computer-systeem, waarmee ik ook uitgebreid mocht experimenteren. Wim, bedankt dat ik je assistent-systeembeheerder kon zijn.



Ad Kemper dank ik voor zijn expertise en hulp bij het ontwerpen van de PSD voorversterkers. Siebren Klein dank ik voor zijn vele, vaak verrassende ideeën en bruikbare tips. Leo de Folter dank ik voor al zijn technische assistentie. Coby Damsma dank ik voor haar secretariële hulp.

Een belangrijk deel van mijn onderzoek was alleen mogelijk dankzij de hulp van externe onderzoekspartners. De samenwerking met vooral Adam Brown en Peter van de Weijer van Philips Research, en met mijn collega Michel de Jong, resulteerde in hoofdstuk 4. Het onderzoek met prof. Dirk Broer en René van Nostrum resulteerde in hoofdstuk 5. Met André Lagerwaard werkte ik samen aan hoofdstuk 6. Bedankt allemaal.

Prof. C. van Eijk van de TU Delft dank ik voor zijn bijdrage als leescommissie-lid van dit proefschrift. Shell en NWO ben ik dankbaar voor de verstrekte reisdonaties voor mijn conferentiebezoeken.

Mijn vrienden, familie en kennissen ben ik erg dankbaar voor alle geboden gezelligheid en onmisbare afleiding van mijn werk. Daarbij bedank ik speciaal Erica voor haar liefdevolle ondersteuning. Mijn broer Paul dank ik, met trots, voor zijn ontwerp en uitvoering van de omslag.

Tenslotte ben ik blij dat ik mijn ouders kan bedanken voor alle mogelijkheden die ze mij altijd hebben geboden. Mama en papa, bedankt voor alles!

# Curriculum Vitae

## David Simons



6 maart 1971	Geboren te Roermond
1983 - 1989	Gymnasium B aan het College Sittard te Sittard
1989 - 1994	Studie Technische Natuurkunde aan de Technische Universiteit Eindhoven
1994 - 1998	Promotieonderzoek aan de Technische Universiteit Eindhoven in de groep Fysica en Toepassingen van Ionenbundels van de faculteit Technische Natuurkunde
sept. 1998 -	Werkzaam bij Philips Research te Eindhoven in de sector Informatie en Software Technologie

Stellingen

behorende bij het proefschrift

**Data Acquisition, Detector Technology,  
and Materials Analysis with a  
Scanning Ion Microprobe**

door

David Peter Louis Simons

Eindhoven, 14 december 1998

-I-

Een multi-parameter data-acquisitie systeem is onmisbaar voor het uitvoeren van de huidige, complexe experimenten van het ionenbundel-analyse onderzoek.

(Dit proefschrift, hoofdstuk 1)

-II-

De toepassing van een *charge-coupled device* (CCD) als Röntgen-spectrometer in een scannende ionen microbundel is (nog) niet zinvol, vanwege de daarvoor gestelde eisen met betrekking tot de uitleessnelheid en stralingsgevoeligheid.

(Dit proefschrift, hoofdstuk 2)

-III-

Het verdient aanbeveling om monomeerdiffusie-processen tijdens niet-uniforme fotopolymerisatie verder te bestuderen met behulp van ionenbundel-analyse technieken.

(Dit proefschrift, hoofdstuk 6)

-IV-

De door Breese gebruikte semi-logaritmische schaalverdeling voor het weergeven van de relatie tussen de gemeten pulshoogte en de ionendosis in een *ion-beam-induced charge* (IBIC) experiment suggereert ten onrechte een drempel-effect.

(M.B.H. Breese, J. Appl. Phys. 74 (1993) 3789-3799, en dit proefschrift, hoofdstuk 3)

-V-

De ionen microbundel van de TUE kan nu al een super nanobundel worden genoemd.

-VI-

Het feit dat natuurkundestudenten bedreven zijn in het werken met computers is helaas nog geen garantie voor hun programmeerqualiteiten.

-VII-

Het gebruik van positron emissie tomografie voor het *in-situ* bestuderen van chemische reacties biedt unieke mogelijkheden voor het optimaliseren van proces-condities in industriële reactoren.

-VIII-

Het 'jaar-2000' probleem is aan het eind van dit millennium niet meer actueel.

-IX-

Op de maan kunnen geen wereldrecords worden gevestigd.

-X-

De benaming 'Eindhoven lichtstad' kan terecht worden gewijzigd in 'Eindhoven verkeerslichtstad'.

-XI-

Het openbaar vervoer is een zaak van hollen en stilstaan.

-XII-

"LEDs make things better. "